

Supervisory Control of Drilling of Composite Materials

by

Motoyoshi Ozaki

B.A. (The University of Tokyo, Japan) 1985

M.E. (The University of Tokyo, Japan) 1987

A dissertation submitted in partial satisfaction of the

requirements for the degree of

Doctor of Philosophy

in

Engineering-Mechanical Engineering

in the

GRADUATE DIVISION

of the

UNIVERSITY OF CALIFORNIA, BERKELEY

Committee in charge:

Professor Masayoshi Tomizuka, Chair

Professor C. K. Hari Dharan

Professor J. Karl Hedrick

Professor Seth R. Sanders

Spring 2000

## Abstract

### Supervisory Control of Drilling of Composite Materials

by

Motoyoshi Ozaki

Doctor of Philosophy in Engineering-Mechanical Engineering

University of California, Berkeley

Professor Masayoshi Tomizuka, Chair

Composite materials have attractive features, such as high ratios of strength-to-weight and stiffness-to-weight. However, they are easily damaged when they are machined. A typical damage is delamination, which can occur when fiber reinforced composite laminates are drilled. The objective of this research is to study the drilling processes of carbon fiber reinforced laminates, and to develop and test a supervisory control strategy for their delamination-free drilling.

Characterization of thrust force and torque is achieved through constant feedrate drilling experiments. The average values of thrust force and torque during the full engagement of the drill are utilized to obtain the Shaw's equations' parameters. The thrust force profile just before exit is given special attention.

The Hocheng-Dharan equations, which give conservative values of delamination at the entrance and at the exit, are modified to express the influence of one lamina thickness

explicitly. They are utilized not only for the characterization of thrust force but also for the determination of the thrust force reference for force control.

In the design of the controllers of thrust force and torque, both thrust force and torque are assumed to be proportional to FPHR (Feed Per Half Revolution). A discrete-time dynamic model is established for the case when the time interval for a half revolution of the drill is divided by the sampling time, and the model is extended to the case of general spindle speeds. PI controllers are designed for the dynamic models of thrust force and torque. Root-locus techniques are used in the analysis.

The phases of the drilling process are introduced and the control strategy at each phase is explained. The supervisory controller chooses not only the best control strategy for each phase, but also the reference value and the controller gain that are suitable at each drill position.

Drilling experiments are conducted to show the usefulness of the concepts introduced in this dissertation, and to give an example of installing the control parameters, which were derived from data obtained in this research, on the supervisory controller. Efficient Delamination-free drilling is given special emphasis in the experiments.

---

Prof. Masayoshi Tomizuka  
Dissertation Committee Chair

# Table of Contents

<b>Table of Contents</b>	<b>vi</b>
<b>List of Figures and Tables</b>	<b>ix</b>
<b>1. Introduction</b>	<b>1</b>
1.1 Background	1
1.1.1 Control of Machining	1
1.1.2 Drilling of Composite Materials	3
1.2 Research Objectives and Topics	4
1.3 Organization and Outline	6
<b>2. Drilling of Composite Materials</b>	<b>8</b>
2.1 Drilling	8
2.2 Shaw's Equations	13
2.3 Drilling of Fiber Reinforced Composite Laminates and Delamination Model	14
2.3.1 Composite Laminates and Delamination	14
2.3.2 Delamination Model and Hocheng-Dharan Equation for Push-out at Exit	15
2.3.3 Delamination Model and Hocheng-Dharan Equation for Peel-up at Entrance	18
2.4 Summary	22
<b>3. Experimental Setup</b>	<b>23</b>
3.1 Matsuura MC510VSS Machining Center	23
3.2 PC-Based Machine Tool Controller	24

3.3 Setup Around the Drilling Process	25
3.3.1 Drills	25
3.3.2 Angle Attachment	26
3.3.3 Fixtures	27
3.4 Sensors	27
3.5 Air Cleaning and Dust Collecting	28
3.6 Summary	29

#### **4. Characterization of Thrust Force and Torque During Drilling of Carbon Fiber Reinforced Laminates**

4.1 Characterization of Thrust Force and Torque Curves	34
4.2 Thrust Force and Torque at Constant Feedrate Drilling and Shaw's Equations	39
4.3 Discrete Hocheng-Dharan Equations and Thrust Force at PreExit Drilling	49
4.3.1 Discrete Hocheng-Dharan Equations	49
4.3.2 Thrust Force at PreExit Drilling	51
4.4 Summary	57

#### **5. Supervisory Control for Drilling Composite Materials**

<b>¾ Controller Design ¾</b>	<b>58</b>
5.1 Transfer Functions of the Machine Tool Feed Drives	59
5.2 Position Control	61
5.3 Thrust Force Control	62
5.3.1 Modeling of Thrust Force During Drilling	63
5.3.2 Spindle Speed, Sampling Frequency and Low-pass Filter Cut-off Frequency	77
5.3.3 Design of Thrust Force Controller	80
5.4 Torque Control	94
5.4.1 Modeling of Torque During Drilling	94
5.4.2 Design of Torque Controller	96

5.5 Supervisory Control	99
5.5.1 Phases of Supervisory Control	99
5.5.2 Control Strategy for Each Phase	105
5.6 Summary	120
 <b>6. Supervisory Control for Drilling Composite Materials</b>	
$\frac{3}{4}$ <b>Experiment</b> $\frac{3}{4}$	<b>121</b>
6.1 Carbon Fiber Reinforced Laminates	121
6.2 Design Parameters of Supervisory Controller	123
6.3 Experimental Results of Supervisory Controlled Drilling of Composite Materials	127
6.4 Summary	133
 <b>7. Conclusions and Future Research</b>	<b>134</b>
7.1 Conclusions	134
7.2 Future Research	136
 <b>Bibliography</b>	<b>139</b>

## List of Figures and Tables

Fig. 2.1	Conical Point Twist Drill with Two Flutes	11
Fig. 2.2	Simplified Two-Dimensional Representation of Two-Flute Twist Drill	12
Fig. 2.3	Simplified Drill and Drilling Phases	12
Fig. 2.4	Drill Bit and Delamination (Hocheng and Dharan, 1988)	20
Fig. 2.5	Circular Plate Model for Delamination Analysis (Hocheng and Dharan, 1988)	21
Fig. 3.1	Matsuura Vertical Machining Center MC510VSS	30
Fig. 3.2	Machining Center MC510VSS and Controllers	30
Fig. 3.3	Drive Train Elements for a Single Axis of the Machine Tool X-Y	
	Table (Tung, 1993)	31
Fig. 3.4	Schematic Figure of the Experimental Setup	32
Fig. 3.5	Experimental Setup	33
Fig. 4.1	Measured Thrust Force and Torque During the Drilling of Carbon Fiber Reinforced Laminate, and the Simplified Graph Shapes	38
Table 4.1	Measured and Calculated Thrust Force and Torque	44
Fig. 4.2	Thrust Force and Torque Given by Experimental Data and Shaw's Equations	45
Fig. 4.3	$K_{Fphr \rightarrow Force}$ and $K_{Fphr \rightarrow Torque}$ Calculated from Experimental Data and Shaw's Equations	46
Fig. 4.4	Thrust Force at Chisel Edge and Cutting Edges Given by Experimental Data	47

Fig. 4.5	$K_{F_{phr} \rightarrow ForceChisel}$ and $K_{F_{phr} \rightarrow ForceCutting}$ Calculated from Experimental Data	48
Fig. 4.6	Hocheng-Dharan Equations and Discrete Hocheng-Dharan Equations for Push-out Delamination and Peel-up Delamination	53
Fig. 4.7	Uncut Thickness and Thrust Force in the <i>PreExit Drilling</i> Phase When Thrust Force Starts Decreasing	54-55
Fig. 4.8	Uncut Thickness and Thrust Force in the <i>PreExit Drilling</i> Phase When Thrust Force Starts Decreasing	56
Fig. 5.1	Block Diagram of the Sampled System from the Discrete Voltage Input to the Measured Digital Thrust Force	72
Fig. 5.2	Bode Plots of Discrete Models of $N_{HR} = 3$ with (a) $e = 0$ , (b) $e = +0.5$ , (c) $e = +1.0$ , (d) $e = -0.5$ and (e) $e = -1.0$ , and Approximate Continuous Thrust Force Models	73-75
Fig. 5.3	Simulation Result of the Unit Step Responses of the Discrete Thrust Force Models of $G_{ForceTF}^o(z)$	76
Fig. 5.4	Block Diagram of the Thrust Force Control System	85
Fig. 5.5	Root Locus of $K \cdot G_{ForcePI}^o(z) \cdot G_{ForceTF}^o(z)$	85-86
Fig. 5.6	Root Locus of $K \cdot G_{ForcePI}^o(z) \cdot G_{ForceTF}^o(z)$	87-89
Fig. 5.7	Simulation Result of the Closed Loop Unit Step Response of $K \cdot G_{ForcePI}^o(z) \cdot G_{ForceTF}^o(z)$	90-93
Fig. 5.8	Block Diagram of the Sampled System from the Discrete Voltage Input to the Measured Digital Torque	98
Fig. 5.9	Block Diagram of the Torque Control System	98
Fig. 5.10	Drill Position and Phase	103



Fig. 5.11	Overall Architecture of the Supervisory Controller	104
Fig. 5.12	Thrust Force Reference Determined by the Hocheng-Dharan Equation in the <i>Entrance Drilling</i> Phase	116
Fig. 5.13	Thrust Force Reference Determined by the Hocheng-Dharan Equation in the <i>PreExit Drilling</i> Phase	117
Fig. 5.14	Conceptual Graph of Decreasing Thrust Force Lines and Thrust Force Reference in the <i>PreExit Drilling</i> Phase	118
Fig. 5.15	Example of Thrust Force Reference Determined by Experimental Data of Thrust Force Decrease in the <i>PreExit Drilling</i> Phase	119
Fig. 6.1	Experimental Data of Supervisory Control of Drilling of Composite Materials	131-132

# **CHAPTER 1**

## **Introduction**

### **1.1 Background**

Composite materials provide distinctive advantages in the manufacture of advanced products because they have attractive features, such as high ratios of strength-to-weight and stiffness-to-weight. They can, however, be easily damaged when machined unless the machining process is performed properly. The typical damage undergone by laminated composites is delamination caused by machining processes.

Drilling is one of the most common and yet one of the most complex operations among many kinds of machining methods, for almost all materials used in industry. Drilling has been a topic in general research in manufacturing due to its popularity, the necessity of solving related problems like delamination and burr-formation, and also due to its interdisciplinary nature. The last factor is the main cause of difficulties in drilling research. Research in drilling incorporates the rigor of control theory and materials science as well as the common sense of manufacturing.

#### **1.1.1 Control of Machining**

Conventional machine tools are servo-controlled. They consist of a set of velocity or position loop controllers for the motion axes of a machine tool. The most primitive and yet popular servo control algorithm is based on PID (Proportional-plus-Integral-plus-

Derivative) control. There have been a number of proposals for advanced control applications at the servo level (Koren and Masory, 1981; Tomizuka and Lee, 1996).

Repetitive control is one of the simplest ways to introduce learning capability to servo controllers. It has been successfully applied to turning for non-circular machining (Tsao and Tomizuka, 1994).

Real-time identification and adaptive control have been applied to various machining processes, including milling (Tomizuka, Oh and Dornfeld, 1983; Lauderbaugh and Ulsoy, 1989) and turning (Tomizuka and Zhang, 1985). In adaptive control, controller parameters are adjusted in real time so that the controller and the process are well matched even if the process characteristics change. The process characteristics may change due to tool wear, machining conditions, or as a result of changes in workpiece height (or radius) and material properties.

In contrast to turning or milling processes, there has been little work done in the area of modeling and control of the drilling process. The major obstacle is that the dynamics of the drilling process are not fully understood and, therefore, cannot be accurately modeled. Furness *et al.* recorded transient responses of the thrust force and torque to command changes in spindle speed and feed, and estimated the parameters of first order models, which can be utilized for closed loop control of thrust force or torque (Furness, Wu and Ulsoy, 1992).

Furness's investigation on through-hole drilling is also an excellent example of supervisory drilling control (Furness, 1996). His supervisory controller selects an appropriate strategy and a proper reference signal based on drill position (depth-of-hole), and provides superior hole quality and low burr formation. Another approach by Kakino,

Matsubara *et al.* is an intelligent machining system with a database system that determines adequate cutting conditions and control parameters (Kakino, Matsubara *et al.*, 1998). They utilized the system for drilling with high productivity.

Many researchers have historically studied burr formation. There have been, however, only a few researchers who have studied both burr formation models and drilling control. Lee developed a model that relates thrust force and drill position to burr formation, and designed a thrust force controller that allows for force-controlled burrless drilling (Lee, 1989).

### **1.1.2 Drilling of Composite Materials**

Early papers have discussed the peculiarities of machining of composite materials, but only in the context of conventional machining processes. For example, Friend *et al.* described conventional machining processes as well as diamond and ultrasonic machining of composite materials (Friend *et al.*, 1972). Doran and Maikish obtained machinability data on boron epoxy composites (Doran and Maikish, 1972).

Although these papers provided insight into the response of composite materials to machining conditions, there has been little work in the area of developing models to predict such responses. For example, the effect of delamination during drilling has not been widely investigated. A few investigators have studied delamination experimentally, where delamination was linked to the change in the thrust force during exit of the drill (Wong *et al.*, 1982; Koenig *et al.*, 1985).

The first quantitative model of delamination based on linear elastic fracture mechanics was suggested by Hocheng and Dharan (Hocheng and Dharan, 1988). They

proposed that delamination of a laminate is related to drilling parameters and composite material properties. Jain and Yang constructed another analytical model to predict the critical thrust force and critical feedrate at which the delamination crack begins to propagate (Jain and Yang, 1992).

Stone *et al.* proposed a neural network forward model for the drilling process, and used a neural network inverse controller utilizing the equations of Hocheng and Dharan to set the thrust force reference (Stone and Krishnamurthy, 1996).

## **1.2 Research Objectives and Contributions**

The objective of this dissertation is to study the drilling processes of carbon fiber reinforced laminates, and to develop a supervisory controller for drilling. The controller is designed through analysis, simulation, and experiments, with the goal of avoiding delamination. The major contributions of this work include: characterization of thrust force and torque, modification and utilization of the Hocheng-Dharan equations, dynamic modeling of thrust force and torque, controller design for thrust force and torque, design of a supervisory controller, and drilling experiments.

- **Characterization of Thrust Force and Torque:** Thrust force and torque during drilling of carbon fiber reinforced laminates are characterized through constant feedrate drilling experiments. This characterization has two objectives. One is constructing the table, graphs and Shaw's equations of thrust force and torque during the full engagement of the drill. This information can be utilized for deciding the sensor range and the controller gains as well as determining the strategy of the supervisory

controller. The other is analyzing the thrust force at the entrance, and just before the exit. The latter stage of drilling is called *PreExit Drilling* in this dissertation. The thrust-force vs. position curves at both phases provide information for determining the control strategies, especially the thrust force reference.

- **Modification and Utilization of Hocheng-Dharan Equations:** The Hocheng-Dharan equations, which give conservative thrust force values of delamination at the entrance and at the exit (which are called ‘in the *Entrance Drilling* phase’ and ‘in the *PreExit Drilling* phase’ in our research), are modified to express the influence of the thickness of one layer explicitly. The original continuous equations are suitable for determining the thrust force reference, except when the value for the first or last layer is considered. When the Hocheng-Dharan equations are compared with the experimental data, the modified equations are more useful because they provide intuitive understanding about delamination and bulging on the unit of single-layer thickness.
- **Dynamic Modeling of Thrust Force and Torque:** For constructing the controller of thrust force and torque, the complicated drilling process must be simplified and modeled. We assume that both thrust force and torque are proportional to FPHR (Feed Per Half Revolution), which corresponds to an uncut chip thickness in the cases of turning and milling. The dynamic model of thrust force and torque with the concept of FPHR is utilized to obtain a discrete-time dynamic model.

- **Controller Design for Thrust Force and Torque:** PI controllers are designed for the dynamic models above. If a PI controller can work only for one specific condition of sampling time and spindle speed, it can not be applied in manufacturing. In our research, first, one PI controller is designed for one spindle speed condition using the corresponding dynamic model. Next, it is proved that the controller can be also used for various spindle speeds simply by changing the total gain. Root-locus techniques are used in the analysis. The design in this dissertation covers still a limited range of spindle speed, however the design procedure is clearly described here, and the method can be applied to many cases if the feed drive has similar dynamics.
- **Design of Supervisory Controller and Drilling Experiments:** The supervisory controller in our research chooses not only the best control strategy for each phase, but also the reference value and the controller gain that are suitable at each drill position. For the design of a practical supervisory controller, each phase must be clearly defined and the control strategy must be well considered. In our research, the drill position is used for deciding the phases, and the control strategy is determined using the results of characterization and analysis. In the experiments, a delamination-free drilling process controlled by the supervisor is given special emphasis.

### **1.3 Organization and Outline**

This dissertation is organized as follows. Chapter 2 starts with general description of conventional drilling followed by two important topics for this research, *i.e.* Shaw's equations of thrust force and torque, and delamination analysis by Hocheng and Dharan.

In Chapter 3, we describe the experimental setup, which includes a machining center, personal computers (PCs), a digital signal processor (DSP), an angle attachment, sensors and an air cleaning device.

Chapter 4 starts with characterization of thrust force and torque for the drilling of composite materials, followed by determination of the coefficients of Shaw's equations for drilling of carbon fiber reinforced laminates. Thrust force (or torque) per FPHR (Feed per Half Revolution) is introduced.

In Chapter 5, the identification of the feed mechanism of the machining center is described, and the design of position, thrust force and torque controllers is explained. Finally, a supervisory control scheme is proposed, which utilizes all of the above.

Chapter 6 is concerned with experiments for drilling of carbon fiber reinforced laminates. Specimen preparation methods and the material properties relevant to these specimens are explained, and experimental results are presented.

Conclusions and topics for future research are discussed in Chapter 7.



## **CHAPTER 2**

### **Drilling of Composite Materials**

In this chapter, the drilling process and issues concerning composite materials are discussed. Two important models relating to this research are explained; they are Shaw's model of thrust force and torque (Shaw and Oxford, 1957), and Hocheng and Dharan's model of delamination (Hocheng and Dharan, 1988). The thrust-force and/or torque values from these models will be utilized for both controller design and reference-value determination.

#### **2.1 Drilling**

The most common tool used in drilling is a conical point twist drill with two flutes, as shown in Fig. 2.1. This tool has three distinct types of cutting surfaces, *i.e.* a chisel edge, two main cutting edges and two marginal cutting edges. In our research, only the first two types of edges are considered, and we will refer to main cutting edges as cutting edges hereafter.

The machining action of the chisel edge is more like extrusion than cutting, particularly at the center of the edge. The chisel edge makes a significant contribution to the total thrust force at full engagement of the drill. On the other hand, the mechanism of cutting edges is like the cutting action of milling. The cutting edges remove the majority of material in a hole. For a drill with web length equal to 18 percent of its diameter (a typical value for conventional twist drills), the cutting edges remove almost 97 percent of

the hole material (Lee, 1989). Although the thrust force at the chisel edge is larger than that of the cutting edges, the torque of the chisel edge is much smaller than that of the cutting edges, because the chisel edge is located at the center of the drill.

In addition to the above-mentioned edges, a two-flute twist drill includes several other curves that fulfill different objectives. In our research, a lateral projection of a drill is simplified as a collection of five straight lines. In Fig. 2.2, the straight line CD is a simplified chisel edge; the real chisel edge is slightly convex and has an obtuse center point. The straight lines BC and DE are simplifications of the cutting edges; the real cutting edges are twisted, the projection of these parts for the real drill are generally convex, and the angles at points B, C, D and E are more obtuse. In our research, the point length  $P$  is defined as the distance between the line BE and the line CD, and the conical part is defined as the conic portion between the drill tip and the horizontal plane containing the line BE. The point length  $P$  cannot be precisely measured and the value varies among drills, even when they have the same diameter and product number.

Figure 2.3 shows the simplified two-dimensional drill and its relative position with respect to the top surface and the bottom surface of the workpiece. In our research, we only consider workpieces with flat top and bottom surfaces, and workpiece thicknesses are assumed greater than the drill point length (see Section 5.5.1 for the precise condition). The top and bottom surfaces are assumed to be perpendicular to the drilling direction. In general, there exist two transient phases in the drilling process. The first phase ranges from air cutting to full engagement of drilling at the top surface, and the second phase encompasses full drilling to air cutting at the bottom surface. The transient phases can be geometrically regarded as the stages of drilling in which the cutting edges,

*i.e.* the straight lines BC and DE of Fig. 2.2, intersect the line of the top surface or the line of the bottom surface. (From the viewpoint of thrust force response, the real transient drilling around the bottom surface starts slightly before the chisel edge CD reaches the bottom surface. See Fig. 5.10.)

In a drilling process with normal two-flute drills, the workpiece thickness is at most thirty times the point length. Hence, the transient phases account for a non-negligible percentage of the total process. In the cases of turning and milling, there also exists a corresponding transient period, *i.e.* when the edge touches the workpiece and begins cutting, and when the edge leaves the workpiece. The duration of these phases is, however, negligible if compared with the normal operating period. On the other hand, turning and milling can include sudden or gradual changes in the cutting conditions due to changes in radius, height or material properties of a workpiece. No corresponding changes exist for drilling, except when there is time-varying interference between the drill flutes and the drilled hole, or when there are changes in material properties of the composite materials. In normal drilling, it is reasonable to regard a sudden increase in thrust force as the result of drill breakage, a defect in the workpiece, or another fatal problem.

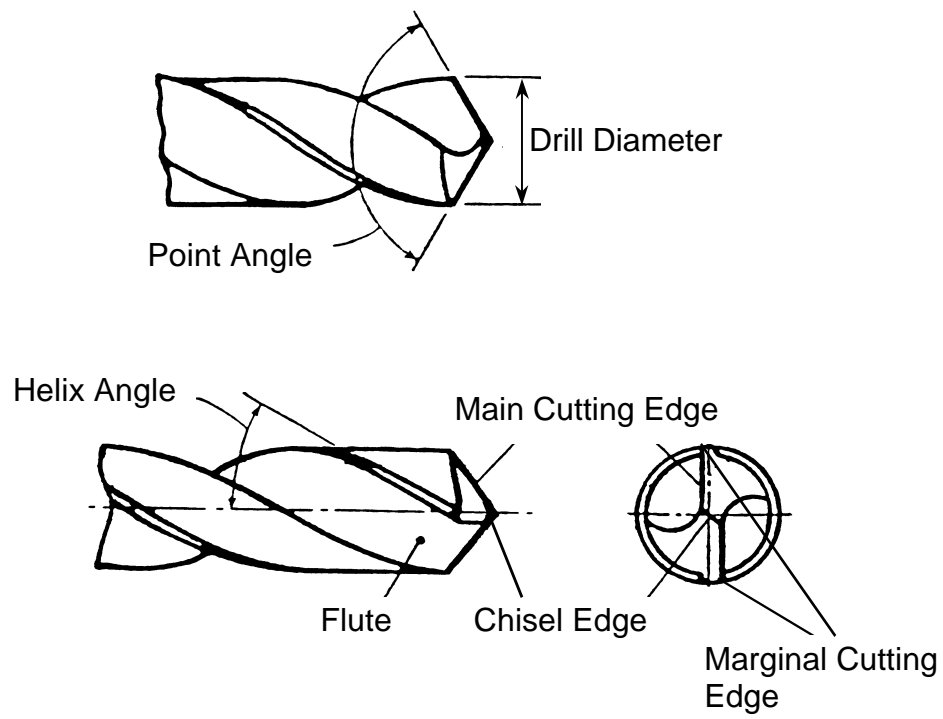


Fig. 2.1 Conical Point Twist Drill with Two Flutes.

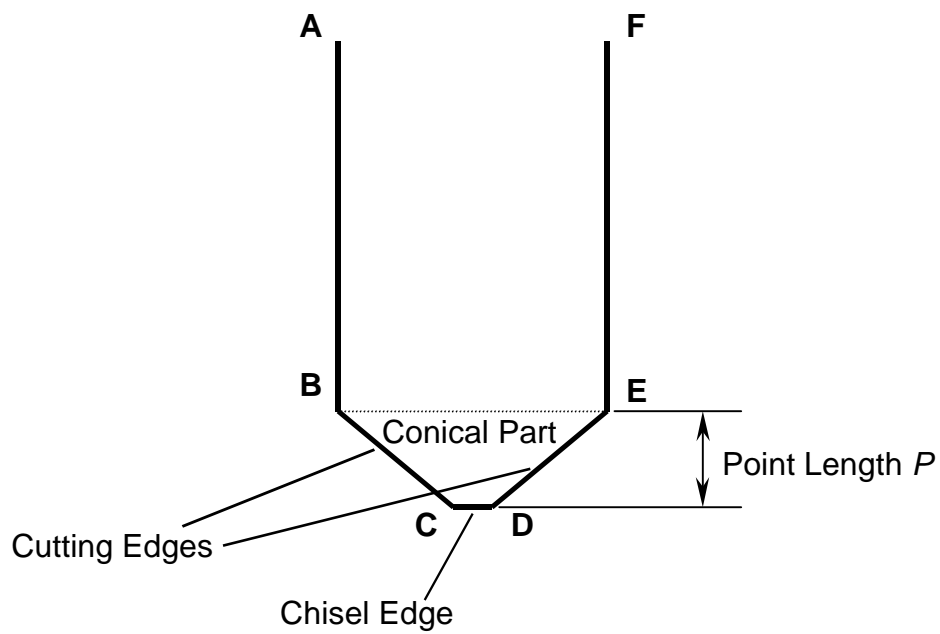


Fig. 2.2 Simplified Two-Dimensional Representation of Two-Flute Twist Drill.

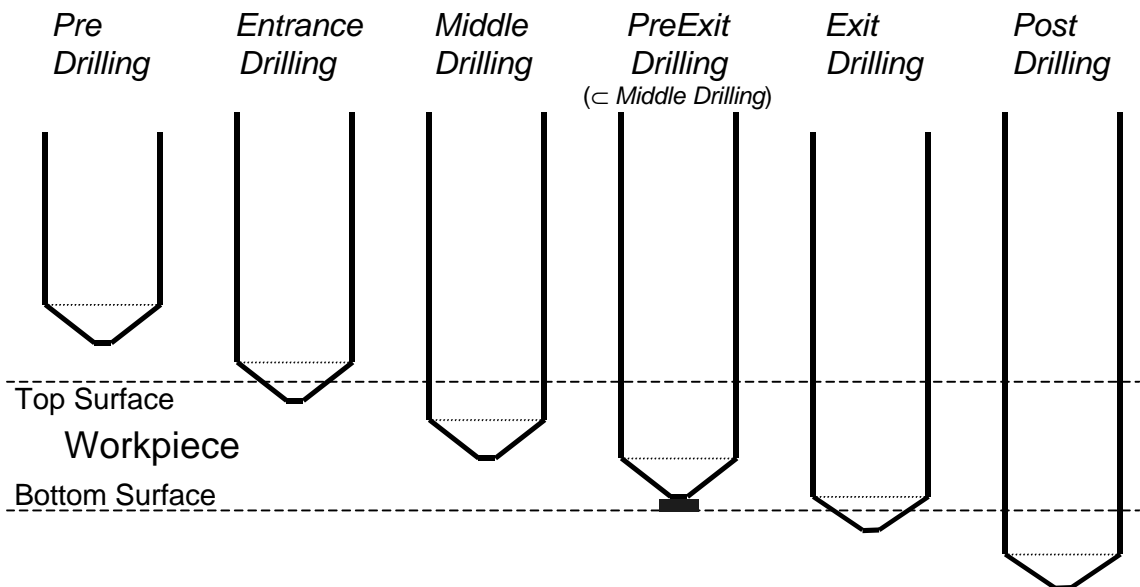


Fig. 2.3 Simplified Drill and Drilling Phases.

## 2.2 Shaw's Equations

Shaw and Oxford proposed empirical equations for thrust force and torque for a metal drilling process (Shaw and Oxford, 1957):

$$\frac{F_s}{d^2 H_B} = k_1 \frac{f^{1-a}}{d^{1+a}} \left[ \frac{1 - \frac{c}{d}}{\left(1 + \frac{c}{d}\right)^a} + k_2 \left(\frac{c}{d}\right)^{1-a} \right] + k_3 \left(\frac{c}{d}\right)^2 \quad (2.2.1)$$

$$\frac{T_s}{d^2 H_B} = k_4 \frac{f^{1-a}}{d^{1+a}} \left[ \frac{1 - \left(\frac{c}{d}\right)^2}{\left(1 + \frac{c}{d}\right)^a} + k_5 \left(\frac{c}{d}\right)^{2-a} \right] \quad (2.2.2)$$

where  $F_s$  is the thrust force,  $T_s$  is the torque,  $H_B$  is the workpiece material hardness,  $c$  is the chisel edge length,  $d$  is the drill diameter,  $f$  is the feed, and  $a$ ,  $k_1$ ,  $k_2$ ,  $k_3$ ,  $k_4$  and  $k_5$  are constants to be determined from experimental data. Capital 'S' subscripts on the thrust force and torque imply Shaw's equations, or related variables.

For the standard twist drills used in our research, the value of  $c/d$  is constant, therefore the thrust force and torque can be simply expressed as

$$F_s = K_1 (fd)^{1-a} + K_2 d^2 \quad (2.2.3)$$

$$T_s = K_3 f^{1-a} d^{2-a} \quad (2.2.4)$$

where  $K_1$ ,  $K_2$ , and  $K_3$  are new constants.

Shaw and Oxford derived another equation of torque. From the size-effect theory, the effective specific energy  $u$  is proportional to  $(fd)^{-a}$  by the relation:

$$u = \frac{8T_s}{fd^2} \propto (fd)^{-a} \quad (2.2.5)$$

Dharan *et al.* proposed that Eqs. (2.2.3) and (2.2.4) (with appropriate values of  $a$ ,  $K_1$ ,  $K_2$  and  $K_3$ ) could be used to predict the values of thrust force and torque during drilling of composite materials (Dharan, Tomizuka, Won, Ozaki and Sheng, 1998, see Section 4.1). Jain and Yang developed a thrust force equation (corresponding to Eq. (2.2.3)) from their experiments (Jain and Yang, 1992); the exponents they chose have values different from those obtained by Dharan *et al.* In general, equations that perfectly predict the thrust force or the torque will never exist for any machining processes due to many unknown factors, particularly friction, that greatly influence the thrust force and torque values. The main goal in seeking equations for thrust force or torque is to obtain good reference values and to design controllers that perform well.

## **2.3 Drilling of Fiber Reinforced Composite Laminates and Delamination Model**

### **2.3.1 Composite Laminates and Delamination**

Composite materials are materials that are composed of two or more constituent substances. Modern composite materials contain a reinforcement phase and a binder

phase; in many cases, composite materials consist of rigid and strong fibers in a compliant matrix (Swanson, 1997). The reinforcing material provides key structural properties. Frequently used fibrous reinforcements are glass, graphite, aramid, and boron. The matrix serves to hold the fibers together, to distribute the load between the fibers, and to protect the fibers from the environment. One of the most common matrix materials is epoxy, which provides the advantages of ease of wetting, nonvolatility, good thermal and dimensional stability, and high bond strength (Hocheng, 1988).

Composite materials are anisotropic, locally inhomogeneous, and are usually in laminate form when they are machined. Due to the anisotropy and local inhomogeneity, metal cutting techniques have to be modified when applied to composite laminates. Among all removal processes, the drilling process is most frequently applied to composite laminates; there is a 2.5 dimensional design freedom for the structure before the removal process is conducted, and drilling processes for future assembly have important roles.

### **2.3.2 Delamination Model and Hocheng-Dharan Equation for Push-out at Exit**

When a composite laminate is drilled, the laminae under the chisel edge are subject to local bending deformation, which can cause delamination around the hole just before the chisel edge exits. This is expressed as push-out at exit (see Fig. 2.4). It is easy to imagine that delamination requires smaller thrust force values as the uncut thickness becomes smaller, and that the last lamina is most easily delaminated. These intuitive predictions



should be mathematically modeled for controller design. The following is a model by Hocheng and Dharan (Hocheng and Dharan, 1988).

In Fig. 2.5, the cylinder in the middle represents the drill,  $D$  is the diameter of the drill,  $F$  is the thrust force,  $x$  is the tool displacement,  $H$  is the thickness of the structure,  $h$  is the uncut depth under the tool, and  $a$  is the assumed size of an existing crack. As the drill moves downward, the uncut laminae under the tool are pushed downward and deformed elastically by the thrust force. If the strain at the tip of the existing crack exceeds the critical value, crack propagation occurs. The equation of energy balance can be expressed as follows using linear elastic fracture mechanics:

$$2Gp(a + D/2)da = Fdx - dU \quad (2.3.1)$$

In this equation,  $G$  is the energy release rate per unit area,  $U$  is the stored strain energy, which is expressed as

$$U = \frac{8pMx^2}{(a + D/2)^2} \quad (2.3.2)$$

and  $x$  is the displacement of the drill, measured from the position at which delamination began.

In Eq. (2.3.2),  $M$  represents the flexural rigidity of the plate (under the drill).  $M$  is determined from plate bending theory for a circular plate with clamped ends and a concentrated central load. It is expressed as

$$M = \frac{Eh^3}{12(1-\nu^2)} \quad (2.3.3)$$

where  $E$  is the modulus of elasticity and  $\nu$  is Poisson's ratio. The displacement  $x$  in Eq. (2.3.1) and Eq. (2.3.2) can be expressed as

$$x = \frac{F(a + D/2)^2}{16pM} \quad (2.3.4)$$

using  $a$ ,  $F$  and  $M$  (Timoshenko, 1959).

Eq. (2.3.1) can, therefore, be modified to

$$\begin{aligned} 2Gp(a + D/2) &= F \frac{dx}{da} - \frac{dU}{da} = F \frac{d}{da} \frac{F(a + D/2)^2}{16pM} - \frac{d}{da} \frac{F^2(a + D/2)^2}{32pM} \\ &= \frac{F^2 \frac{d}{da} (a + D/2)^2}{32pM} = \frac{F^2(a + D/2)}{16pM} \end{aligned} \quad (2.3.5)$$

Hence, the critical thrust force for crack propagation (as a function of the uncut thickness  $h$ ) in push-out mode is expressed as follows:

$$F_{PushOut}(h) = F^*(h) = p \sqrt{32MG_{IC}} = p \sqrt{\frac{8G_{IC}Eh^3}{3(1-\nu^2)}} \quad (2.3.6)$$

To avoid delamination, the thrust force should not exceed this value. The critical thrust force is a function of only the uncut thickness  $h$  and material properties, and is proportional to  $h^{3/2}$ .

In Eq. (2.3.6), the value  $G_{IC}$  (critical energy release rate for delamination in model I) is used for  $G$ . The value of  $G_{IC}$  is lower than that for the plane stress case, which makes  $F_{PushOut}(h)$  smaller than the real value. Thus, Eq. (2.3.6) gives a conservative prediction (in the sense that real delamination may not occur at the predicted thrust force) for the critical thrust force (Hocheng and Dharan, 1988).

### **2.3.3 Delamination Model and Hocheng-Dharan Equation for Peel-up at Entrance**

In the entrance phase, cutting action of the spiraled cutting edges generates a peeling force in the upward direction, which may separate the upper lamina from the uncut portion. This corresponds to peel-up at entrance in Fig. 2.4. The transformation from the peripheral cutting force to the axial peeling force is a complex function of drill geometry and friction between the tool and the workpiece.

The critical peeling force  $F_p^*$  in the axial direction is related to the critical cutting force  $F_c^*$  as

$$k_p = \frac{F_c^*}{F_p^*} \quad (2.3.7)$$

where  $k_p$ , the peeling factor, is defined by  $\lambda$  (the helix angle at the drill tip) and  $m$  (the coefficient of friction between tool and workpiece).

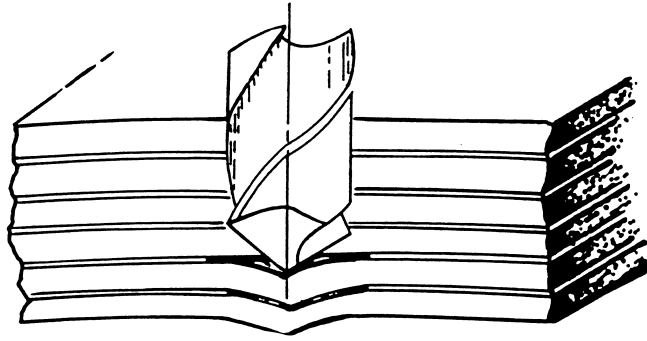
It is assumed that the mechanism behind tearing of laminates in Mode I fracture is also responsible for peel-up. Therefore, by substituting  $F^*$  of Eq. (2.3.6) into  $F_p^*$  of Eq. (2.3.7), and replacing the uncut thickness  $h$  with the hole depth  $h_d = H - h$ , the critical cutting force for the onset of delamination at entrance is obtained:

$$F_c^*(h) = k_p p \sqrt{\frac{8G_{IC}E(H-h)^3}{3(1-\nu^2)}} \quad (2.3.8)$$

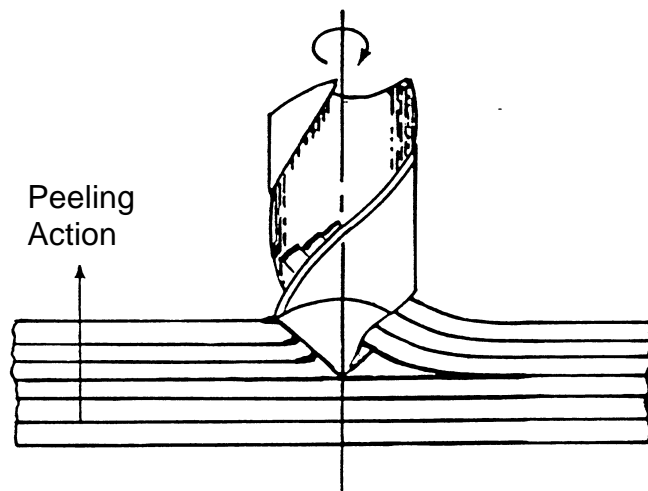
and the critical thrust force, expressed as

$$F_{PeelUp}(h) = p \sqrt{\frac{8G_{IC}E(H-h)^3}{3(1-\nu^2)}} \quad (2.3.9)$$

can be used as a more conservative solution for drilling without delamination.



(a) Push-out at Exit



(b) Peel-up at Entrance

Fig. 2.4 Drill Bit and Delamination (Hocheng and Dharan, 1988).

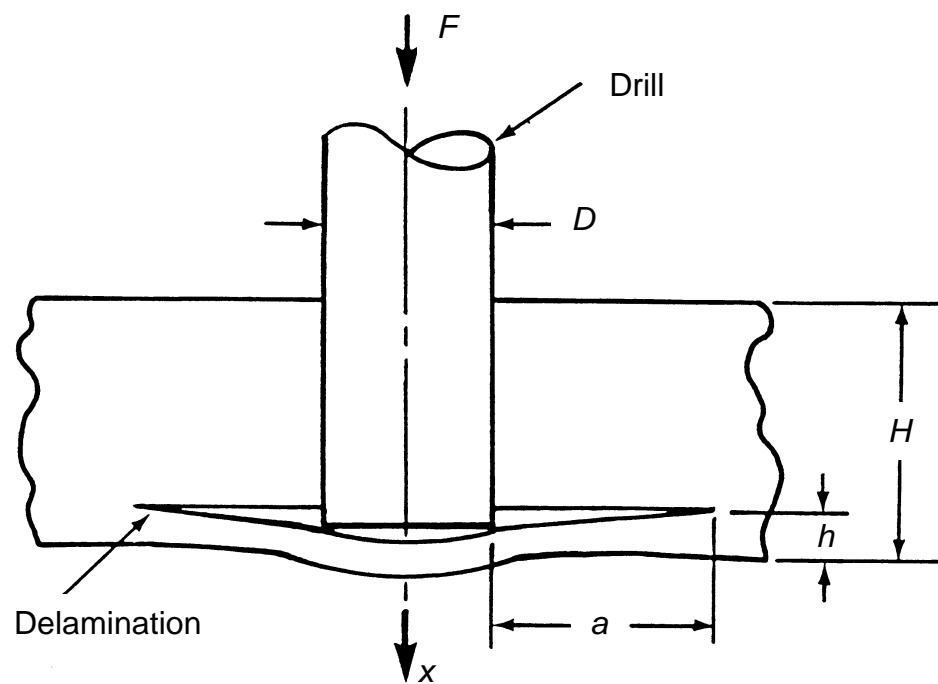


Fig. 2.5 Circular Plate Model for Delamination Analysis (Hocheng and Dharan, 1988).

## **2.4 Summary**

In this chapter, the drill structure and drilling processes were explained, and Shaw's empirical equations for thrust force and torque during drilling were introduced. The original equations were simplified into more concise equations, and another torque equation, derived from size-effect theory, was described. Finally, the drilling of composite materials and delamination were explained. Push-out at exit and peel-up at entrance are two delamination modes that should be considered in the drilling process. The models of Hocheng and Dharan were introduced, which give conservative thrust force values for delamination-free drilling as a function of drill position.

## **CHAPTER 3**

### **Experimental Setup**

In this chapter, the experimental setup used in this investigation is described. Section 3.1 introduces the machining center in which all drilling experiments were conducted. In Section 3.2, a PC-based machine tool controller is explained. Section 3.3 describes the drilling setup itself, *i.e.* the drills, the angle attachment, and the fixtures. Section 3.4 shows the sensors that were attached to the machining center for the present work. Finally, Section 3.5 explains air cleaning and dust collecting procedures used during the experiments; both air cleaning and dust collection are important because particles generated by machining of composite materials are hazardous to health.

#### **3.1 Matsuura MC510VSS Machining Center**

A Matsuura MC510VSS vertical machining center (Figs. 3.1 and 3.2) was used in all the drilling experiments described in this research. The machine has a spindle with 15,000 rpm maximum speed. A three-phase AC motor coupled with a ball screw moves each of X, Y and Z-axes. The X-axis mechanism resides on top of the Y-axis mechanism; each is constrained by a linear guide (Fig. 3.3), and together they construct an X-Y stage for the horizontal movement of the workpiece. The mechanism for the Z-axis moves the spindle head, and includes a counterweight that is connected to the head assembly with a metallic chain.



The MC510VSS machining center is equipped with a Yasnac MX-3 CNC controller, which provides closed-loop position control for each axis with a sampling time of 2 msec. An optical shaft encoder generates 12,000 counts per revolution and performs position sensing for each axis. A linear position measurement resolution of 1  $\mu\text{m}$  is obtained with the use of a 12 mm-lead ball-screw.

The coordinate system used in our research is the same as that of MC510VSS, *i.e.* the X-Y plane lies horizontally with the Y-axis toward the front door, and the Z-axis is upward.

### **3.2 PC-Based Machine Tool Controller** (Al-Majed, 1997)

The machining center's original controller, Yasnac MX-3, was replaced with an experimental control system, which allowed installation of many different control algorithms. The experimental control system receives optical encoder position signals from the feed drives and sends velocity commands to the servo packs during closed-loop position control (Al-Majed, 1997).

The control system consists of a DSP based on a TMS320C30 processor (Texas Instruments) and a PC based on an Intel 80486 processor. The DSP interacts with the machine tool servo packs through its four D/A converters and three other special I/O boards residing on the DSP-Link.

The voltage command sent to the servo pack (through the D/A converter) is equivalent to an analog velocity reference for the velocity loop. The allowable range for the velocity reference is  $\pm 10$  V, with +10 V corresponding to a command feedrate of 400 mm/sec.

The original servo packs for the feed drive provided Proportional-plus-Integral (PI) velocity control. In our research, each of the original servo packs was replaced with a remodeled servo pack without integral action, in order to construct a simple transfer function from voltage command to velocity.

The spindle speed is set by a voltage reference, whose signal is sent to the spindle servo pack of the machining center. The maximum voltage of 10V corresponds to the maximum spindle speed of 15,000 rpm.

One of the I/O boards on the DSP-Link has two A/D converters (with a 10  $\mu$ sec maximum conversion time), which receive analog signals from the sensors. The DSP board itself resides on the AT-bus of the 486 PC.

Figure 3.2 shows the controllers, all of which are located close to the machining center, and Fig. 3.4 shows a schematic figure of the experimental setup.

### **3.3 Setup Around the Drilling Process**

#### **3.3.1 Drills**

In our drilling experiments, carbide tipped drills were used. During machining of composite materials, a high-speed steel (HSS) tool suffers extreme wear, therefore an HSS tool is not economical, and does not provide constant conditions. Carbide offers a good compromise between tool life and production costs (Hocheng, 1988). The diameters of the drills used in our experiments were 6.35 mm (1/4"), 7.94 mm (5/16") and 9.53 mm (3/8"). The point lengths of the drills used in this research for supervisory-controlled drilling were about 1.5 mm, 2.3 mm and 2.5 mm, respectively. These large point lengths provide adequate time and distance for measurement when the cutting edges intersect

either the top surface or the bottom surface, *i.e.* in the phases of *Entrance Drilling* and *Exit Drilling*. The thickness of the workpieces used in our research was between 8 mm and 13 mm, which allows adequate time and distance to be taken for measurement when the entire conical part of the drill is engaged, *i.e.* during the *Middle Drilling* phase.

The dimensions of the drills, particularly point length, were measured with a contour projector (Optical Gaging Products, Model 30-826). The point length is an important value for the supervisory controller, because the supervisory controller uses the point length values to decide certain drilling phases. However, it is true that the point length is not constant among drills, even if the drills have the same product number. Also the point length may change after a drill is used repeatedly. Before any drilling took place, the point lengths of the drills used in the supervisory-controlled drilling experiments were  $1.50 \text{ mm} \pm 0.07 \text{ mm}$ ,  $2.27 \text{ mm} \pm 0.25 \text{ mm}$ , and  $2.54 \text{ mm} \pm 0.28 \text{ mm}$ , for 6.35 mm, 7.94 mm, and 9.53 mm drill, respectively. The heights of the chisel edges (the axial distance between the center tip and the crosspoints of the chisel edge and the cutting edges) were  $0.051 \text{ mm} \pm 0.005 \text{ mm}$ ,  $0.070 \text{ mm} \pm 0.006 \text{ mm}$ , and  $0.114 \text{ mm} \pm 0.015 \text{ mm}$ , respectively.

### **3.3.2 Angle Attachment**

The machining center's original drilling direction was the Z-axis (the vertical axis). There is about a 4 msec delay for Z-axis movement. On the other hand, the X-axis and the Y-axis have relatively small time delays. This difference arises from differences in the mechanical configurations of the axes, as described in Section 3.1. Thus, to reduce delays, an angle attachment (Alberti Umberto, T90cn) was inserted in the spindle, and the drilling direction was changed from the Z-axis to the Y-axis. In this new setup, the drill

point was aligned to face the front door of the machining center. This is shown in Fig. 3.5 (a) and (b). The reason for choosing the Y-axis (instead of the X-axis) and the drill point direction, was for the future possibility of observing the bottom surface through the dynamometer in real time. This could be done by attaching measurement instruments, such as a video camera, to the bottom of the dynamometer (Dipaolo *et al.*, 1993).

### 3.3.3 Fixtures

The workpiece must be held in a rigid fixture during drilling. Two fixtures are shown in Figs. 3.4 and 3.5. Fixture 1 is attached to the top of the dynamometer and holds a specimen. The size of specimens that can be attached to this fixture is 6 ~ 20 mm in thickness, 38 ~ 51 mm in width, and 100 ~ 300 mm in length. Fixture 2 is attached to the X-Y stage, and holds the dynamometer with the dynamometer's axial direction parallel to the Y-axis, *i.e.* parallel to the drill.

## 3.4 Sensors

The board attached to the DSP board has two A/D converters, and the system can measure two of the following analog signals during the drilling process:

- **Dynamometer**

A dynamometer, Kistler 9271A, measures thrust force and torque. Each of the two outputs is amplified by a charge amplifier, Kistler 5004. The outputs of the charge amplifiers are sent to the A/D converters (through appropriate low-pass filters in the case of thrust force or torque control).

- Linear Sensor (not shown in the figures)

A linear variable differential transformer (LVDT), Shaevitz 1000HR, was attached to the setup. Its linear range is  $\pm 25.4$  mm. The LVDT body (f 20.6 mm  $\times$  168.4 mm) was attached to Fixture 2 via another fixture. The LVDT core (f 6.35 mm  $\times$  101.6 mm) was fixed to the flange of the head assembly with another rod, and was kept inside the LVDT body. The LVDT signal was sent to an amplifier, ATA-2001, whose output was sent to the A/D converter. This configuration made it possible to measure directly the relative displacements of the specimen and the drill.

- Electric Contact

A electric circuit consisting of one battery detects the moment when the point of the drill contacts the strip of aluminum foil attached to a composite material specimen (Dipaolo *et al.*, 1993), or a metal specimen insulated from the machining center.

### **3.5 Air Cleaning and Dust Collecting**

Any dust generated during drilling of composite materials is hazardous to one's health and must be prevented from spreading into the laboratory room. Some additional modifications were made to the machining center for this reason.

A high-pressure-air-driven vacuum cleaner was placed beside the machining center, and the hose of the vacuum cleaner was attached near the region of the drilling process. No coolant was used during drilling experiments, and all of the smaller, powder-like chips generated by drilling were collected by the vacuum hose.

The upper open space of the machining center was closed with a vinyl sheet to isolate the drilling space from the outside. An air cleaner was inserted into the machining center and was run continuously during and after drilling.

Operators of the experiments always wore masks with particulate filters.

### **3.6 Summary**

The Matsuura machining center MC510VSS was modified to apply position control and other sensor-based control, such as thrust force and torque controls. The machining center's original main controller was replaced with a DSP controller, on which experimental control programs were run. An angle attachment was inserted into the spindle and the drilling direction was changed to the horizontal Y-axis, to allow for a simpler transfer function in position, thrust force and torque control. Additional modifications were made to minimize dust; dust reduction is an important issue in the machining of composite materials.

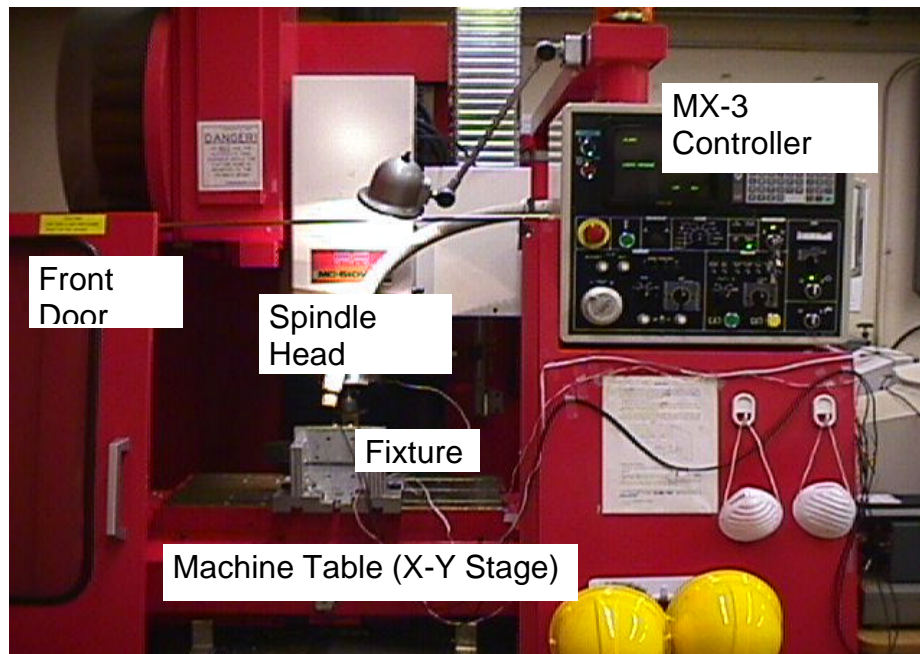


Fig. 3.1 Matsuura Vertical Machining Center MC510VSS.

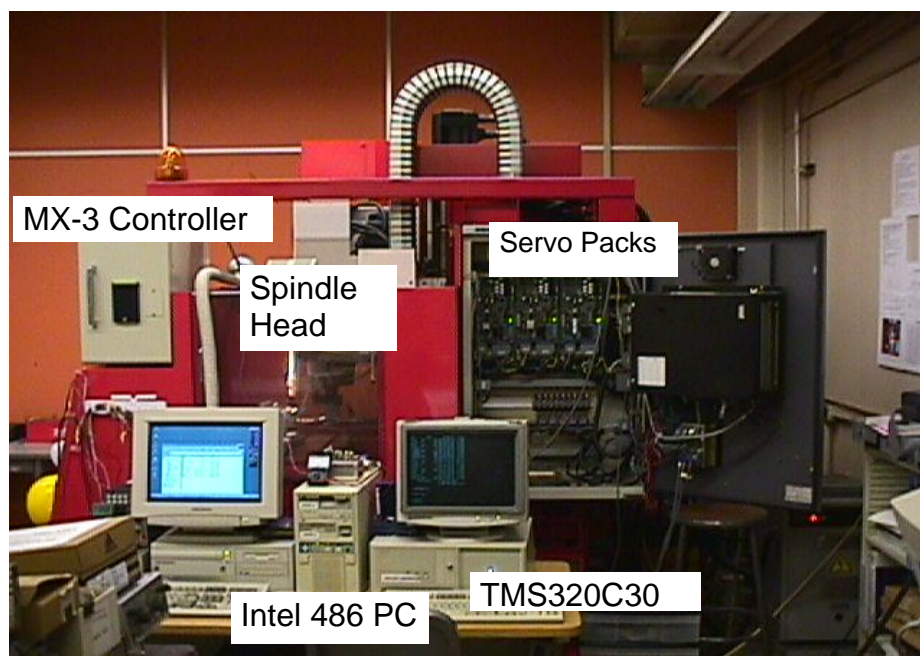


Fig. 3.2 Machining Center MC510VSS and Controllers.

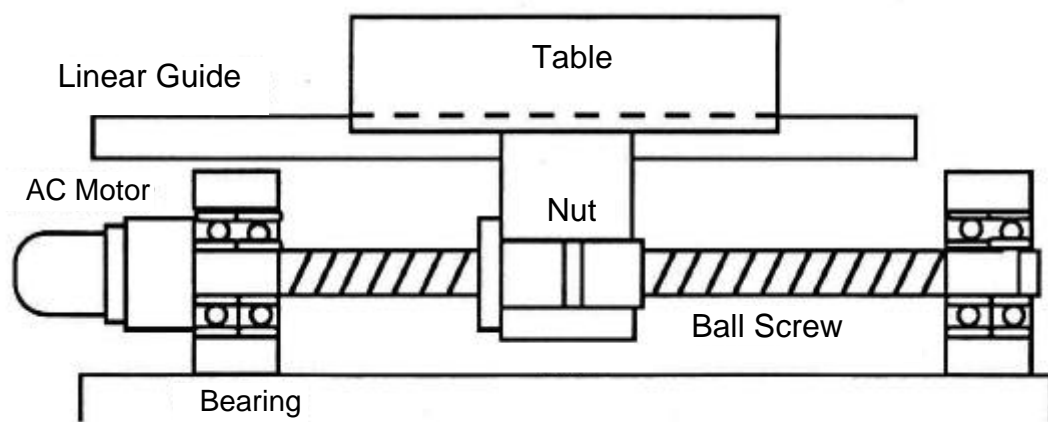


Fig. 3.3 Drive Train Elements for a Single Axis of the Machine Tool X-Y Table (Tung, 1993).



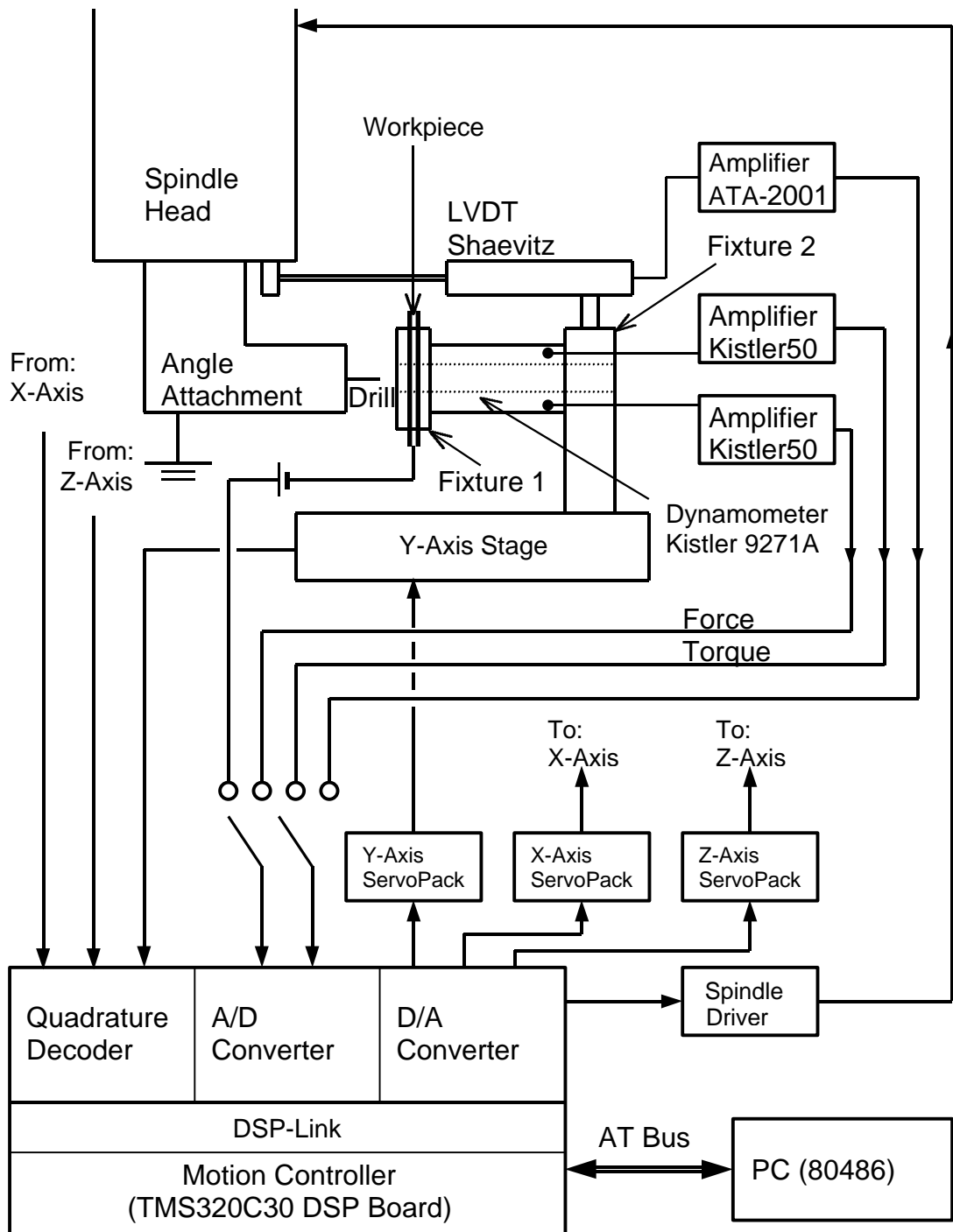
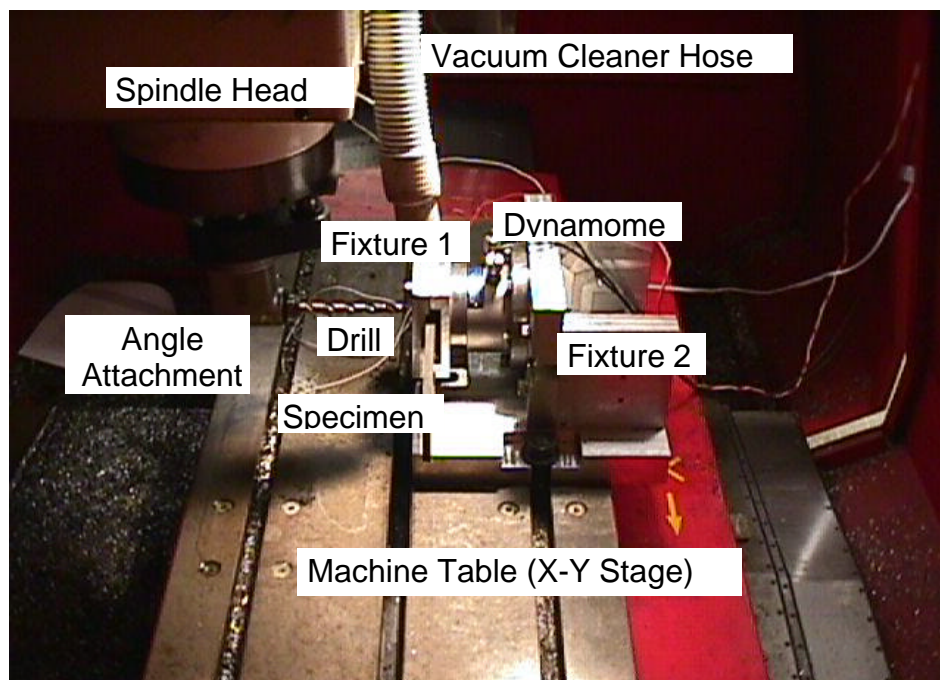
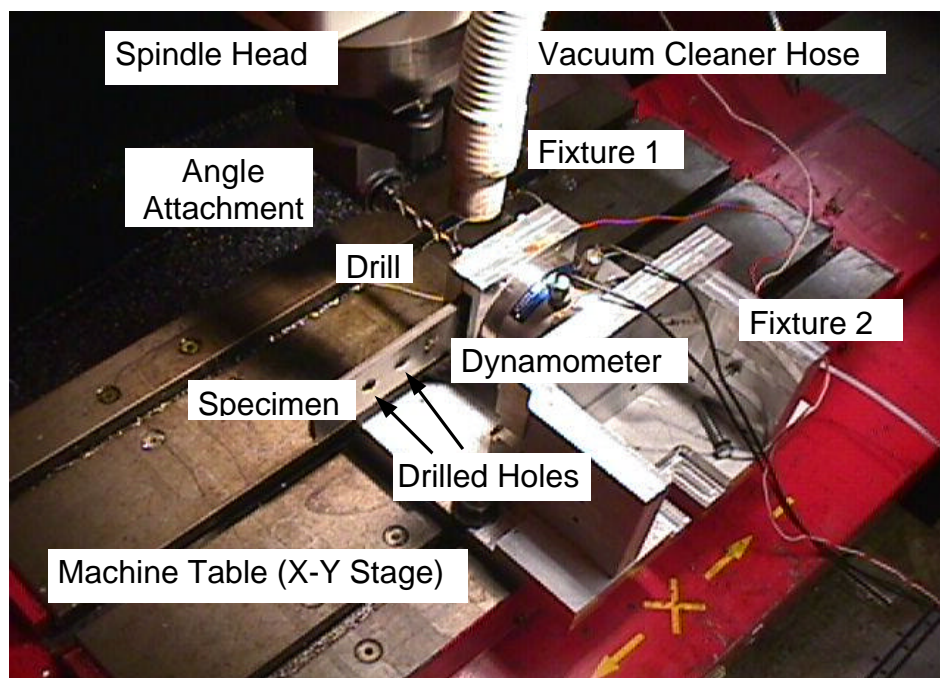


Fig. 3.4 Schematic Figure of the Experimental Setup.



(a)



(b)

Fig. 3.5 Experimental Setup. (Drill, Angle Attachment, Specimen, Fixtures, etc.)

## **CHAPTER 4**

### **Characterization of Thrust Force and Torque During Drilling of Carbon Fiber Reinforced Laminates**

In this chapter, the characterization of thrust force and torque is discussed. This characterization is important for the controls described in the next chapter. Section 4.1 gives the characterization of the thrust force and torque curves for constant feedrate drilling. Both curves (especially the thrust force curve) have distinctive features which are helpful in controller design. Section 4.2 develops Shaw's equations from experimental data, and considers the values of thrust force (or torque) per FPHR (Feed Per Half Revolution). Section 4.3 describes the thrust force during the *PreExit Drilling* phase; special attention is given to the exit thrust force (the thrust force just when the chisel edge reaches the bottom surface), in comparison with the thrust force of the discrete Hocheng-Dharan equations, which will be introduced in this chapter. Section 4.4 is a summary of this chapter.

#### **4.1 Characterization of Thrust Force and Torque Curves**

Figure 4.1 (a) and (b) show typical measurements of thrust force and torque, plotted with respect to the hole depth. Note that for constant feedrate drilling, the hole depth is nothing but scaled time. The drill used in these measurements was carbide tipped, 6.35 mm in diameter, with a point length of 1.9 mm. The specimen was 9.78 mm in thickness,

with a lay-up of  $[0/45]_{39S}$ . The feedrate was 100mm/min. Figure 4.1 (c) and (d) are the thrust force and torque, idealized and simplified by straight-line segments (Dharan, Tomizuka, Won, Ozaki and Sheng, 1998).

Figure 4.1 (c) is interpreted as follows. Just after contact of the chisel edge with the top surface (Point A), the thrust force rises sharply (Segment AB). This agrees with the fact that the chisel edge is responsible for more than 50% of the total thrust force at full engagement of the drill. It takes less than 0.2 mm to attain full influence of the chisel edge, while the thickness of one lamina is 0.127 mm. Hence, at Point B, the tip of the chisel edge has not even reached the third layer from the top surface. It is not clear whether peel-up delamination by the spiral action of the cutting edges (there is no peel-up delamination by the extrusion action of the chisel edge) can still occur in Segment AB, nor whether it is only the chisel edge that works in Segment AB. For these problems, it is important to consider not only the convexity of the chisel edge, but also deformation of the first few laminae, which is caused by the chisel edge.

Next, there is a gradual rise, which is caused by the gradual increase of the working part of the cutting edges (Segment BC). Segment CD, where the conical part is inside the workpiece, shows a mild decrease in thrust force; this is due to the lifting of the specimen that results from the contact force between the flutes of the drill and the wall of the hole already drilled. The sudden drop along Segment DE is attributed to delamination and/or bulging of the uncut part under the chisel edge that occurs when the uncut thickness becomes small. The uncut thickness at Point D is more than 0.4 mm, which means at least three layers must have suffered some deformation.

At Point E, the chisel edge is at the same height as the bottom surface of the workpiece. After this point, the chisel edge has no effect on drilling. There is a noticeable change in slope corresponding to this location (the position is calculated from the workpiece thickness and the contact position; the contact position is defined as the drill position where the chisel edge touches the top surface). In the case of ductile materials, the thrust force at the chisel edge does not vanish instantly at Point E; rather, the thrust force remains until the deformed material is cut by the cutting edges. Kim, Dornfeld and Furness have considered the phenomenon from the viewpoint of its relation to burr-formation (Kim, Dornfeld and Furness, 1999). This type of deformation does not occur during the drilling of brittle materials, such as carbon fiber reinforced laminates.

As the conical part passes through the bottom surface, the thrust force decreases gradually along Segment EF, due to the gradual reduction in the thrust force acting on the cutting edges. The distance between Point E and Point F is almost the same as the point length of the drill, although Point F can not be clearly found in the graph because of the small residual thrust force after Point F.

In the graph of Fig. 4.1 (c), two new values are defined. The entrance thrust force is the thrust force at Point B and the exit thrust force is the thrust force at Point E. The exit thrust force can be clearly defined in the experimental data as the thrust force when the chisel edge reaches the position of the bottom surface. The entrance thrust force, however, is hard to determine because (1) the thrust force does not increase exactly when the chisel edge touches the top surface (Point A) and (2) the drill must advance an unknown, yet very small distance to Point B to attain the total effect of the chisel edge. This ambiguity

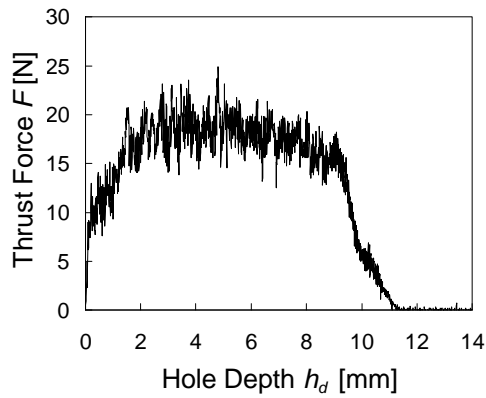
is also related to the difficulties in analyzing peel-up delamination, a phenomenon that was discussed earlier.

Next, the simplified torque graph of Fig. 4.1 (d) is interpreted. Here, the curve shape is not as straightforward as that of thrust force. The torque increases in Segment OP without a sudden rise, as increasing amounts of the cutting edges engage in cutting. This shows that the torque acting on the chisel edge is very small. There is a gradual rise in Segment PQ during the full engagement of the drill, due to the increase in the contact area between the drill and the inside of the drilled hole. In Segment PQ, it is difficult to find a sudden decrease of torque similar to that of Segment DE in the thrust force graph.

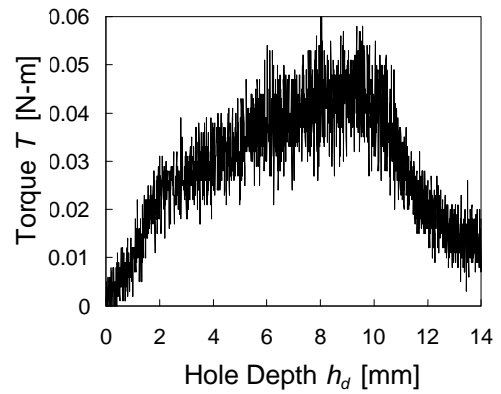
The chisel edge is at the bottom surface at Point Q. As the drill emerges from the bottom surface, the torque decreases in Segment QR due to the decrease of the working part of the cutting edges. When the cutting edges exit completely from the specimen, the torque has non-zero residual value in Segment RS due to the contact force between the two flutes of the drill and the inside wall of the drilled hole.

The torque curve shows that constant torque control for drilling can be useful in general manufacturing, because it will prevent the increase of torque that causes fast drill wear and drill breakage, which are problems when the workpiece thickness is large.

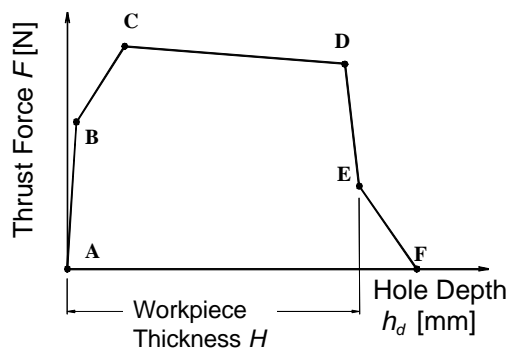
The thrust force curve for constant feedrate has some peculiar characteristics, when plotted as a function of position. Also, the thrust force is closely related to delamination. These two issues, Shaw's equations, the dynamic model of FPHR, and supervisory control are the main topics of this dissertation.



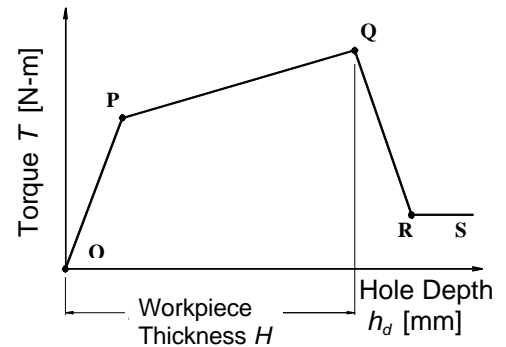
(a) Thrust Force



(b) Torque



(c) Simplified Graph of Thrust Force



(d) Simplified Graph of Torque

Fig. 4.1 Measured Thrust Force and Torque During the Drilling of Carbon Fiber Reinforced Laminate, and the Simplified Graph Shapes. (Modified from Dharan, Tomizuka, Won, Ozaki and Sheng, 1998.)

## 4.2 Thrust Force and Torque at Constant Feedrate Drilling and Shaw's Equations

Table 4.1 shows experimental data of the measured thrust force and torque with various constant feedrates and three drill diameters, and also shows the values calculated using Shaw's equations (the latter will be discussed later). The specimen is 9.78 mm in thickness with a lay-up of  $[0/45]_{39S}$  (the same as in Section 4.1).  $F$  and  $T$  are average values of thrust force and torque, respectively, during the full engagement of the drill.  $F_{Cutting}$  and  $T_{Cutting}$  are average values during full engagement for the specimens with pre-drilled pilot holes; the diameters of the pilot holes are the same as the chisel edge's length. The thrust force and torque for a specimen with a pilot hole are assumed to be acting on the cutting edges. The value of thrust force acting on the chisel edge,  $F_{Chisel}$ , can be estimated by subtracting  $F_{Cutting}$  from  $F$ . The percentages in parentheses express the ratios of  $F_{Chisel}$  to  $F$ .

In Table 4.1, the chisel edge thrust force is more than half of the total thrust force, except for a few cases at lower feeds; it is clear that the ratio of the chisel edge thrust force increases as the feed increases. For a constant feed, the relation between the chisel edge thrust force  $F_{Chisel}$  and the diameter  $d$  is not strictly increasing or decreasing. The thrust force at the chisel edge and the thrust force at the cutting edges are not independent of one another, because there are many mutual relations between their mechanisms. For example, the chips formed by the extrusion mechanism of the chisel edge are also pushed away by the cutting edges; this process influences the thrust forces at both types of edges. For these reasons, our calculated values are not exactly equal to the real values, which cannot be measured by any means.



As seen in Table 4.1, the difference between  $T$  and  $T_{Cutting}$  is negligible. This is due to the fact that the chisel edge is located at the center, and therefore cannot generate much torque, even if the thrust force at the chisel edge is larger than that at cutting edges.

The following two empirical relationships were introduced in Section 2.2 as Eqs. (2.2.3) and (2.2.4):

$$F_s(f, d) = K_1 (fd)^{1-a} + K_2 d^2 \quad (4.2.1)$$

$$T_s(f, d) = K_3 f^{1-a} d^{2-a} \quad (4.2.2)$$

where  $F_s$  is the thrust force in [N],  $T_s$  is the torque in [N-m], and  $a$ ,  $K_1$ ,  $K_2$  and  $K_3$  are dimensional constants to be determined. The drill diameter  $d$  and feed  $f$  are expressed in [mm] and [mm/rev], respectively. (In this dissertation, Shaw's equations use units of [mm], while all control-related calculations use [ $\mu$ m], except for the torque, which is in [N-m] for both cases.) Another equation was also introduced as Eq. (2.2.5):

$$u = \frac{8T_s}{fd^2} \propto (fd)^{-a} \quad (4.2.3)$$

The experimental data of Table 4.1 can be used to determine the unknown values  $a$ ,  $K_1$ ,  $K_2$  and  $K_3$  (Dharan *et al.*, 1998). The slope of the line of  $\log u$  against  $\log(fd)$  is used to determine  $-a$  from Eq. (4.2.3) (by applying the least squares method). Then,  $K_1$  and  $K_2$  can be determined from Eq. (4.2.1), and  $K_3$  from Eq. (4.2.2), also by the least squares

method. The following values were obtained from the  $F$  and  $T$  values in Table 4.1:  $a=0.4011$ ,  $K_1=31.31$ ,  $K_2=-0.0571$  and  $K_3=0.0069$ . Figure 4.2 shows the  $F$  and  $T$  values from Table 4.1 (where a different symbol is used for each drill diameter), along with  $F_s$  and  $T_s$  from Shaw's equations (a different line type is used for each case). The two rightmost columns of Table 4.1 give the values of thrust force and torque calculated from Shaw's equations, using the above-mentioned values of  $a$ ,  $K_1$ ,  $K_2$  and  $K_3$ . The thrust force and torque results from Shaw's equations show good agreement with the experimental data, in the feed range of 0.1 ~ 0.5 mm/rev.

The data for feeds greater than 0.7 mm/rev were eliminated from the calculations, because they were not consistent with the results from Shaw's equations for smaller feeds. A possible reason for the inconsistency is that during the full engagement of the drill, thrust force and torque cannot be measured effectively when the feedrate is large. For example, a feed of 0.7 mm/rev corresponds to more than 11 mm/sec of feedrate, at a spindle speed of 1,000 rpm. Another reason could be the inherent limitation of Shaw's equations, which were developed for small feedrates. It should be noted that Shaw's equations are essentially power-law empirical equations originally developed for metals.

Thrust force data from Table 4.1 can be used for estimating a time varying parameter  $K_{F_{phr} \rightarrow Force}$  [N/ $\mu$ m] (thrust force per FPHR; FPHR: Feed Per Half Revolution) that appears in Eq. (5.3.2). For a constant feed  $\bar{f}$ ,

$$K_{F_{phr} \rightarrow Force}(\bar{f}, d) = \frac{F(\bar{f}, d)}{\bar{f}_{phr}} = 2 \cdot \frac{F(\bar{f}, d)}{1000 \cdot \bar{f}} = 0.002 \frac{F(\bar{f}, d)}{\bar{f}} \quad (4.2.4)$$

where a factor of 2 has been introduced because FPHR is half of the feed at steady state, and 1/1000 accounts for the change of units from [mm] to [ $\mu\text{m}$ ]. In this chapter, the upper bars signify constant values. Similarly,  $K_{Fphr \rightarrow Torque}$  [N-m/ $\mu\text{m}$ ] (torque per FPHR) of Eq. (5.4.1) can be estimated as

$$K_{Fphr \rightarrow Torque}(\bar{f}, d) = \frac{T(\bar{f}, d)}{\bar{f}_{phr}} = 0.002 \frac{T(\bar{f}, d)}{\bar{f}} \quad (4.2.5)$$

Figure 4.3 shows values for  $K_{Fphr \rightarrow Force}$  and  $K_{Fphr \rightarrow Torque}$ ; these values are calculated by substituting  $F$  and  $T$  from Table 4.1 into Eq. (4.2.4) and Eq. (4.2.5), using the Shaw's equations' values of  $F_s$  from Eq. (4.2.1) and  $T_s$  from Eq. (4.2.2). The values of  $K_{Fphr \rightarrow Force}$  and  $K_{Fphr \rightarrow Torque}$  increase as the feed decreases.

Figure 4.4 shows  $F_{Chisel}$  and  $F_{Cutting}$  from Table 4.1. As mentioned above, the values of  $F_{Chisel}$  do not follow a monotonic relationship over the three different diameters. Comparisons of  $F_{Chisel}$  and  $F$  are only meaningful for the same values of diameter and feed. However, it can be observed that  $F_{Chisel}$  has a relatively constant value for different diameters of the drill. In the graph of Fig.4.1 (a), the entrance thrust force cannot be well defined (as discussed before), but it may be approximated by the chisel edge thrust force,  $F_{Chisel}$ , although this value is not reliable, either. The exit thrust force can also be approximated by the cutting edge thrust force,  $F_{Cutting}$ . This will be discussed in Subsection 4.3.2 and Subsection 5.5.2.

Figure 4.5 shows the calculated values of  $K_{F_{phr} \rightarrow ForceChisel}$  and  $K_{F_{phr} \rightarrow ForceCutting}$  when the values of  $F_{Chisel}$  and  $F_{Cutting}$  from Table 4.1 are successively substituted into Eq. (4.2.4) (instead of  $F$ ),

$$K_{F_{phr} \rightarrow ForceChisel}(\bar{f}, d) = \frac{F_{Chisel}(\bar{f}, d)}{\bar{f}_{phr}} = 0.002 \frac{F_{Chisel}(\bar{f}, d)}{\bar{f}} \quad (4.2.6)$$

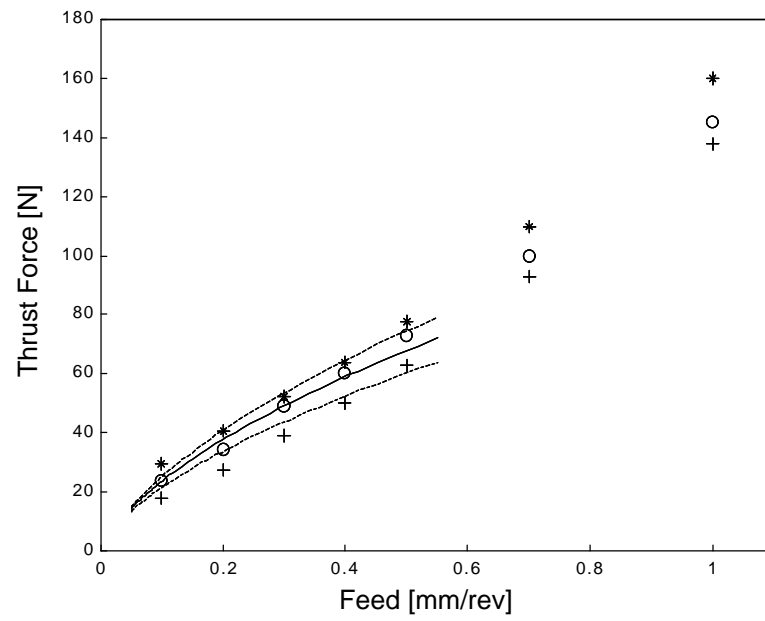
$$K_{F_{phr} \rightarrow ForceCutting}(\bar{f}, d) = \frac{F_{Cutting}(\bar{f}, d)}{\bar{f}_{phr}} = 0.002 \frac{F_{Cutting}(\bar{f}, d)}{\bar{f}} \quad (4.2.7)$$

The sum of these two values is the same as  $K_{F_{phr} \rightarrow Force}$  of Eq. (4.2.4).  $K_{F_{phr} \rightarrow ForceCutting}$  was obtained from the real experimental values of  $F_{Cutting}$ , therefore it has a real physical meaning, while  $K_{F_{phr} \rightarrow ForceChisel}$  does not.  $K_{F_{phr} \rightarrow ForceCutting}$  becomes larger as the feed becomes smaller. On the other hand, the plot of  $K_{F_{phr} \rightarrow ForceChisel}$  shows that the value remains within the range of 0.14 ~ 0.24 N/μm, and is relatively constant around 0.20 ~ 0.22 N/μm for high feed values, independent of the diameter.

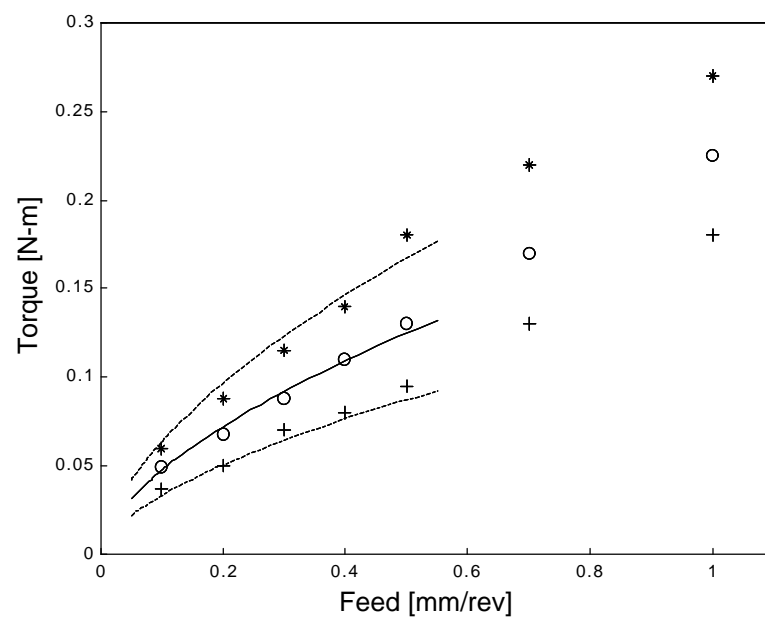
Table 4.1 Measured and Calculated Thrust Force and Torque. (Modified from Dharan, Tomizuka, Won, Ozaki and Sheng, 1998.)

Dia. $D$ (mm)	Feed $f$ (mm/rev)	Measured Forces					Calculated Forces	
		Force(N)		$F_{Chisel}$ (= $F - F_{Cutting}$ )	Torque(N-m)		Force(N)	Trq.(N-m)
		$F$ (.)	$F_{Cutting}$ (..)		$T$ (.)	$T_{Cutting}$ (..)	$F^S$	$T^S$
6.35 (1/4")	0.1	17.8	7.1	10.7(60.1%)	0.037	0.038	21.6	0.033
	0.2	27.5	8.1	19.4 (70.5%)	0.050	0.048	33.8	0.051
	0.3	39.0	9.0	30.0 (76.9%)	0.070	0.065	43.8	0.065
	0.4	50.0	10.5	39.5 (79.0%)	0.080	0.077	52.4	0.077
	0.5	63.0	11.5	51.5 (81.7%)	0.095	0.092	60.3	0.088
	0.7	93.0	13.7	79.3 (85.3%)	0.130	0.120	—	—
	1.0	138.0	17.5	120.5 (87.3%)	0.180	0.165	—	—
7.94 (5/16")	0.1	23.5	11.2	12.3 (52.3%)	0.049	0.050	23.7	0.048
	0.2	34.3	12.5	21.8 (63.6%)	0.068	0.065	37.7	0.072
	0.3	49.0	13.5	35.5 (72.4%)	0.088	0.090	49.1	0.092
	0.4	60.0	14.0	46.0 (76.7%)	0.110	0.110	59.0	0.109
	0.5	73.0	15.0	58.0 (79.5%)	0.130	0.130	67.9	0.125
	0.7	100.0	17.0	83.0 (83.0%)	0.170	0.160	—	—
	1.0	145.0	19.7	125.3 (86.4%)	0.225	0.220	—	—
9.53 (3/8")	0.1	29.3	22.0	7.3 (24.9%)	0.060	0.060	25.2	0.064
	0.2	40.8	24.0	16.8 (41.2%)	0.088	0.080	40.9	0.097
	0.3	52.0	26.0	26.0 (50.0%)	0.115	0.110	53.6	0.123
	0.4	64.0	27.0	37.0 (57.8%)	0.140	0.130	64.6	0.146
	0.5	77.5	28.5	49.0 (63.2%)	0.180	0.165	74.6	0.167
	0.7	110.0	30.5	79.5 (72.3%)	0.220	0.210	—	—
	1.0	160.0	35.0	125.0(78.1%)	0.270	0.260	—	—

\* without pilot holes, \*\* with pilot holes

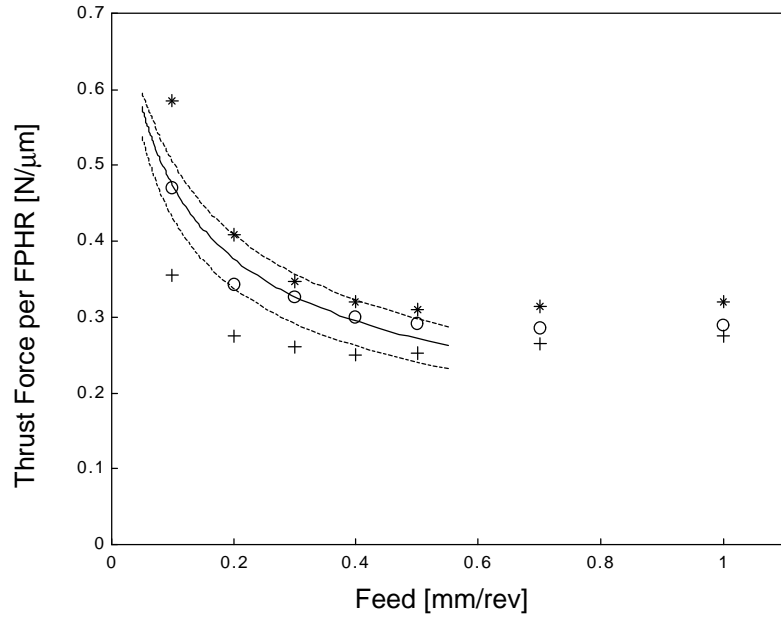


(a) Thrust Force  $F$

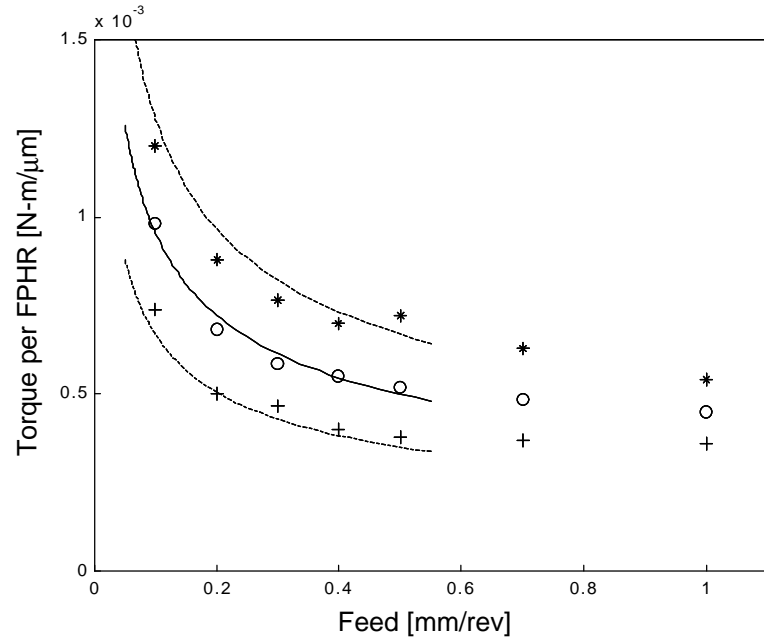


(b) Torque  $T$

Fig. 4.2 Thrust Force and Torque Given by Experimental Data and Shaw's Equations.  
 (+ - - - - : 6.35 mm dia., o — : 7.94 mm dia., and \* ..... : 9.35 mm dia.)

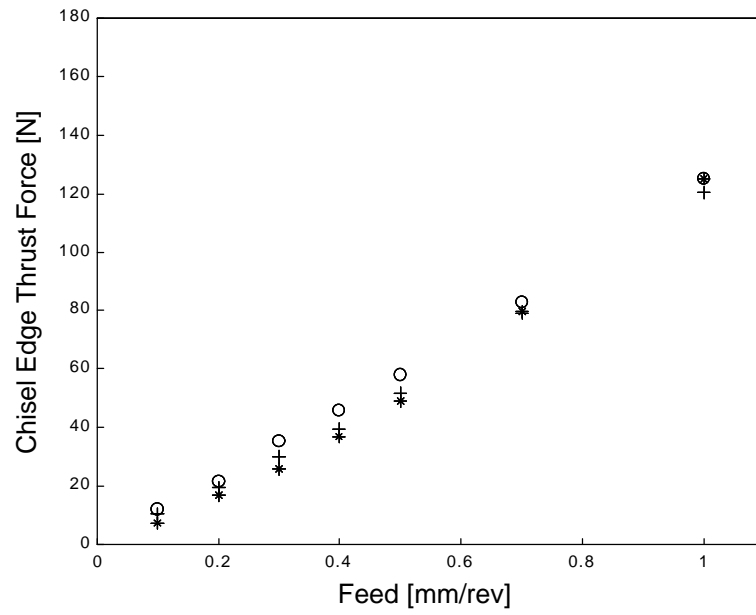


(a) Thrust Force per FPHR  $K_{Fphr \rightarrow Force}$

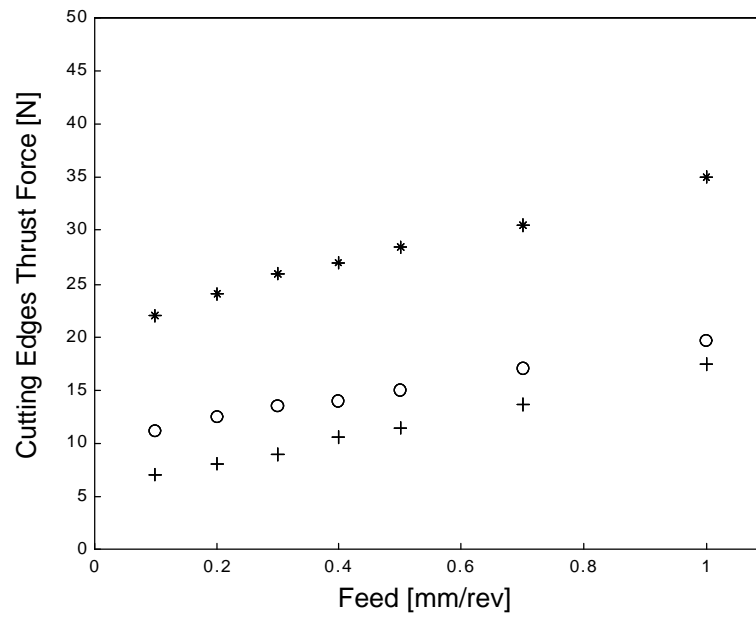


(b) Torque per FPHR  $K_{Fphr \rightarrow Torque}$

Fig. 4.3  $K_{Fphr \rightarrow Force}$  and  $K_{Fphr \rightarrow Torque}$  Calculated from Experimental Data and Shaw's Equations. (+ - - - - : 6.35 mm dia., o — : 7.94 mm dia., and \* ..... : 9.35 mm dia.)



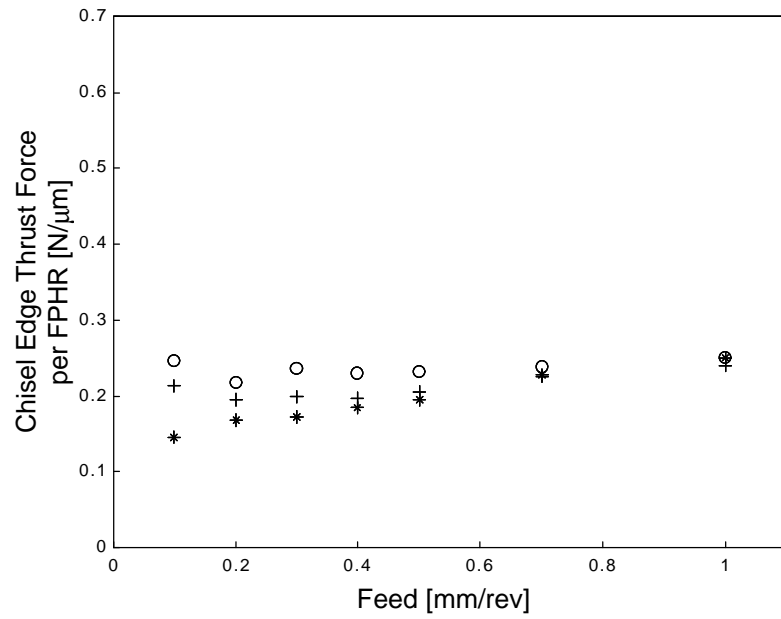
(a) Thrust Force at Chisel Edge  $F_{Chisel}$



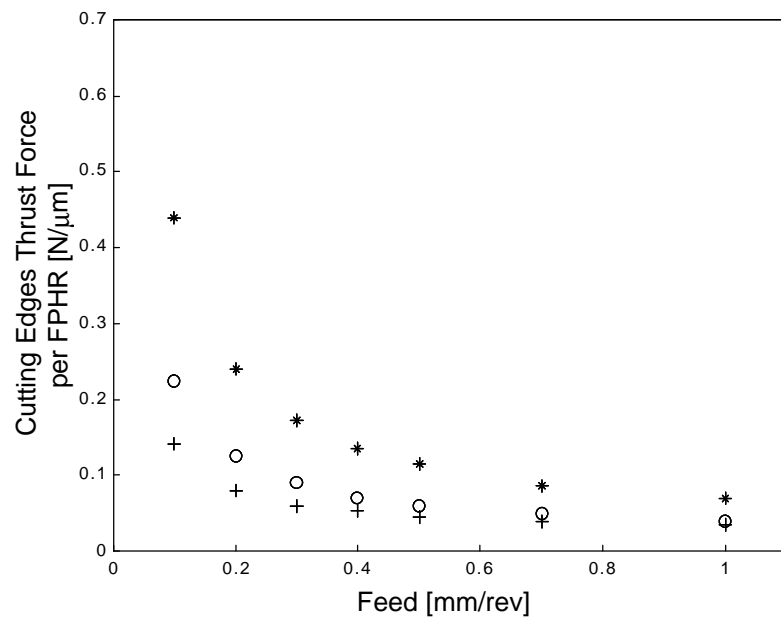
(b) Thrust Force at Cutting Edge  $F_{Cutting}$

Fig. 4.4 Thrust Force at Chisel Edge and Cutting Edges Given by Experimental Data.  
(+ : 6.35 mm dia., o : 7.94 mm dia., and \* : 9.35 mm dia.)





(a) Chisel Edge Thrust Force per FPHR  $K_{Fphr \rightarrow ForceChisel}$



(b) Cutting Edges Thrust Force per FPHR  $K_{Fphr \rightarrow ForceCutting}$

Fig. 4.5  $K_{Fphr \rightarrow ForceChisel}$  and  $K_{Fphr \rightarrow ForceCutting}$  Calculated from Experimental Data.

(+ : 6.35 mm dia., o : 7.94 mm dia., and \* : 9.35 mm dia.)

## 4.3 Discrete Hocheng-Dharan Equations and Thrust Force at PreExit Drilling

In Fig. 4.1 (c), the thrust force slope of Segment DE (the *PreExit Drilling* phase) was caused by delamination or bulging. In this section, the thrust force values for this phase will be compared with results from both the Hocheng-Dharan equations and the discrete Hocheng-Dharan equations. The latter equations will be introduced in the first subsection.

### 4.3.1 Discrete Hocheng-Dharan Equations

The values given by the original Hocheng-Dharan equations are continuous with respect to drill position; however, the thrust force that causes delamination must be discrete, since delamination occurs only between laminae, not inside a lamina.

To express this clearly, we introduce

$$F_D(n) = p \sqrt{\frac{8G_{IC} E(nh_t)^3}{3(1-n^2)}} \quad (4.3.1)$$

where  $h_t$  is the thickness of one layer. This function returns the critical thrust force at push-out delamination, where  $n$  is the number of layers that remain undrilled. If the material properties of Section 6.1 are substituted into Eq. (4.3.1), we obtain

$$F_D(n) = p \sqrt{\frac{8 \cdot 260 \cdot 41.6 \cdot 10^9 \cdot (n \cdot 0.127 \cdot 10^{-3})^3}{3 \cdot (1 - 0.3^2)}} = 25.3 \times n^{3/2} \quad (4.3.2)$$

The first eight values of this function are as follows:  $F_D(1)=25.3[\text{N}]$ ,  $F_D(2)=71.6[\text{N}]$ ,  $F_D(3)=131.5[\text{N}]$ ,  $F_D(4)=202.5[\text{N}]$ ,  $F_D(5)=283.0[\text{N}]$ ,  $F_D(6)=372.0[\text{N}]$ ,  $F_D(7)=468.8[\text{N}]$  and  $F_D(8)=572.8[\text{N}]$ .

Using the function of Eq. (4.3.1), the discrete Hocheng-Dharan equation for push-out delamination is defined as

$$F_{D,PushOut}(h) = F_D([h/h_t]) = p \sqrt{\frac{8G_{IC}E([h/h_t]h_t)^3}{3(1-n^2)}} \quad (4.3.3)$$

and the discrete Hocheng-Dharan equation for peel-up delamination is defined as

$$F_{D,PeelUp}(h) = F_D([(H-h)/h_t]) = p \sqrt{\frac{8G_{IC}E([(H-h)/h_t]h_t)^3}{3(1-n^2)}} \quad (4.3.4)$$

where the new function  $[x]$  returns the smallest integer that is greater than or equal to  $x$ . Theoretically,  $F_{D,PushOut}(h)$  and  $F_{D,PeelUp}(h)$  express the robust thrust forces for drilling without delamination, where  $h_t$  refers to the thickness of one lamina. These expressions assume that no bulging or delamination occurs inside any lamina.

Figure 4.6 shows the graph of the Hocheng-Dharan equations and the discrete Hocheng-Dharan equations, where the horizontal axis is the uncut thickness  $h$ . The drill advances leftward in the graph. The material properties used for this plot are the same as those of Section 6.1. The discrete values of  $F_D(1)=25.3[\text{N}]$ ,  $F_D(2)=71.6[\text{N}]$  and  $F_D(3)=131.5[\text{N}]$  are also shown in the same graph.

### 4.3.2 Thrust Force at PreExit Drilling

Figure 4.7, parts (a) through (d), show the experimental results for feed and thrust force in the *PreExit Drilling* phase for drilling of carbon fiber reinforced laminates. The feeds are 0.1, 0.4, 0.7 and 1.0 mm/rev, and the spindle speed is 1,000 rpm; both are held constant during each drilling. One carbide-tipped drill was used in all drilling experiments. The drill diameter is 6.35 mm and the specimen thickness is 9.78 mm. In the four graphs of Fig. 4.7, the mirror images of the DE segments (one segment per experimental run) are drawn in the lower left corner. The lower-left-hand region of Fig. 4.6 is superimposed on each part (a) ~ (d) of Fig. 4.7. In each case, the drill moves from right to left. The magnifications of the four graphs are different, although the ratios of the horizontal axis and the vertical axis are kept constant.

In the 2 ~ 6 oblique lines of Fig. 4.7, the lower left part corresponds to the linear approximation (Segment DE) of the decreasing thrust force. The approximation is made by connecting the endpoints. Point D is represented by a circle, and Point E is always located on the vertical line  $h = 0$ . The vertical axis value of the asterisk point is the average thrust force at full engagement. The real thrust force value (before the thrust force begins to decline) is, generally, on the right side of the dotted line.

There was no delamination around the holes for (a) 0.1 mm/rev and (b) 0.4 mm/rev, while delamination was observed at exit of each hole in the cases of (c) 0.7 mm/rev and (d) 1.0 mm/rev. The original Hocheng-Dharan theory can be modified to “If the line segment DE and the curve of the discrete Hocheng-Dharan equation do not cross at any point, delamination does not occur.” The modified theory is appropriate, although two DE lines in (c) are below the discrete Hocheng-Dharan equation values.

In the graphs, it is clear that the point (0.127 mm, 25.3 N) is critical, *i.e.* the last layer is the most vulnerable lamina for constant feedrate drilling. Hence, the above theory can be simplified to “If the line DE is located below the point (0.127 mm, 25.3 N), delamination does not occur.” However, we have not yet studied whether bulging can make delamination more likely by assisting the delamination process, or less likely by releasing the energy that could cause delamination. The influence of bulging on the lower laminae must also be studied in the context of delamination and drill models. Note that bulging is a nonlinear process and is not considered in the Hocheng-Dharan model, which is based on linear elastic fracture mechanics (LEFM).

In the four plots of Fig. 4.7, average thrust forces at full engagement are about 20 % higher than the thrust force of Table 4.1. The reason for this could be the wear caused by the repeated usage of the same drill for this experiment. Table 4.1 shows that the cutting edges’ thrust forces for 0.1, 0.4, 0.7 and 1.0 mm/rev are 7.1, 10.5, 13.7 and 17.5 N, respectively. All exit thrust forces in the four graphs are between –26 % and +62 % of these values in each case.

In Fig. 4.8, all four plots of Fig. 4.7 are drawn on one graph. The blank space to the right of the DE segments can be considered to indicate the region that does not cause the thrust force to decrease. This graph is used in Subsection 5.5.2 to determine the thrust force reference.

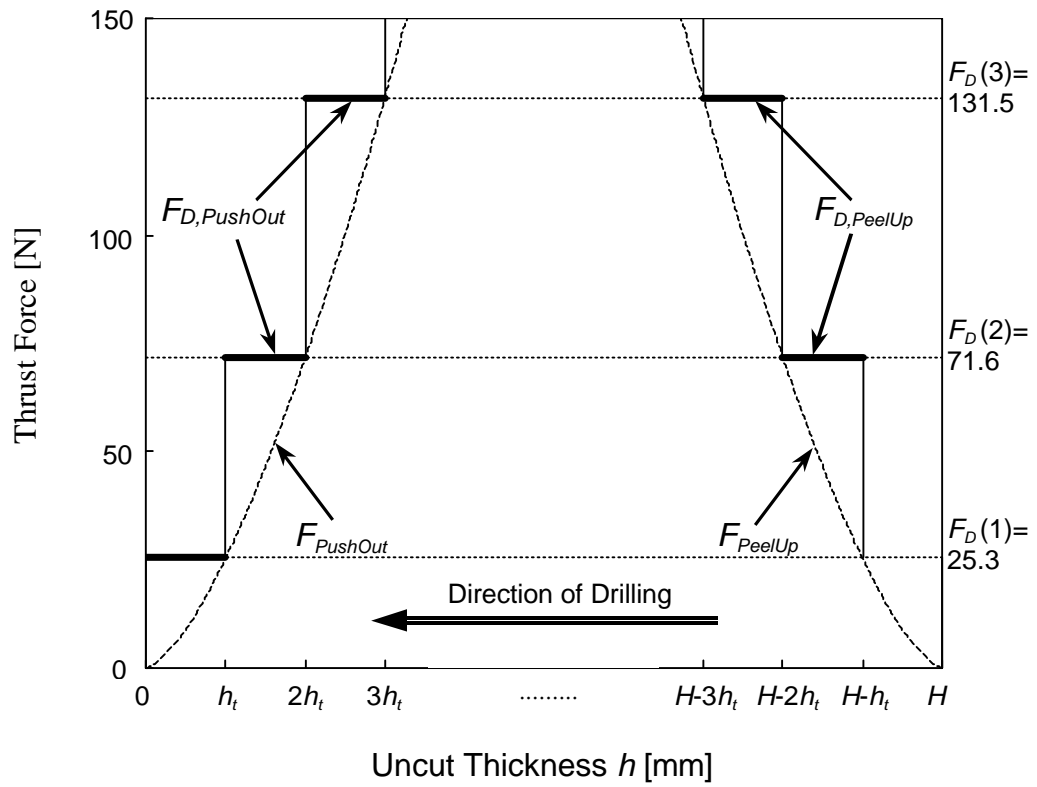
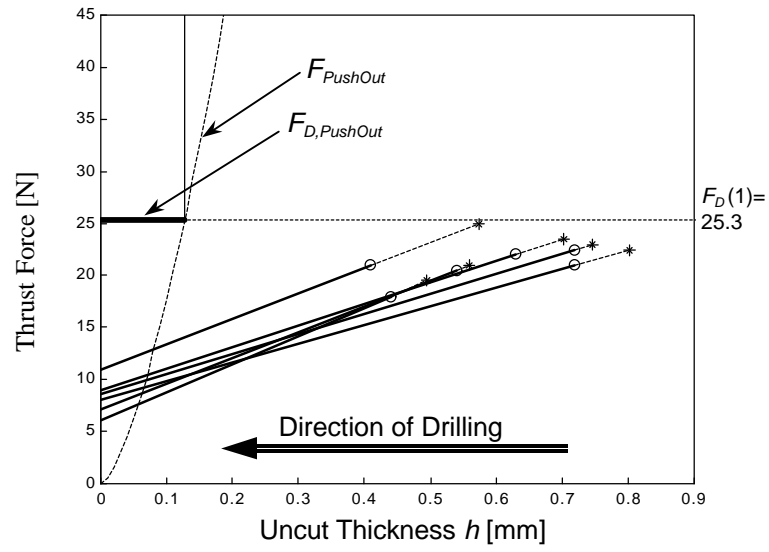
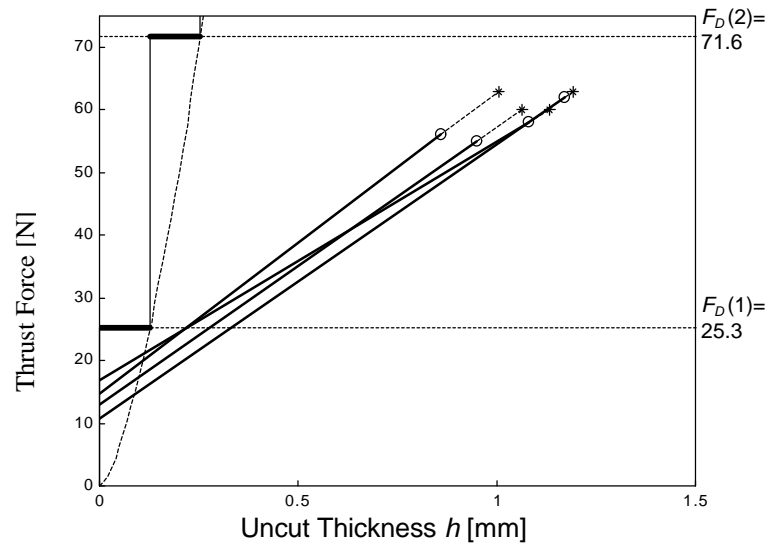


Fig. 4.6 Hocheng-Dharan Equations and Discrete Hocheng-Dharan Equations for Push-out Delamination and Peel-up Delamination. (Single-layer thickness is  $h_t = 0.127$  [mm].)



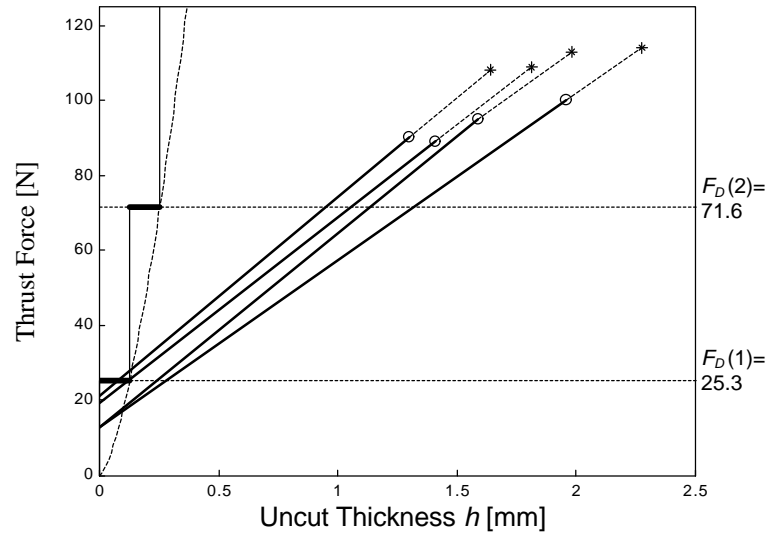
(a) Feed 0.1 mm/rev



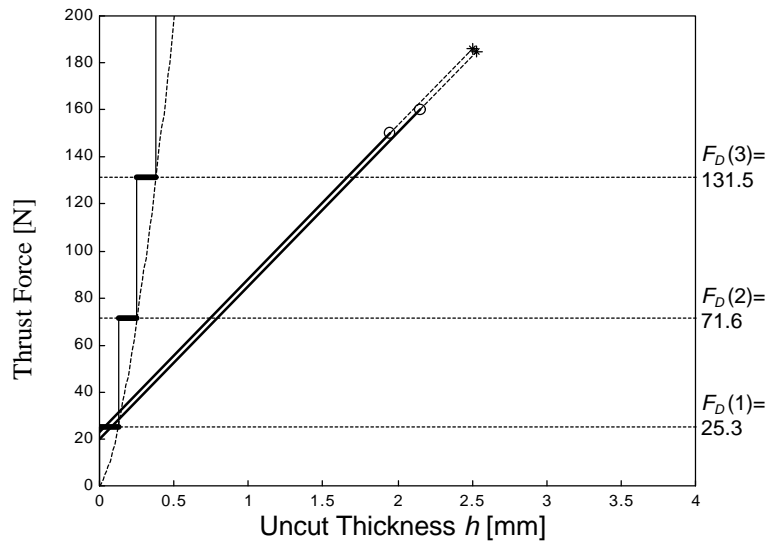
(b) Feed 0.4 mm/rev

Fig. 4.7 Uncut Thickness and Thrust Force in the *PreExit Drilling* Phase When Thrust Force Starts Decreasing. (Drill diameter is 6.35 mm. Spindle speed is 1,000 rpm, constant.)

- — : The decreasing thrust force line (mirror image of Segment DE of Fig. 4.1 (c)) approximated by a straight line connecting the endpoints.
- \* - - - : The average thrust force in full engagement (\*), and the extension of the decreasing thrust force line.



(c) Feed 0.7mm/rev



(d) Feed 1.0 mm/rev

Fig. 4.7 Uncut Thickness and Thrust Force in the *PreExit Drilling* Phase When Thrust Force Starts Decreasing. (Drill diameter is 6.35 mm. Spindle speed is 1,000 rpm, constant.)

- — : The decreasing thrust force line (mirror image of Segment DE of Fig. 4.1 (c)) approximated by a straight line connecting the endpoints.
- \* - - - : The average thrust force in full engagement (\*), and the extension of the decreasing thrust force line.



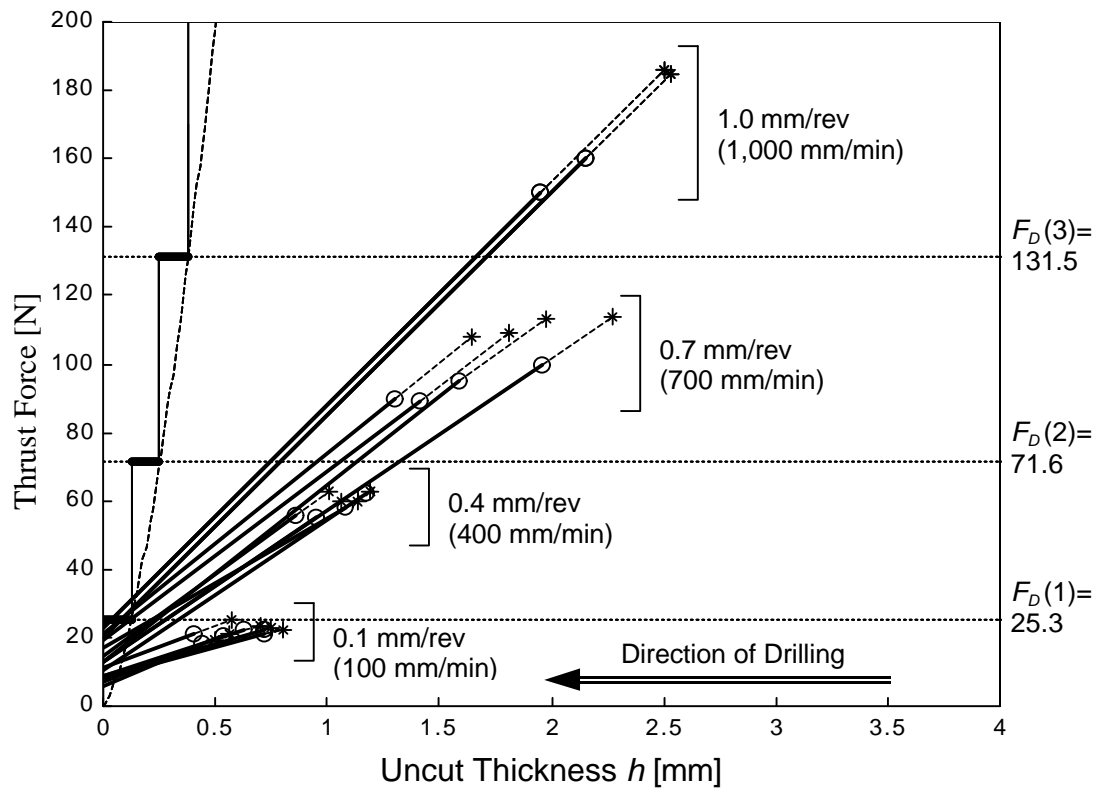


Fig. 4.8 Uncut Thickness and Thrust Force in the *PreExit Drilling* Phase When Thrust Force Starts Decreasing. (The feedrate is 0.1 mm/rev, 0.4 mm/rev, 0.7 mm/rev and 1.0mm/rev. Spindle speed is 1,000 rpm, constant. All four graphs of Fig. 4.7 are drawn on this graph.)

## 4.4 Summary

In this chapter, thrust force and torque curves as functions of drill position were characterized. The thrust force curve shows strong dependence on drill position; this characteristic is the motivation for using drill position in the supervisory control to decide the control scheme, reference force, etc. Next, the coefficients of thrust force and torque from Shaw's equations were determined using the experimental data. The new parameters, thrust force per FPHR (Feed Per Half Revolution) and torque per FPHR, were introduced, and the thrust forces at entrance and at exit were also discussed, along with the relation between Shaw's equations and the new parameters. The discrete Hocheng-Dharan equations were introduced in order to consider the thickness of laminae explicitly. The thrust force graph for the *PreExit Drilling* phase was used to compare experimental data to the results of the discrete Hocheng-Dharan equations. The relation between the thrust force curve positions and delamination was considered. A graph was created that shows the lowest limit of the uncut thickness that does not cause the thrust force to decrease.

## **CHAPTER 5**

### **Supervisory Control for Drilling Composite Materials**

#### **$\frac{3}{4}$ Controller Design $\frac{3}{4}$**

The design of supervisory control for drilling of composite materials is presented. The supervisory controller decides the control strategy, and sets the reference signal and controller gains. This chapter begins with the description of the transfer function (from voltage input to velocity) of the feed drive for the horizontal Y-axis. The designs of the position, thrust force and torque controllers for drilling are based on this transfer function. The designs of thrust force and torque controllers also require the knowledge of transfer functions of the drilling dynamics and sensor gains. Adequate sampling time and low-pass filters must be selected for a given spindle speed. In the design, it is assumed that thrust force and torque have dynamics derived from an imaginary chip thickness. Thrust force and torque cannot be controlled simultaneously; therefore they are controlled in different phases. The drilling process consists of different phases, which are determined by the position of the drill relative to the top and bottom surfaces of the workpiece. Control strategies are developed for each of the phases.

## 5.1 Transfer Functions of the Machine Tool Feed Drives

In the Matsuura experimental setup, the voltage input to the machine tool servo pack (from the DSP controller) is used as the velocity command of each of the three-axis movements. To obtain a reasonable estimate of the linear transfer function for each axis of the machining center, the velocity response of the feed drive to a set of sine-wave voltage inputs with various frequencies was recorded, and the model was obtained using the least squares method (Al-Majed, 1997). The transfer functions from voltage input  $V_i$  [V] to velocity output  $U_a$  [ $\mu\text{m}/\text{sec}$ ] of the X, Y and Z-axis were estimated as

$$G_v^x(s) = \frac{1.71 \times 10^6}{s + 55.34} \quad [(\mu\text{m}/\text{sec})/\text{V}] \quad (5.1.1)$$

$$G_v^y(s) = \frac{1.39 \times 10^6}{s + 44.61} \quad [(\mu\text{m}/\text{sec})/\text{V}] \quad (5.1.2)$$

$$G_v^z(s) = \frac{1.61 \times 10^6 e^{-0.004s}}{s + 33.74} \quad [(\mu\text{m}/\text{sec})/\text{V}] \quad (5.1.3)$$

The mechanical structures of the X-axis and the Y-axis are similar, but that of the Z-axis is more complicated because of the presence of the metallic chain and the counterweight. For this reason, as well as other reasons mentioned in Subsection 3.3.2, the Y-axis was chosen as the drilling axis. The transfer function from voltage input to feedrate is, therefore,

$$G_{\text{VoltageInput} \rightarrow \text{Feedrate}}(s) = \frac{K_y}{s + a_y} = \frac{1}{J_y s + B_y} \quad (5.1.4)$$

where

$$a_y = 44.61 \text{ [1/sec]}, \quad K_y = 1.39 \times 10^6 \text{ [(\mu m/sec)/V]} \quad (5.1.5)$$

and

$$J_y = 7.194 \times 10^{-7} \text{ [V/(\mu m/sec}^2\text{)]}, \quad B_y = 3.209 \times 10^{-5} \text{ [V/(\mu m/sec)]} \quad (5.1.6)$$

The transfer function from voltage to position is, accordingly,

$$G_{VoltageInput \rightarrow Position}(s) = \frac{1}{s(J_y s + B_y)} \quad (5.1.7)$$

The ZOH discrete-time equivalents of the transfer functions of Eq. (5.1.4) and Eq. (5.1.7)

are

$$G_{VoltageInput \rightarrow Feedrate}(z) = \frac{b_0}{z - p} \quad (5.1.8)$$

and

$$G_{VoltageInput \rightarrow Position}(z) = \frac{b_1 z + b_2}{(z - 1)(z - p)} \quad (5.1.9)$$

respectively, where  $p = \exp\left(-\frac{T_s B_y}{J_y}\right)$ ,  $b_0 = \frac{1}{B_y}(1-p)$ ,  $b_1 = \frac{1}{B_y}\left(T_s + \frac{J_y}{B_y}(p-1)\right)$  and

$$b_2 = \frac{1}{B_y}\left(\frac{J_y}{B_y}(1-p) - T_s p\right), \text{ and } T_s \text{ is the sampling time.}$$

If  $T_s$  is 5 msec, as will be determined in Section 5.3 (for the case of spindle speed 2,000 rpm), then the above introduced variables become:  $p = 0.8001$ ,  $b_0 = 6.230 \times 10^3$ ,  $b_1 = 16.15$  and  $b_2 = 15.00$ .

## 5.2 Position Control

The transfer function of the Proportional-plus-Derivative (PD) controller is given by

$$G_{PositionPD}(s) = K_c(1 + T_d s) \quad (5.2.1)$$

where  $K_c$  is the proportional gain and  $T_d$  is the derivative time constant. The discrete-time counterpart is

$$G_{PositionPD}(z) = K_p + K_d(1 - z^{-1}) = (K_p + K_d) - K_d z^{-1} = \frac{(K_p + K_d)z - K_d}{z} \quad (5.2.2)$$

where  $K_p = K_c$  and  $K_d = K_c T_d / T_s$ .

To make the closed-loop transfer function critically damped with corner frequency  $\omega$ ,  $K_p = J\omega^2$  and  $K_d = (2J\omega - B)/T_s$  are chosen. When  $\omega = 200$  rad/sec and  $T_s = 5$  msec, the two coefficients become

$$K_p = 7.19 \times 10^{-7} \times 200^2 = 2.88 \times 10^{-2} = 0.0288 \text{ [V/}\mu\text{m]} \quad (5.2.3)$$

and

$$K_d = (2 \times 7.19 \times 10^{-7} \times 200 - 3.21 \times 10^{-5}) / 0.005 = 0.0511 \text{ [V/}\mu\text{m]} \quad (5.2.4)$$

The discrete time PD controller becomes

$$G_{\text{positionPD}}(z) = \frac{0.0799z - 0.0511}{z} \quad (5.2.5)$$

### 5.3 Thrust Force Control

For turning and milling, force control is typically accomplished by adjusting the feedrate, which is proportional to the chip thickness if the spindle speed is constant. The steady state relationship linking the cutting force  $F_t$ , the uncut chip thickness  $h$ , and the depth of cut  $b$ , can be written in the form:

$$F_t = K_t b h^p = (K_t b h^{p-1}) h = r_t h \quad (5.3.1)$$

where the last coefficient  $r_t$  is treated as a time varying parameter in the linear equation form (Tomizuka, Oh and Dornfeld, 1983; Tomizuka and Zhang, 1988).

In this section, it is assumed that the same form can also be applied to the thrust force of the drilling process. The geometric relation between the drill edges and the chip, however, is not as obvious as in the cases of turning and milling. Furthermore, the mechanism of the chisel edge (especially at the center) is like extrusion rather than cutting, which makes the dynamics of drilling quite different from that of turning or milling.

The above-mentioned assumption causes few problems at steady state. Of greater concern is the fact that the dynamics of the model may be different from the actual dynamics. Nevertheless, we utilize the model of Eq. (5.3.1), since it is intuitively understandable and lends itself easily toward a consistent controller design for this model.

### 5.3.1 Modeling of Thrust Force During Drilling

If a normal two-flute drill is used, *i.e.* one with two sets of edges symmetric with respect to the drill axis (here, it is assumed that the chisel edge consists of two edges separated by the center point), then the following linear equation can be obtained;

$$F = K_{F_{phr} \rightarrow Force} \cdot f_{phr} \quad (5.3.2)$$

where  $F$  is the thrust force,  $K_{F_{phr} \rightarrow Force}$  is a time varying parameter corresponding to  $r_t$  of Eq. (5.3.1), and  $f_{phr}$  is the Feed Per Half Revolution (FPHR), which corresponds to the chip thickness  $h$  in Eq. (5.3.1). The definition of FPHR is “the distance the drill has advanced during its last half revolution.” It is not necessarily the same as one half of feed, nor the feedrate multiplied by one half of the period of the spindle revolution at any given



moment. Equation (5.3.2) and the definition suggest the following dynamic model of thrust force: *i.e.* given a step change in the actual feedrate, the thrust force achieves a ramp profile leveling out at a new constant value in one half revolution.

If the spindle speed is constant, the Laplace transform of the distance  $f_{phr}$  [ $\mu\text{m}$ ] can be expressed as

$$f_{phr}(s) = \frac{1}{s} U_a(s) - \frac{e^{-T_{HR}s}}{s} U_a(s) \quad (5.3.3)$$

where  $U_a$  [ $\mu\text{m}/\text{sec}$ ] is the actual feedrate, and  $T_{HR}$  [sec] is the time interval for one half revolution of the drill. Therefore, the transfer function relating feedrate  $U_a(s)$  to feed per one half revolution  $f_{phr}(s)$  is expressed as

$$G_{Feedrate \rightarrow Fphr}(s) = \frac{1 - e^{-T_{HR}s}}{s} \quad (5.3.4)$$

Let the unit of the gain factor from FPHR to thrust force,  $K_{Fphr \rightarrow Force}$ , be in [ $\text{N}/\mu\text{m}$ ], then the following relation between feedrate in [ $\mu\text{m}/\text{sec}$ ] and thrust force in [ $\text{N}$ ] is obtained;

$$G_{Feedrate \rightarrow Force}(s) = K_{Fphr \rightarrow Force} \frac{1 - e^{-T_{HR}s}}{s} \quad (5.3.5)$$

In our experimental setup, the force output of the dynamometer, Kistler 9271A, is the input to a charge amplifier, Kistler 5004. The amplifier gain mode chosen for our experiments is 50 N/V, and the transfer function from thrust force to voltage output is

$$K_{ForceSensor} = 0.02 \text{ [V/N]} \quad (5.3.6)$$

The stage dynamics obtained in Section 5.1 is

$$G_{VoltageInput \rightarrow Feedrate}(s) = \frac{K_y}{s + a_y} \quad (5.3.7)$$

and the transfer function of the low-pass filter attached at the output of the charge amplifier is

$$G_{LPF}(s) = \frac{b_{LPF}}{s + b_{LPF}} \quad (5.3.8)$$

where  $b_{LPF}$  is set larger than  $a_y$ .

The transfer function from voltage input (corresponding to command feedrate) to voltage output (corresponding to thrust force) is, therefore, expressed as

$$G_{VoltageInput \rightarrow VoltageForce}(s) = K_{ForceSensor} K_{Fphr \rightarrow Force} \cdot \frac{K_y}{s + a_y} \cdot \frac{1 - e^{-T_{HR}s}}{s} \cdot \frac{b_{LPF}}{s + b_{LPF}} \quad (5.3.9)$$

The continuous time model  $G_{VoltageInput \rightarrow VoltageForce}(s)$  is the plant that will be controlled by our digital controller (via interfaces to analog signals).

The analog-to-digital converter that receives the analog thrust force signal is a 12-bit converter with input range of  $\pm 10$  V, and the conversion gain from analog voltage to digital value is

$$K_{A/D} = 2048/10 = 204.8 \text{ [1/V]} \quad (5.3.10)$$

The value of  $K_{ForceSensor}$  in Eq. (5.3.6) was chosen by considering the balance of both the maximum thrust force,  $10/K_{ForceSensor} = 500$  N ( = 51 kgf ), and the thrust force resolution,  $1/(K_{A/D} \cdot K_{ForceSensor}) = 0.244$  N ( = 24.9 gf ).

To design a controller for the DSP in discrete time with a sampling time  $T_s$ , the ZOH equivalent of the transfer function (5.3.9) multiplied by  $K_{A/D}$  is obtained:

$$G_{VoltageInput \rightarrow DigitalForce}(z^{-1}) = K_{A/D} \cdot (1 - z^{-1}) \cdot Z \left\{ L^{-1} \left( \frac{K_{ForceSensor} K_{Fphr \rightarrow Force} K_y (1 - e^{-T_{HR}s}) b_{LPF}}{s^2 (s + a_y)(s + b_{LPF})} \right) \right\} \quad (5.3.11)$$

where the gain of the digital-to-analog converter has been assumed to be unity and the plant input is in volts. Figure 5.1 represents the block diagram of the system from the (discrete) voltage input to the measured digital thrust force.

If the half revolution interval  $T_{HR}$  is expressed as  $N_{HR} \cdot T_s$  ( $N_{HR}$  is a constant integer) and  $K_{Fphr \rightarrow Force}$  is regarded as constant, we obtain the following equation ( $a_y$  and  $b_{LPF}$  are written simply as  $a$  and  $b$ , respectively),

$$\begin{aligned}
& G_{\text{VoltageInput} \rightarrow \text{DigitalForce}}(z^{-1}) \\
&= K_{A/D} K_{\text{ForceSensor}} K_{\text{Fphr} \rightarrow \text{Force}} K_y b(1-z^{-1})(1-z^{-N_{HR}}) \cdot \mathcal{Z} \left\{ L^{-1} \left( \frac{1}{s^2(s+a)(s+b)} \right) \right\} \\
&= \frac{K_{A/D} K_{\text{ForceSensor}} K_{\text{Fphr} \rightarrow \text{Force}} K_y b(1-z^{-1})(1-z^{N_{HR}})(c_0 z^{-3} + c_1 z^{-2} + c_2 z^{-1})}{a^2 b^2 (b-a)(1-z^{-1})^2 (1-e^{-aT} z^{-1})(1-e^{-bT} z^{-1})} \\
&= \frac{K_{A/D} K_{\text{ForceSensor}} K_{\text{Fphr} \rightarrow \text{Force}} K_y b}{a^2 b^2 (b-a)} (1+z^{-1}+z^{-2}+\dots+z^{-(N_{HR}-1)}) \frac{c_0 z^{-3} + c_1 z^{-2} + c_2 z^{-1}}{(1-e^{-aT} z^{-1})(1-e^{-bT} z^{-1})} \\
&= \frac{K_{A/D} K_{\text{ForceSensor}} K_{\text{Fphr} \rightarrow \text{Force}} K_y b}{a^2 b^2 (b-a)} (z^{-1} + z^{-2} + z^{-3} \dots + z^{-N_{HR}}) \frac{c_0 z^{-2} + c_1 z^{-1} + c_2}{(1-e^{-aT} z^{-1})(1-e^{-bT} z^{-1})} \quad (5.3.12)
\end{aligned}$$

or, as a function of  $z$ ,

$$\begin{aligned}
& G_{\text{VoltageInput} \rightarrow \text{DigitalForce}}(z) \\
&= \frac{K_{A/D} K_{\text{ForceSensor}} K_{\text{Fphr} \rightarrow \text{Force}} K_y b}{a^2 b^2 (b-a)} \cdot \frac{z^{N_{HR}-1} + \dots + z + 1}{z^{N_{HR}}} \cdot \frac{c_2 z^2 + c_1 z + c_0}{(z-e^{-aT})(z-e^{-bT})} \quad (5.3.13)
\end{aligned}$$

where the coefficients,  $c_2$ ,  $c_1$  and  $c_0$ , are

$$\begin{aligned}
c_2 &= -(a-b) \{ abT + (a+b)(e^{-aT} + e^{-bT} - 1) \} + (a^2 e^{-aT} - b^2 e^{-bT}) \\
c_1 &= -(a-b) \{ (a+b)(1 - e^{-aT} e^{-bT}) - (a+b+abT)(e^{-aT} + e^{-bT}) \} - 2(a^2 e^{-aT} - b^2 e^{-bT}) \\
c_0 &= -(a-b)(abT + a+b)e^{-aT} e^{-bT} + (a^2 e^{-aT} - b^2 e^{-bT}) \quad (5.3.14)
\end{aligned}$$

Extending Eq. (5.3.13) to the case where  $T_{HR}$  is not an integer multiple of  $T_s$  but is still constant, *i.e.*  $(N_{HR}+\epsilon) \cdot T_s$ , the following approximate transfer function is obtained,

$$\begin{aligned}
G_{VoltageInput \rightarrow DigitalForce}(z) &= \frac{K_{A/D} K_{ForceSensor} K_{Fphr \rightarrow Force} K_y b}{a^2 b^2 (b-a)} \cdot \frac{z^{N_{HR}-1} + \dots + z + (1+\epsilon)}{z^{N_{HR}}} \cdot \frac{c_2 z^2 + c_1 z + c_0}{(z - e^{-aT})(z - e^{-bT})} \\
&= K_{ForceCE} \cdot G_{ForceTF}^o(z)
\end{aligned} \tag{5.3.15}$$

where

$$K_{ForceCE} = K_{A/D} K_{ForceSensor} K_{Fphr \rightarrow Force} K_y b \tag{5.3.16}$$

and

$$G_{ForceTF}^o(z) = \frac{1}{a^2 b^2 (b-a)} \cdot \frac{z^{N_{HR}-1} + \dots + z + (1+\epsilon)}{z^{N_{HR}}} \cdot \frac{c_2 z^2 + c_1 z + c_0}{(z - e^{-aT})(z - e^{-bT})} \tag{5.3.17}$$

The continuous-time transfer function for the same input and output, with polynomials in the numerator and denominator, is calculated by applying a Pade approximation:

$$e^{-as} \approx \frac{s^2 - (6/a)s + (12/a^2)}{s^2 + (6/a)s + (12/a^2)} \tag{5.3.18}$$

to both the ZOH and the FPHR dynamics. We obtain

$$\begin{aligned}
& G_{VoltageInput \rightarrow DigitalForce}^{Approx}(s) \\
&= K_{ForceCE} \cdot \frac{1}{T_s} \cdot \frac{(12/T_s)}{s^2 + (6/T_s)s + (12/T_s^2)} \cdot \frac{(12/T_{HR})}{s^2 + (6/T_{HR})s + (12/T_{HR}^2)} \cdot \frac{1}{(s+a)(s+b)} \\
&= K_{ForceCE} \cdot G_{ForceTF}^{o, Approx}(s)
\end{aligned} \tag{5.3.19}$$

where

$$G_{ForceTF}^{o, Approx}(s) = \frac{1}{T_s} \cdot \frac{(12/T_s)}{s^2 + (6/T_s)s + (12/T_s^2)} \cdot \frac{(12/T_{HR})}{s^2 + (6/T_{HR})s + (12/T_{HR}^2)} \cdot \frac{1}{(s+a)(s+b)} \tag{5.3.20}$$

In the above calculation,  $\frac{1}{T_s}$  is used as a multiplying factor in order to adjust the steady state gain of ZOH to be unity. The dominant pole of Eq. (5.3.19) is  $-a$  ( $= -44.61$ ) if the spindle speed is faster than about 400 rpm; this condition is always satisfied in our experiments.

Figure 5.2 shows the Bode plots of the discrete time model  $G_{ForceTF}^o(z)$  of Eq. (5.3.17) with the sampling time of  $T_s$ , and the approximate continuous model  $G_{ForceTF}^{o, Approx}(s)$  of Eq. (5.3.20), both for

- (a)  $e = 0.0$  i.e.  $T_{HR} = N_{HR} \cdot T_s$ , 2,000 rpm
- (b)  $e = +0.5$  i.e.  $T_{HR} = (N_{HR} + 0.5) \cdot T_s$ , 1,714 rpm
- (c)  $e = +1.0$  i.e.  $T_{HR} = (N_{HR} + 1.0) \cdot T_s$ , 1,500 rpm
- (d)  $e = -0.5$  i.e.  $T_{HR} = (N_{HR} - 0.5) \cdot T_s$ , 2,400 rpm

(e)  $e = -1.0$  i.e.  $T_{HR} = (N_{HR} - 1.0) \cdot T_s$ , 3,000 rpm

where  $N_{HR}=3$  and  $T_s=0.005$ . The other values are the same as those in the example introduced in the next subsection; this condition will be named Condition A. In the figure, the discrete models with  $N_{HR} = 4$  are also shown in (b) and (c), and the discrete model with  $N_{HR} = 2$  is shown in (e). In (c), the discrete model of  $N_{HR} = 4$  with  $e = 0.0$  (not the models of  $N_{HR} = 3$  with  $e = +1.0$ ) is mathematically exact. In the case of (e), the model of  $N_{HR} = 3$  with  $e = -1.0$ , and the model of  $N_{HR} = 2$  with  $e = 0$  are identical.

Figure 5.2 (a), (b) and (d) show that the matching between the two types of models (discrete model of Eq. (5.3.17) and approximate continuous model of Eq. (5.3.20), not the two discrete models with different  $N_{HR}$ ) is excellent. This is true not only for the case of  $e = 0$ , but also for the cases of  $e = +0.5$  and  $e = -0.5$ . The extension from Eq. (5.3.13) to Eq. (5.3.15) has, therefore, been justified. Figure 5.2 (c) shows that the two types of models at 1,500 rpm are slightly different. The two types of models are in good agreement at 3,000 rpm (Fig. 5.2 (e)).

Figure 5.3 shows the open loop unit step responses of the discrete time model  $G_{ForceTF}^o(z)$  of  $N_{HR} = 3$  for various values of  $e$ . For comparison, the models of  $N_{HR} = 4$  with  $e = -0.5$  and  $e = 0.0$  are also shown by dotted lines. The difference between the model of  $N_{HR} = 3$  with  $e = +1.0$ , and the more accurate model  $N_{HR} = 4$  with  $e = 0.0$ , is small. The difference between the model of  $N_{HR} = 3$  with  $e = +0.5$ , and the model of  $N_{HR} = 4$  with  $e = -0.5$ , is negligible.

As a result, there are few problems in applying the discrete time model  $G_{ForceTF}^o(z)$  ( $N_{HR} = 3$ , and  $e = 0.0$  at 2,000 rpm) in the spindle speed range between 1,500 rpm

( $e = +1.0$ ) and 3,000 rpm ( $e = -1.0$ ). If the spindle speed is limited to below 2,000 rpm,  $N_{HR} = 4$  can be used for better accuracy, or a smaller sampling frequency may be chosen.



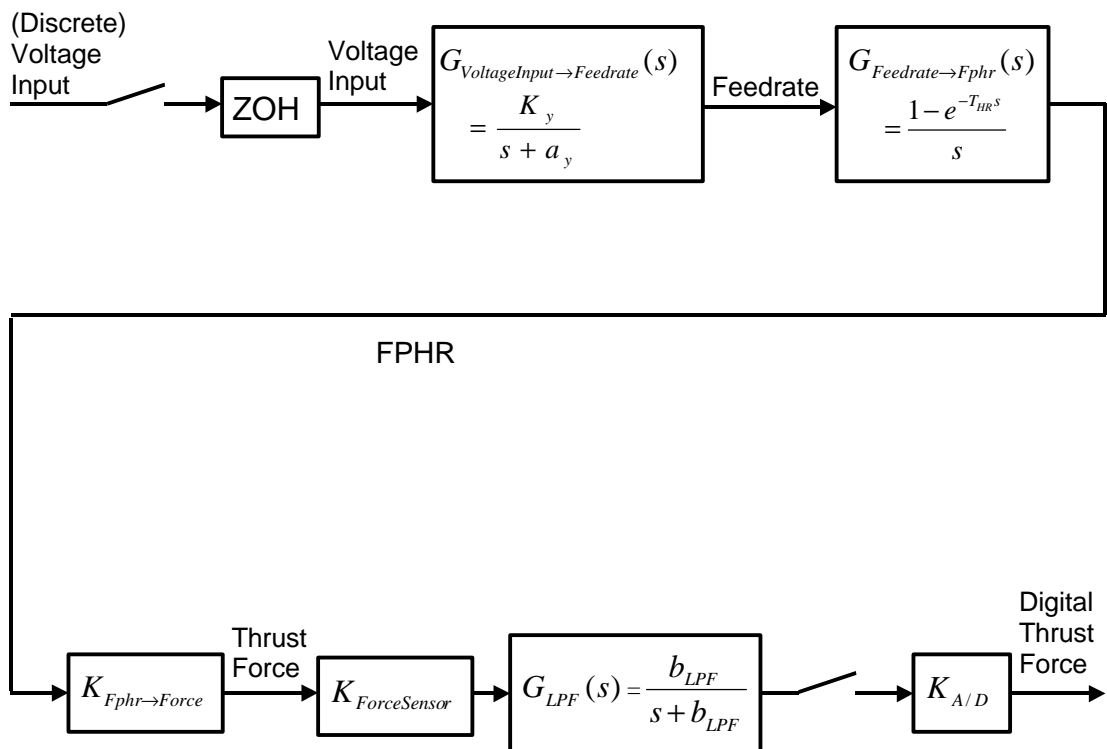
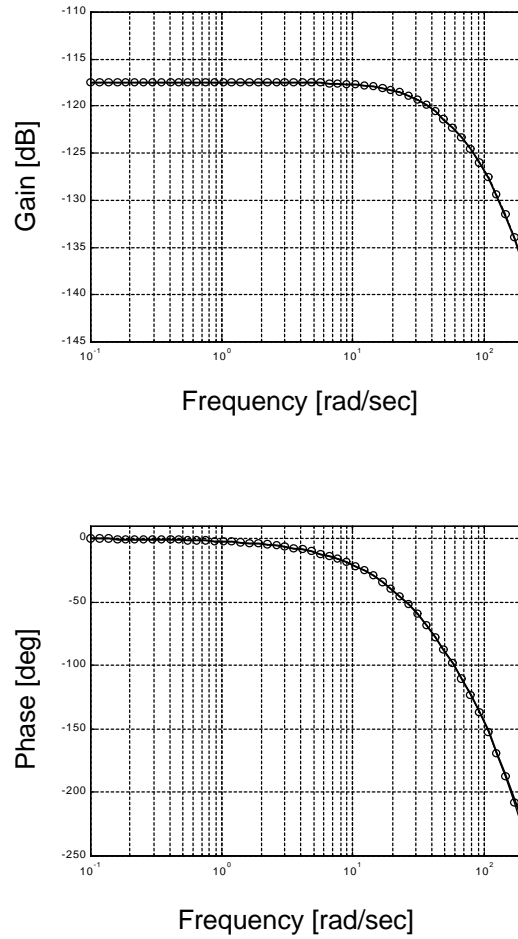
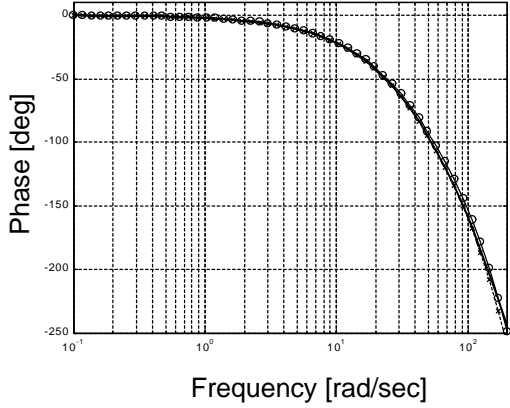
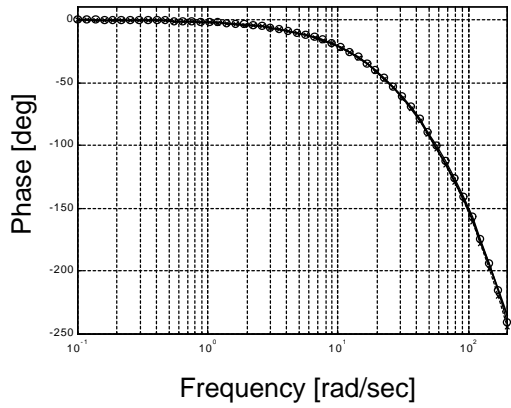
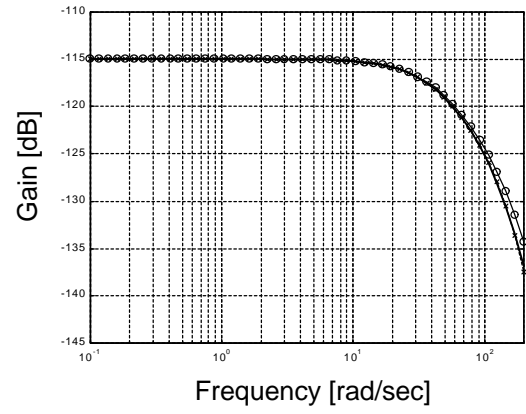
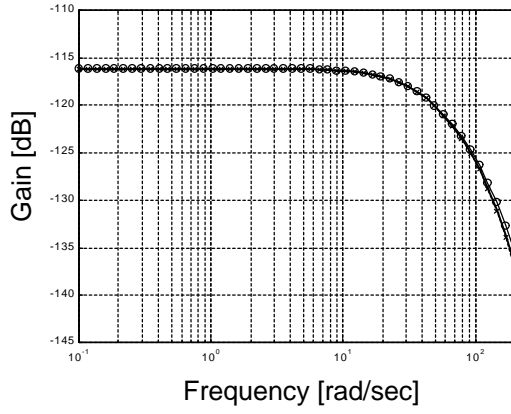


Fig. 5.1 Block Diagram of the Sampled System from the Discrete Voltage Input to the Measured Digital Thrust Force. (The overall transfer function corresponds to  $G_{VoltageInput \rightarrow DigitalForce}(z)$  in Fig. 5.4.)



(a)  $N_{HR} = 3$ ,  $e = 0$  (2,000 rpm)

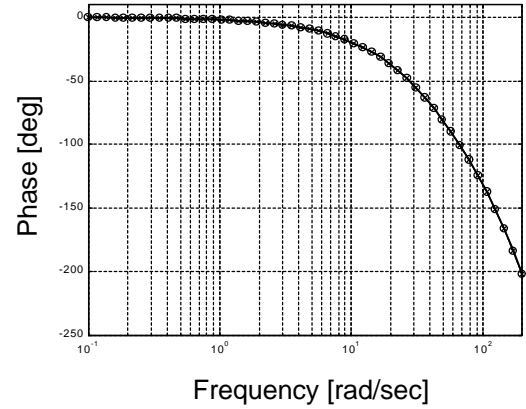
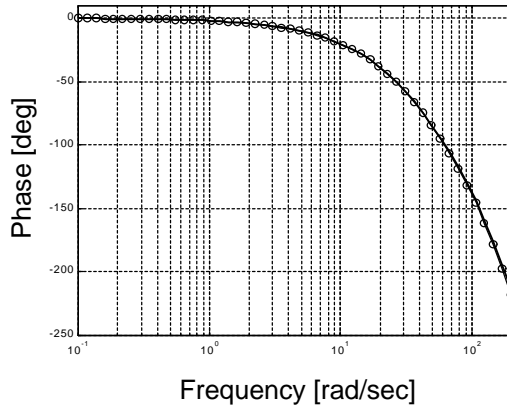
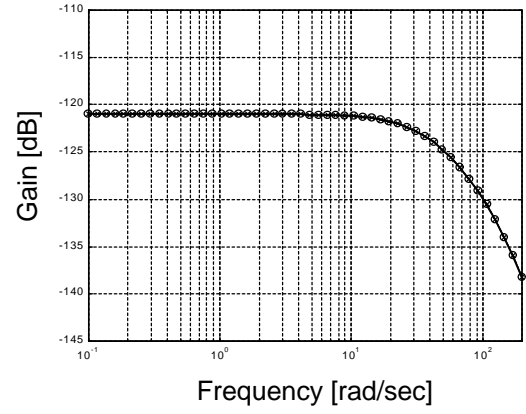
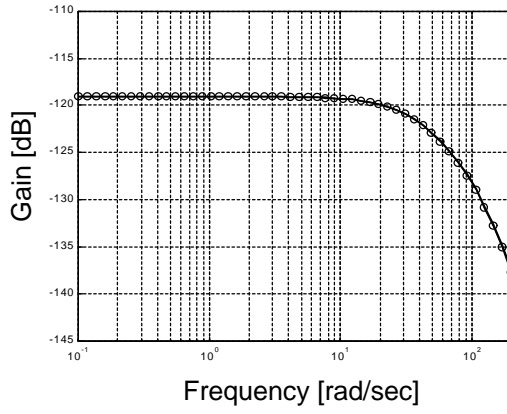
Fig. 5.2 Bode Plots of Discrete Models of  $N_{HR} = 3$  with (a)  $e = 0$  (b)  $e = +0.5$ , (c)  $e = +1.0$ , (d)  $e = -0.5$  and (e)  $e = -1.0$ , and Approximate Continuous Thrust Force Models. (In each figure, the discrete model is represented by a thin line with circles (  $-\bigcirc-\bigcirc-\bigcirc-$  ), and the approximate continuous model is represented by a thick line. Thin dotted lines with crosses (  $-\times-\times-\times-$  ) represent the discrete models with  $N_{HR} = 4$  in (b) and (c), and the discrete model with  $N_{HR} = 2$  in (e).)



(b)  $N_{HR} = 3$ ,  $e = +0.5$  (1,714 rpm)

(c)  $N_{HR} = 3$ ,  $e = +1.0$  (1,500 rpm)

Fig. 5.2 Bode Plots of Discrete Models of  $N_{HR} = 3$  with (a)  $e = 0$  (b)  $e = +0.5$ , (c)  $e = +1.0$ , (d)  $e = -0.5$  and (e)  $e = -1.0$ , and Approximate Continuous Thrust Force Models. (In each figure, the discrete model is represented by a thin line with circles (  $-\bigcirc-\bigcirc-\bigcirc-$  ), and the approximate continuous model is represented by a thick line. Thin dotted lines with crosses (  $-\times-\times-\times-$  ) represent the discrete models with  $N_{HR} = 4$  in (b) and (c), and the discrete model with  $N_{HR} = 2$  in (e).)



(d)  $N_{HR} = 3$ ,  $e = -0.5$  (2,400 rpm)

(e)  $N_{HR} = 3$ ,  $e = -1.0$  (3,000 rpm)

Fig. 5.2 Bode Plots of Discrete Models of  $N_{HR} = 3$  with (a)  $e = 0$  (b)  $e = +0.5$ , (c)  $e = +1.0$ , (d)  $e = -0.5$  and (e)  $e = -1.0$ , and Approximate Continuous Thrust Force Models. (In each figure, the discrete model is represented by a thin line with circles (  $-\bigcirc-\bigcirc-\bigcirc-$  ), and the approximate continuous model is represented by a thick line. Thin dotted lines with crosses (  $-\times-\times-\times-$  ) represent the discrete models with  $N_{HR} = 4$  in (b) and (c), and the discrete model with  $N_{HR} = 2$  in (e).)

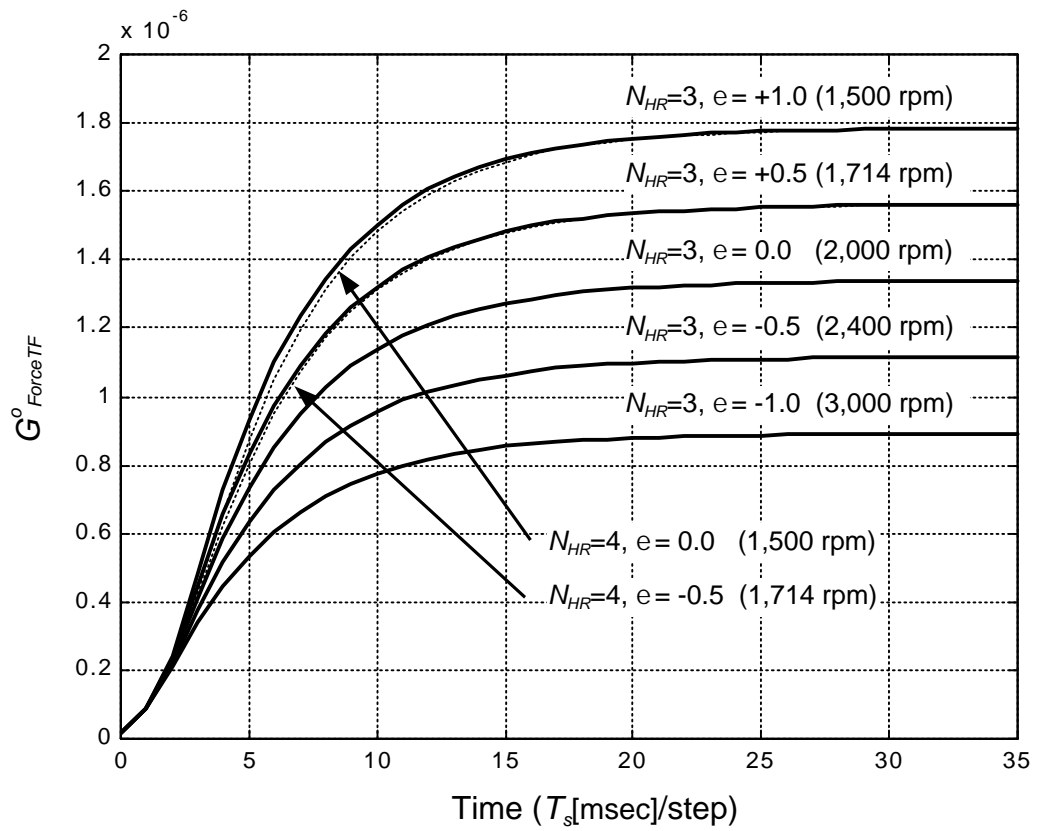


Fig. 5.3 Simulation Result of the Unit Step Responses of the Discrete Thrust Force Models of  $G^o_{ForceTF}(z)$ . (The solid lines represent the models of  $N_{HR} = 3$  with  $e = -1.0$ ,  $e = -0.5$ ,  $e = 0.0$ ,  $e = +0.5$  and  $e = +1.0$ . The dotted lines represent the models of  $N_{HR} = 4$  with  $e = -0.5$  and  $e = 0.0$ .)

### 5.3.2 Spindle Speed, Sampling Frequency and Low-pass Filter Cut-off Frequency

A sufficiently fast sampling frequency not only improves the quality of the discrete time model, but also makes it easier for the supervisory controller to detect any signals that may indicate abnormal operations or accidents such as drill breakage. The controller output does not have to be updated every sampling instance, but it is important to know the minimum sampling frequency that will satisfy the control requirements.

The low-pass filter introduced in the previous subsection prevents aliasing due to sampling and eliminates high frequency noise. When the sampling frequency is determined, the spindle speed and the cut-off frequency of the low-pass filter must also be considered. From the viewpoint of machining, the spindle speed is the only factor that directly affects the drilling process. Therefore, the sampling frequency  $\omega_s (=2\pi/T_s)$  and the cut-off frequency  $\omega_{LPF} (=b_{LPF})$  of the low-pass filter for a given spindle speed  $\omega_{Spindle}$  are considered in this subsection.

First, the closed-loop bandwidth  $\omega_b$  is estimated. In our research, any thrust force controls with frequency higher than the spindle rotation  $\omega_{Spindle}$ , are not considered. Thus, any frequency between  $\frac{1}{3}\omega_{Spindle}$  and  $\omega_{Spindle}$  is reasonable for  $\omega_b$ .

In a conservative approach, the sampling frequency  $\omega_s$  would be chosen 5 ~ 10 times as high as  $\omega_{LPF}$ , and  $\omega_{LPF}$  would be at least four times  $\omega_b$  (Anderson and Moore, 1990). The latter condition can be weakened if the low-pass filter is taken into account when the controller is designed. In the design of discrete-time controllers for drilling, it is convenient to express  $\omega_s$  as

$$\omega_s = 2N_{HR} \cdot \omega_{Spindle} \quad (5.3.22)$$

where the integer  $N_{HR}$  is the number of samples during a half rotation of the spindle.

With these considerations,

$$\omega_s = 6\omega_{Spindle} \quad (5.3.23)$$

and

$$\omega_{LPF} = 1.2\omega_{Spindle} \quad (5.3.24)$$

were determined, where the first equation implies that  $N_{HR}$  is 3. For example, if the spindle speed is 2,000 rpm (*i.e.*  $\omega_{Spindle} = 2\pi \cdot 33.3 = 209$  rad/sec and  $T_{HR} = 15$  msec), then  $\omega_s = 2\pi \cdot 200 = 1,257$  rad/sec, *i.e.*  $T_s = 5$  msec, and  $\omega_{LPF} = b_{LPF} = 2\pi \cdot 40 = 251$  rad/sec. This condition ( $\omega_{Spindle} = 209$  rad/sec,  $\omega_s = 1,257$  rad/sec, and  $\omega_{LPF} = 251$  rad/sec) is called Condition A hereafter.

When the sampling frequency  $\omega_s$  is fixed, and the actual spindle speed  $\omega_{Spindle}^{actual}$  differs from the value  $\omega_{Spindle} = \omega_s / (2N_{HR})$ , the general discrete time model of Eq. (5.3.15) in the previous subsection is valid for the following spindle frequency range:

$$\frac{\omega_s}{2(N_{HR} + 1.0)} = \frac{\omega_{Spindle} N_{HR}}{N_{HR} + 1.0} \leq \omega_{Spindle}^{actual} \leq \frac{\omega_s}{2(N_{HR} - 1.0)} = \frac{\omega_{Spindle} N_{HR}}{N_{HR} - 1.0} \quad (5.3.25)$$

and in this case,  $e$  (as a function of  $w_{Spindle}^{actual}$ ) in the discrete time model can be expressed as

$$e = N_{HR} \left( \frac{w_{Spindle}}{w_{Spindle}^{actual}} - 1 \right) \quad (5.3.26)$$

For the fixed sampling frequency  $w_s$ , if  $N_{HR}$  is 3 (as determined in Eq. (5.3.23)), Eq.

(5.3.25) for  $w_{Spindle(N_{HR}=3)} = \frac{1}{6}w_s$  becomes

$$\frac{1}{8}w_s = \frac{3}{4}w_{Spindle(N_{HR}=3)} \leq w_{Spindle}^{actual} \leq \frac{1}{4}w_s = \frac{3}{2}w_{Spindle(N_{HR}=3)} \quad (5.3.27)$$

and if  $N_{HR} = 4$  instead of 3, then Eq. (5.3.25) for  $w_{Spindle(N_{HR}=4)} = \frac{1}{8}w_s$  becomes

$$\frac{1}{10}w_s = \frac{4}{5}w_{Spindle(N_{HR}=4)} \leq w_{Spindle}^{actual} \leq \frac{1}{6}w_s = \frac{4}{3}w_{Spindle(N_{HR}=4)} \quad (5.3.28)$$

The previous subsection demonstrated the following: the discrete model with  $N_{HR} = 3$  can be used with small errors in the range of Eq. (5.3.27) (between 1,500 rpm and 3,000 rpm for Condition A). The discrete model with  $N_{HR} = 4$  gives a better approximation if the spindle speed belongs to the range of Eq. (5.3.28) (between 1,200 rpm and 2,000 rpm for



Condition A). The difference between the two models ( $N_{HR} = 3$  and  $N_{HR} = 4$ ) is small at  $\frac{1}{8}\omega_s$  (1,500 rpm) and negligible at  $\frac{1}{7}\omega_s$  (1,714 rpm).

The foregoing analysis can be appropriate for different values of  $\omega_s$ . However, if the dynamics of the stage or the target spindle speed differ significantly from this example, the influence of the change in the spindle speed must be studied for each case, and an adequate low-pass filter and sampling time must be chosen.

### 5.3.3 Design of Thrust Force Controller

The plant introduced in Subsection 5.3.1 includes no free integrator. Therefore, an integral action should be added to the feedback controller to ensure zero offset at constant thrust force. If a PI controller is chosen to be the thrust force controller, its continuous-time transfer function is given by

$$G_{ForcePI}(s) = K_c \left(1 + \frac{1}{T_i s}\right) = K_c + \frac{K_c}{T_i s} \quad (5.3.29)$$

where  $K_c$  is the proportional gain and  $T_i$  is the integral time constant. The discrete-time counterpart is

$$G_{ForcePI}(z) = K_p + K_i \frac{z^{-1}}{1 - z^{-1}} = K_p + K_i \frac{1}{z - 1} = \frac{K_p z - (K_p - K_i)}{z - 1} = K_p \frac{z - (1 - K_i / K_p)}{z - 1} \quad (5.3.30)$$

where  $K_p = K_c$  and  $K_i = K_c T_s / T_i$ , which imply  $K_i / K_p = T_s / T_i$ .

First, a PI controller  $G_{ForcePI}^o(z)$  for the plant  $G_{ForceTF}^o(z)$  of Eq. (5.3.17) (with  $e=0$ ) is designed. In the case of Condition A of Subsection 5.3.2, *i.e.*  $\omega_{spindle} = 209$  rad/sec,  $\omega_s = 1,257$  rad/sec and  $\omega_{LPF} = 251$  rad/sec, the plant  $G_{ForceTF}^o(z)$  becomes

$$\begin{aligned} G_{ForceTF}^o(z) &= \frac{1}{2.594 \times 10^{10}} \cdot \frac{z^2 + z + 1}{z^3} \cdot \frac{383.0z^2 + 1089z + 183.4}{(z - 0.8001)(z - 0.2848)} \\ &= \frac{1.476 \times 10^{-8} \cdot (z^2 + z + 1)(z + 0.1801)(z + 2.659)}{z^3(z - 0.8001)(z - 0.2848)} \end{aligned} \quad (5.3.31)$$

where  $e=0$  is satisfied because there are exactly six samplings during one spindle rotation.

The PI controller can be expressed with a proportional gain  $K_c^o$  and an integral time constant  $T_i^o$ ;

$$G_{ForcePI}^o(z) = K_c^o \frac{z - (1 - T_s/T_i^o)}{z - 1} \quad (5.3.32)$$

Since  $-a$  ( $= -44.61$ ) is a dominant pole,  $T_i^o$  is chosen to be larger than  $1/a$  ( $= 0.02242$ ); however, it must be less than the time interval for a few revolutions of the drill (one revolution takes 0.03 sec for a spindle speed of 2,000 rpm). By trial and error simulation in this range, to satisfy the conditions of short rising time and no overshoot,

$$T_i^o = 0.0280 \quad (5.3.33)$$

and

$$K_c^o = 6.49 \times 10^5 \quad (5.3.34)$$

were chosen. With these values, the controller becomes

$$G_{ForcePI}^o(z) = K_c^o \frac{z - (1 - T_s / T_i^o)}{z - 1} = 6.49 \times 10^5 \cdot \frac{z - 0.821}{z - 1} \quad (5.3.35)$$

The complete block diagram of the closed loop system (with  $G_{VoltageInput \rightarrow DigitalForce}(z)$  as the plant and  $G_{ForcePI}(z)$  as the PI controller) is shown in Fig. 5.4.

Figure 5.5 shows the root locus of  $K \cdot G_{ForcePI}^o(z) \cdot G_{ForceTF}^o(z)$  where the controller of Eq. (5.3.35) corresponds to  $K=1$ . The system has a stability limit at  $K=4.3$ , *i.e.*, when the proportional gain is 4.3, the points of the root locus are located on the unit circle, as shown in Fig. 5.5 (a).

Figure 5.6 shows the root locus of  $K \cdot G_{ForcePI}^o(z) \cdot G_{ForceTF}^o(z)$  for various values of  $N_{HR}$  and  $e$ . At 3,000 rpm, the transfer function is evaluated with  $N_{HR}=2$  and  $e = 0$ ; this condition can be also expressed as  $N_{HR}=3$  and  $e = -1.0$ . The two models are identical. In Fig. 5.6 (a), the two zeros in the left half plane for the case  $N_{HR}=3$  move drastically as  $e$  increases from  $-1.0$  to  $+1.0$  (as the spindle speed decreases from 3,000 rpm to 1,500 rpm); this movement is depicted with bold arrows. The dotted arrows show the movement of two zeros in the left half plane for  $N_{HR}=4$ , as  $e$  increases from  $-1.0$  to  $0.0$  (the spindle speed decreases from 2,000 rpm to 1,500 rpm).

The locus in the right half plane can be used for examining the stability limit and tuning the gain. Figure 5.6 (b) shows the stability limit on the unit circle for various spindle speeds. The original system of 2,000 rpm has a stability limit at  $K=4.3$ . As the spindle speed decreases from 3,000 rpm to 1,500 rpm, the critical gain for stability also decreases. Figure 5.6 (c) shows a partial enlargement around the point where  $K=1$  (for  $N_{HR}=3$ ); this represents the original PI controller, located on the constant-damping-ratio line of  $z=0.716$ . The value of  $K$  for a different spindle speed can be determined from the intersection of the root locus and the constant-damping-ratio line of  $z=0.716$ . The tuned values of  $K$  are shown in Fig. 5.6 (c) and are used below.

Figure 5.7 (a) shows the simulation results for the closed loop unit step response of  $K \cdot G_{ForcePI}^o(z) \cdot G_{ForceTF}^o(z)$  with  $e=0$ . Various proportional gains within  $0.5 \sim 4.0$ , and the same integral time constant  $T_i^o$  were used to generate these responses. The rise time (from 10% to 90% of final value) for the controller of Eq. (5.3.35) (whose proportional gain is 1) is about 40 msec, using a sampling time of 5 msec for the simulation. This rise time is less than 45 msec, which is the time interval for one-and-a-half drill revolutions at 2,000 rpm.

Figure 5.7 (b) ~ (e) show the simulation results of the closed loop unit step responses for various spindle speeds. In each graph, the gain  $K$  determined in Fig. 5.6 (c) is taken as the nominal value, and the magnitudes of the responses are multiplied by various proportional gains  $0.5 \sim 4.0$  for comparison with Fig. 5.7 (a). The controller  $G_{ForcePI}^o(z)$  is the same as in Eq. (5.3.35). In all cases, the rise time is shorter than the time interval for one-and-a-half drill revolutions. For each case of 1,714 rpm and 1,500 rpm, the two

models with  $N_{HR}=3$  and  $N_{HR}=4$  are examined. The real model must be expressed with  $N_{HR}=4$ , however the model with  $N_{HR}=3$  provides enough information for applications.

Once the PI controller for the transfer function  $G_{ForceTF}^o(z)$  at 2,000 rpm is given, the PI controller  $G_{ForcePI}(z)$  (for the transfer function  $G_{VoltageInput \rightarrow DigitalForce}(z)$ ) is automatically determined as

$$G_{ForcePI}(z) = \frac{1}{K_{ForceCE}} G_{ForcePI}^o(z) = \frac{K_c^o}{K_{ForceCE}} \cdot \frac{z - (1 - T_s / T_i^o)}{z - 1} = \frac{6.49 \times 10^5}{K_{ForceCE}} \cdot \frac{z - 0.821}{z - 1} \quad (5.3.36)$$

By substituting

$$\begin{aligned} K_{ForceCE} &= K_{A/D} K_{ForceSensor} K_{Fphr \rightarrow Force} K_y b \\ &= 204.8 \cdot 0.02 \cdot K_{Fphr \rightarrow Force} \cdot 1.39 \times 10^6 \cdot 251 \\ &= 1.43 \times 10^9 \cdot K_{Fphr \rightarrow Force} \end{aligned} \quad (5.3.37)$$

(Condition A) into Eq. (5.3.36),

$$G_{ForcePI}(z) = \frac{4.54 \times 10^{-4}}{K_{Fphr \rightarrow Force}} \cdot \frac{z - 0.821}{z - 1} \quad (5.3.38)$$

is obtained.

If the spindle speed is not 2,000 rpm, Eq. (5.3.38) should be multiplied by the gain  $K$  obtained from Fig. 5.6 (c) .

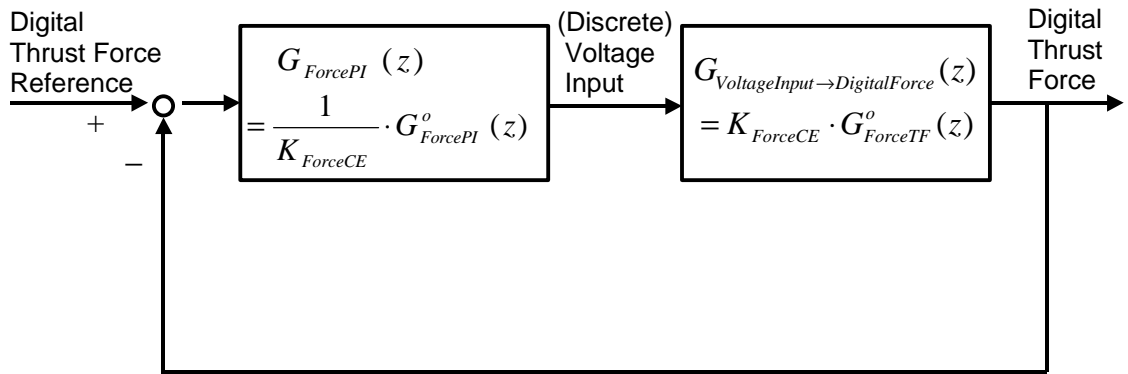
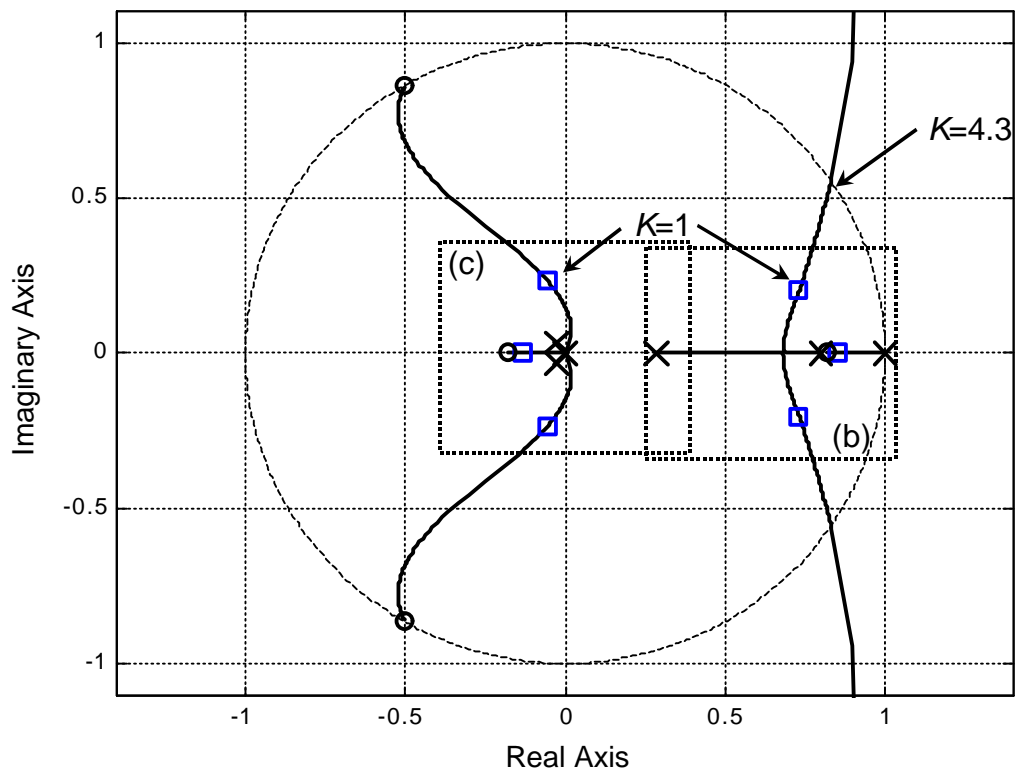
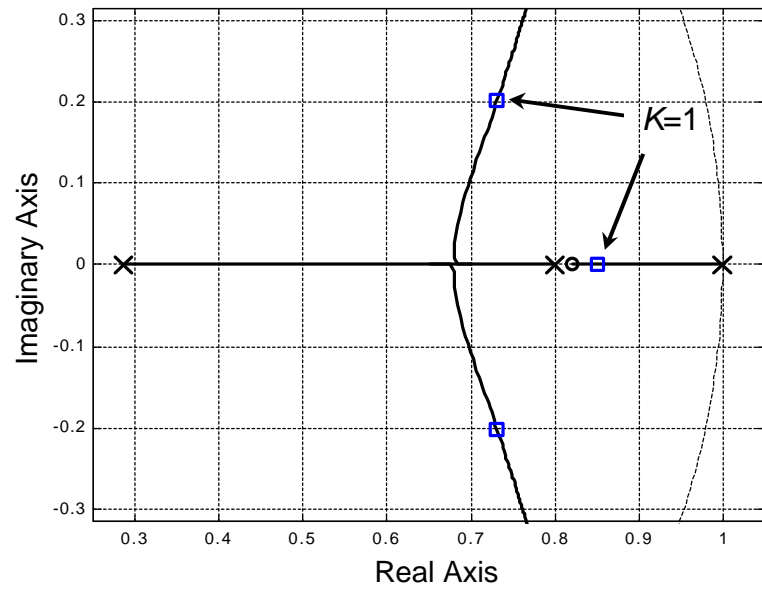


Fig. 5.4 Block Diagram of the Thrust Force Control System.

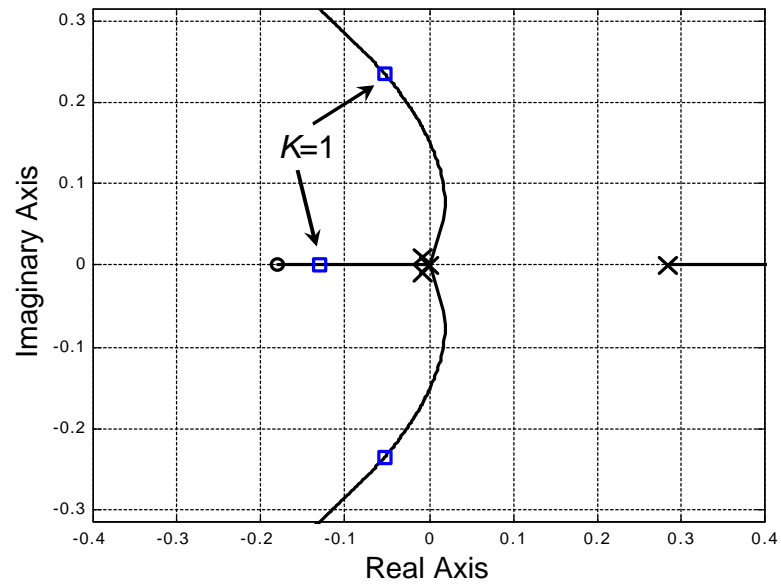


(a) Total

Fig. 5.5 Root Locus of  $K \cdot G_{ForcePI}^o(z) \cdot G_{ForceTF}^o(z)$ . (Three poles are located at the origin. A zero at  $-2.659 + 0j$  is not shown.)



(b) Partial Enlargement



(c) Partial Enlargement

Fig. 5.5 Root Locus of  $K \cdot G_{ForcePI}^o(z) \cdot G_{ForceTF}^o(z)$ . (Three poles are located at the origin. A zero  $-2.659 + 0j$  is not shown.)

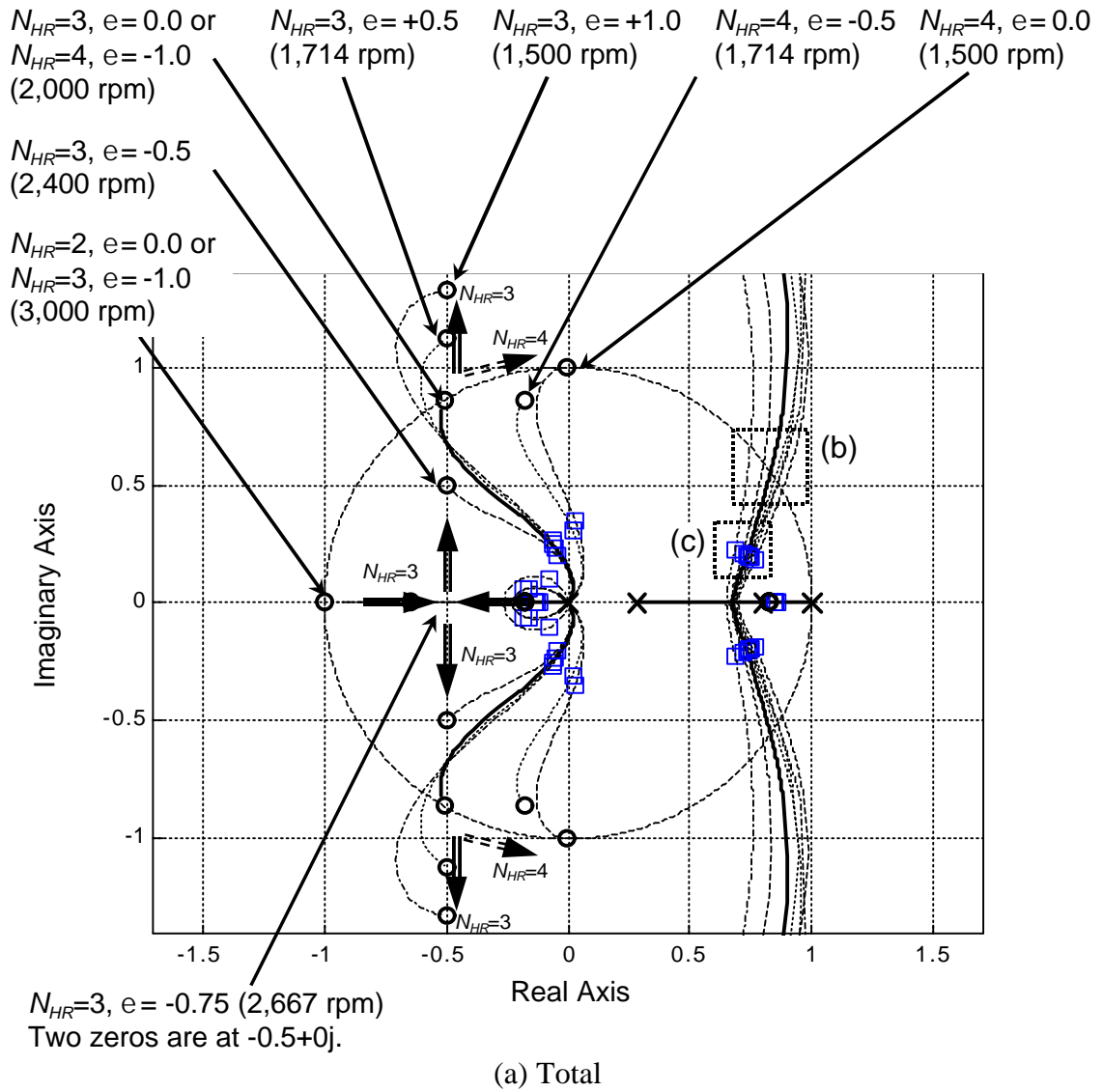
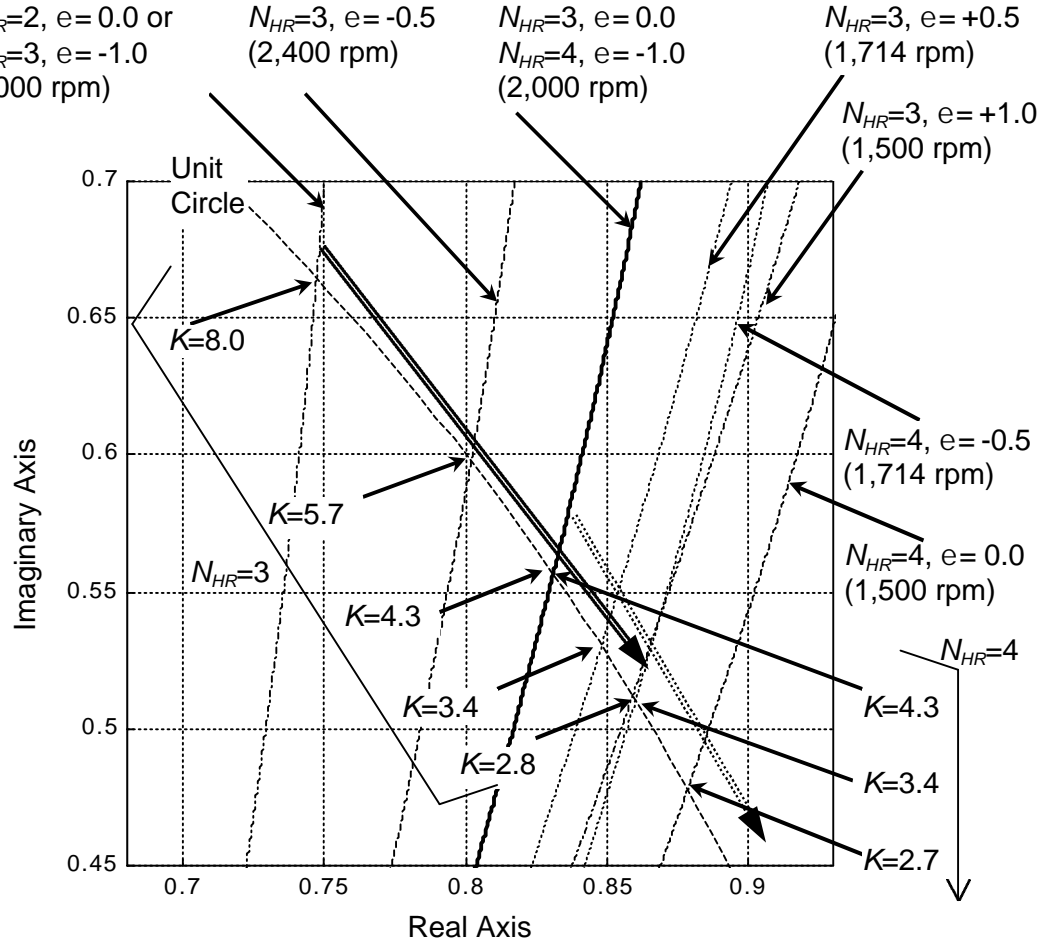


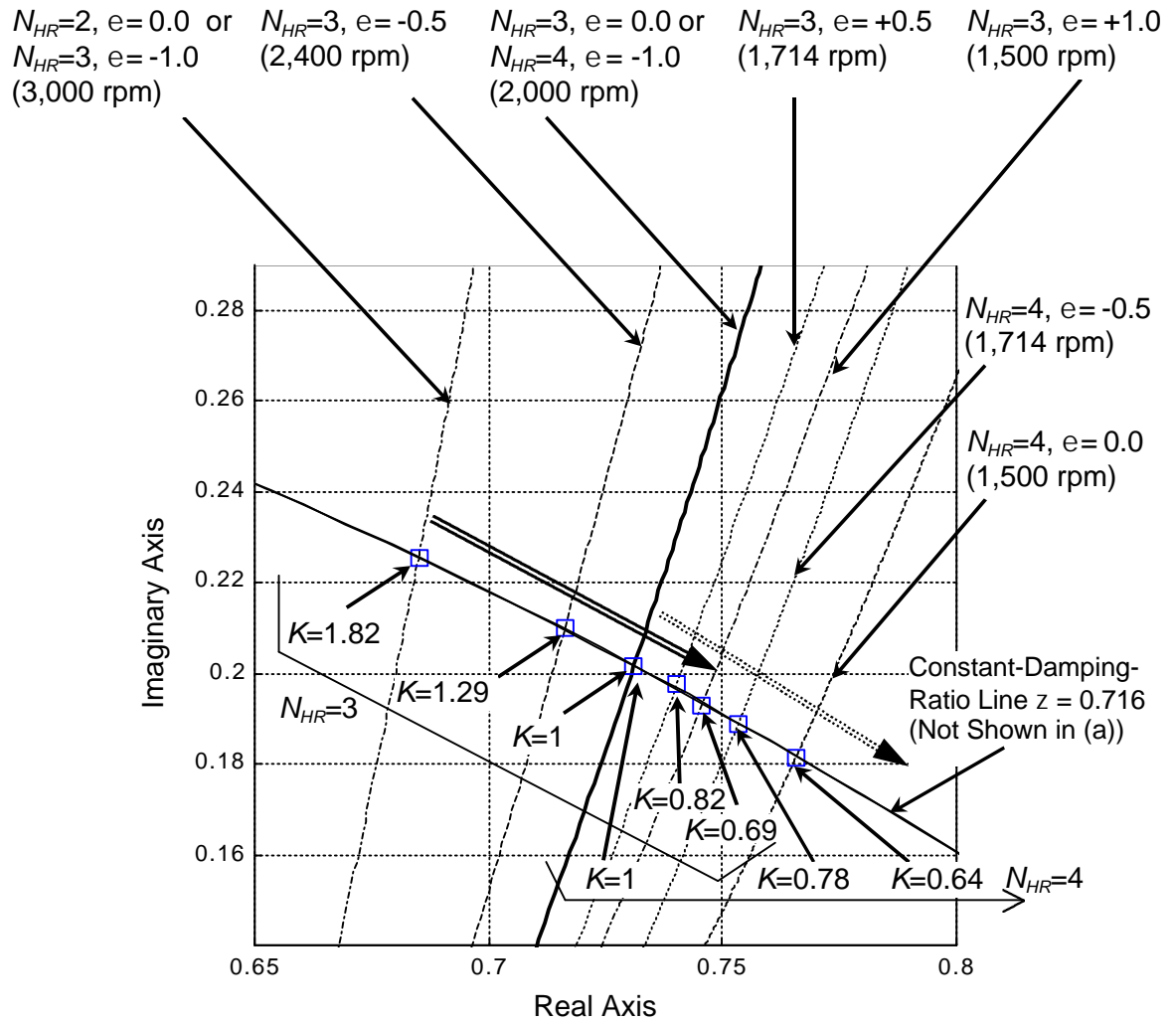
Fig. 5.6 Root Locus of  $K \cdot G_{ForcePI}^o(z) \cdot G_{ForceTF}^o(z)$ . ( $N_{HR}$  poles are located at the origin. A zero at  $-2.659+0j$  is not shown. A zero on the real axis (between  $-1+0j$  and  $0+0j$ ) for  $N_{HR}=4$  is erased. The direction of decreasing spindle speed is indicated by bold arrows for  $N_{HR}=3$ , and broken arrows for  $N_{HR}=4$  about (a) zeros in the left half plane, (b) stability limit, and (c) controller gain. The squares represent the tuned controller gains.)





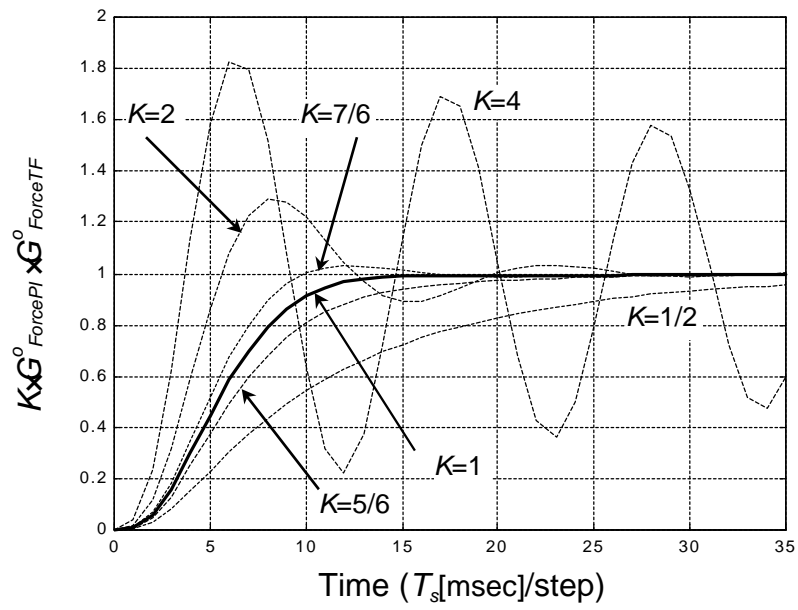
(b) Partial Enlargement (stability limits on the unit circle)

Fig. 5.6 Root Locus of  $K \cdot G_{ForcePI}^o(z) \cdot G_{ForceTF}^o(z)$ . ( $N_{HR}$  poles are located at the origin. A zero at  $-2.659+0j$  is not shown. A zero on the real axis (between  $-1+0j$  and  $0+0j$ ) for  $N_{HR}=4$  is erased. The direction of decreasing spindle speed is indicated by bold arrows for  $N_{HR}=3$ , and broken arrows for  $N_{HR}=4$  about (a) zeros in the left half plane, (b) stability limit, and (c) controller gain. The squares represent the tuned controller gains.)



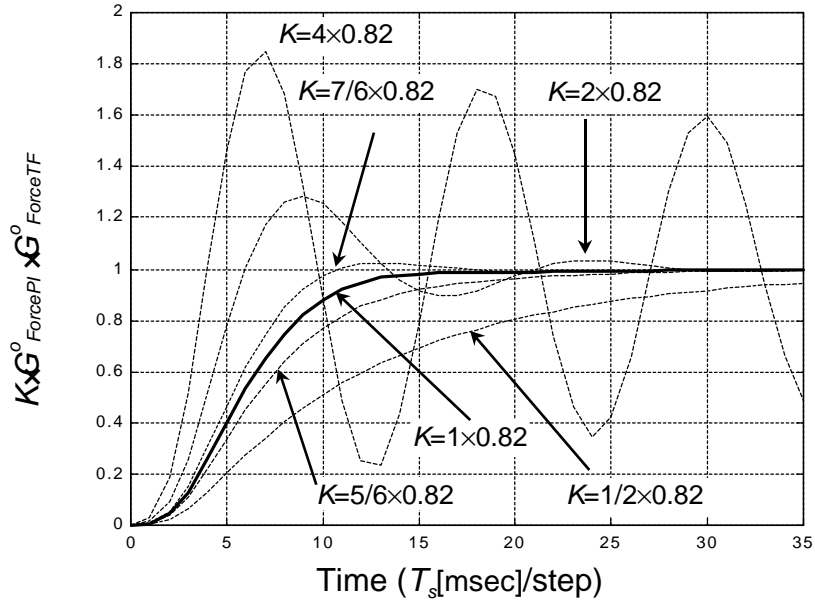
(c) Partial Enlargement with Constant-Damping-Ratio Line  $z = 0.716$   
(for the decision of the controller gains)

Fig. 5.6 Root Locus of  $K \cdot G_{ForcePI}^o(z) \cdot G_{ForceTF}^o(z)$ . ( $N_{HR}$  poles are located at the origin. A zero at  $-2.659+0j$  is not shown. A zero on the real axis (between  $-1+0j$  and  $0+0j$ ) for  $N_{HR}=4$  is erased. The direction of decreasing spindle speed is indicated by bold arrows for  $N_{HR}=3$ , and broken arrows for  $N_{HR}=4$  about (a) zeros in the left half plane, (b) stability limit, and (c) controller gain. The squares represent the tuned controller gains.)

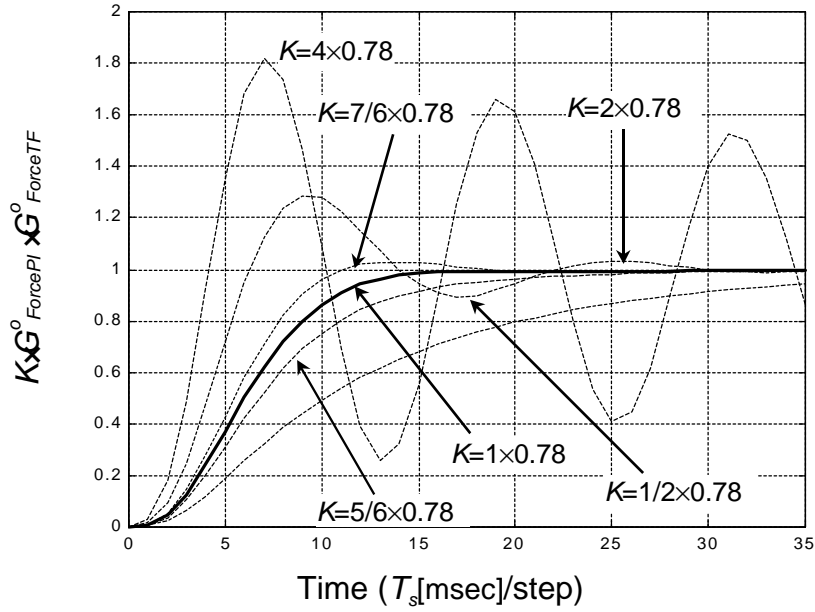


(a)  $e = 0.0$  for  $N_{HR}=3$  or  $e = -1.0$  for  $N_{HR}=4$  (2,000 rpm)

Fig. 5.7 Simulation Result of the Closed Loop Unit Step Response of  $K \cdot G^o_{ForcePI}(z) \cdot G^o_{ForceTF}(z)$ . ( $N_{HR}=3$  with (a) $e = 0$ , (b1) $e = +0.5$ , (c1) $e = +1.0$ , (d) $e = -0.5$  and (e) $e = -1.0$ , and  $N_{HR}=4$  with (b2) $e = -0.5$  and (c2) $e = 0$ .)

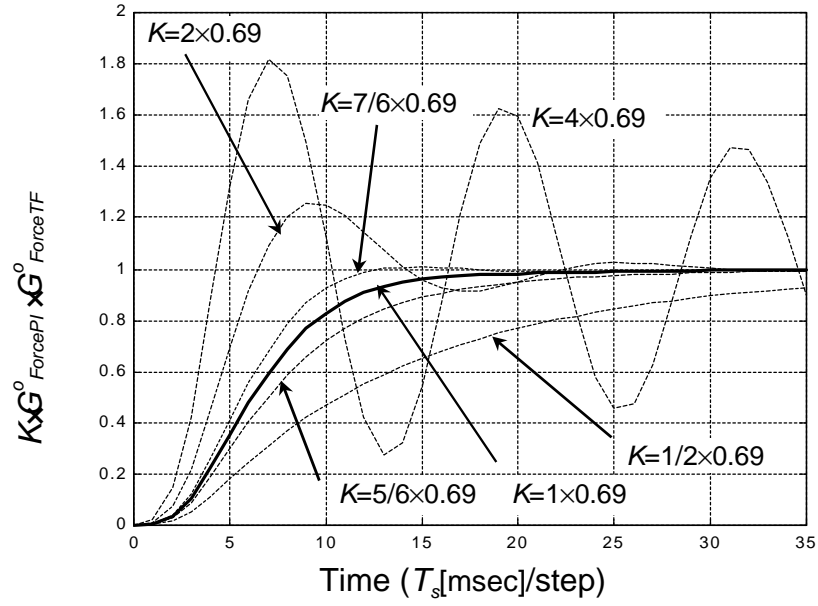


(b1)  $e = +0.5$  for  $N_{HR}=3$  (1,714 rpm)

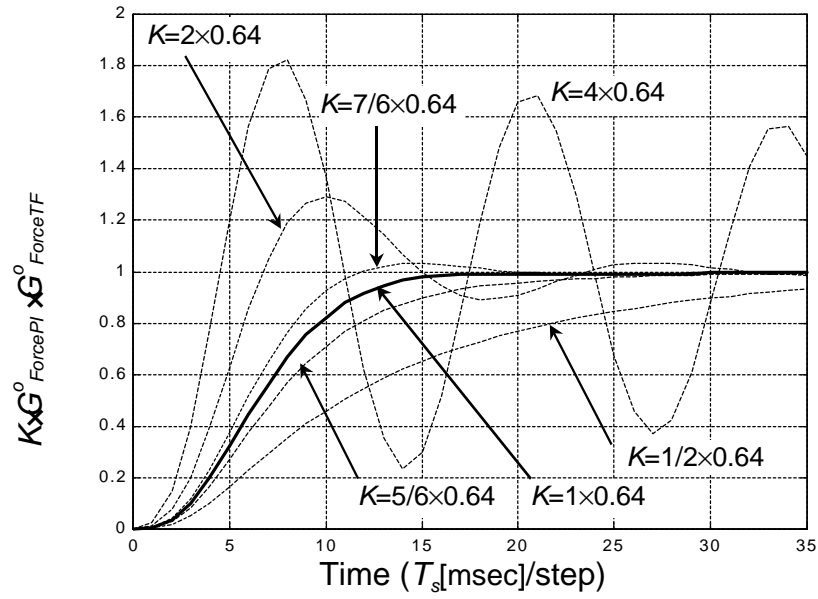


(b2)  $e = -0.5$  for  $N_{HR}=4$  (1,714 rpm)

Fig. 5.7 Simulation Result of the Closed Loop Unit Step Response of  $K \cdot G^o_{ForcePI}(z) \cdot G^o_{ForceTF}(z)$ . ( $N_{HR}=3$  with (a) $e = 0$ , (b1) $e = +0.5$ , (c1) $e = +1.0$ , (d) $e = -0.5$  and (e) $e = -1.0$ , and  $N_{HR}=4$  with (b2) $e = -0.5$  and (c2) $e = 0$ .)

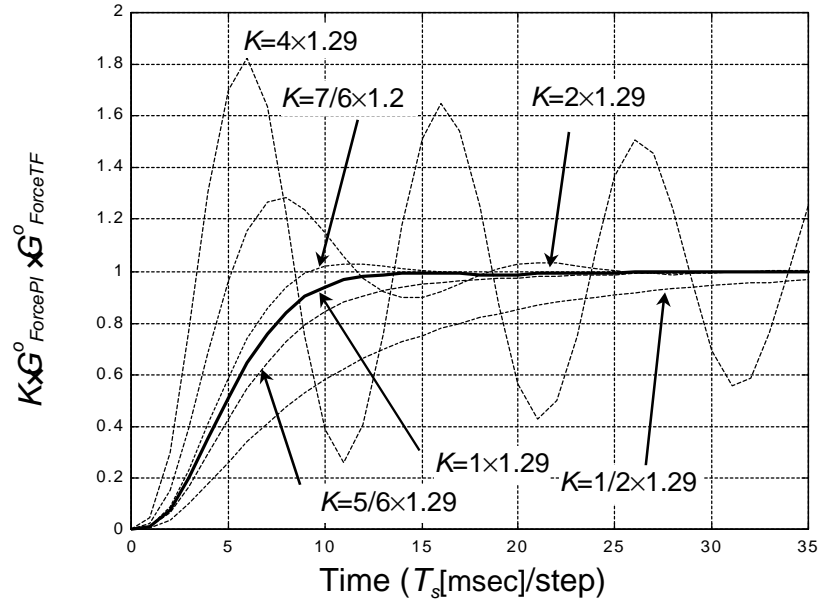


(c1)  $e = +1.0$  for  $N_{HR}=3$  (1,500 rpm)

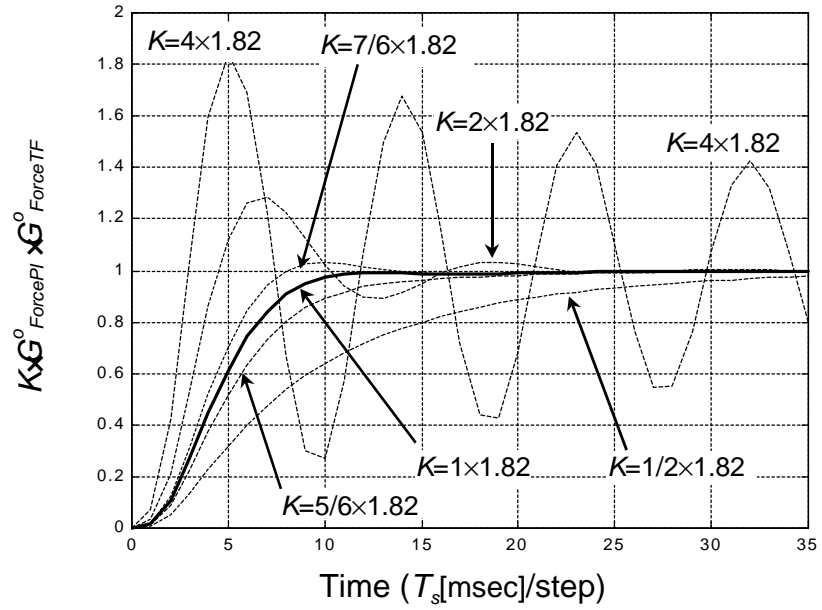


(c2)  $e = 0.0$  for  $N_{HR}=4$  (1,500 rpm)

Fig. 5.7 Simulation Result of the Closed Loop Unit Step Response of  $K \cdot G^o_{ForcePI}(z) \cdot G^o_{ForceTF}(z)$ . ( $N_{HR}=3$  with (a) $e = 0$ , (b1) $e = +0.5$ , (c1) $e = +1.0$ , (d) $e = -0.5$  and (e) $e = -1.0$ , and  $N_{HR}=4$  with (b2) $e = -0.5$  and (c2) $e = 0$ .)



(d)  $e = -0.5$  (2,400 rpm)



(e)  $e = -1.0$  (3,000 rpm)

Fig. 5.7 Simulation Result of the Closed Loop Unit Step Response of  $K \cdot G^o_{ForcePI}(z) \cdot G^o_{ForceTF}(z)$ . ( $N_{HR}=3$  with (a) $e = 0$ , (b1) $e = +0.5$ , (c1) $e = +1.0$ , (d) $e = -0.5$  and (e) $e = -1.0$ , and  $N_{HR}=4$  with (b2) $e = -0.5$  and (c2) $e = 0$ .)

## 5.4 Torque Control

### 5.4.1 Modeling of Torque During Drilling

For torque control, the following equation, which has the same form as Eq. (5.3.2), is assumed:

$$T = K_{Fphr \rightarrow Torque} \cdot f_{phr} \quad (5.4.1)$$

where  $T$  is the torque, and  $f_{phr}$  is FPHR, as defined in the previous section.

Taking the units of the coefficient  $K_{Fphr \rightarrow Torque}$  to be [N-m/ $\mu$ m], the relation between feedrate [ $\mu$ m/sec] and torque [N-m] becomes

$$G_{Feedrate \rightarrow Torque}(s) = K_{Fphr \rightarrow Torque} \frac{1 - e^{-T_{HR}s}}{s} \quad (5.4.2)$$

The charge amplifier's gain is 0.2 N-m/V, and the transfer function of the torque sensor can be simply approximated by a static gain:

$$K_{TorqueSensor} = 5 \text{ [V/N-m]} \quad (5.4.3)$$

The stage dynamics  $G_{VoltageInput \rightarrow Feedrate}(s) = \frac{K_y}{s + a_y}$  and the low-pass filter

$G_{LPF}(s) = \frac{b_{LPF}}{s + b_{LPF}}$  are the same as those for the thrust force controller. Hence, the

transfer function from voltage input to voltage output (corresponding to torque) can be expressed as

$$G_{VoltageInput \rightarrow VoltageTorque}(s) = K_{TorqueSensor} K_{Fphr \rightarrow Torque} \cdot \frac{K_y}{s + a_y} \cdot \frac{1 - e^{-T_{HR}s}}{s} \cdot \frac{b_{LPF}}{s + b_{LPF}} \quad (5.4.4)$$

Both the maximum torque  $10/K_{TorqueSensor} = 2.0$  N-m (=204 kgf-mm) and the resolution of torque  $1/(K_{A/D} \cdot K_{TorqueSensor}) = 9.77 \times 10^{-4}$  N-m (=100 gf-mm) were considered when selecting  $K_{TorqueSensor}$  of Eq. (5.4.3).

The ZOH of Eq (5.4.4) multiplied by  $K_{A/D}$  (204.8 [1/V], same as Eq. (5.3.10)) is

$$G_{VoltageInput \rightarrow DigitalTorque}(z^{-1}) = K_{A/D} \cdot (1 - z^{-1}) \cdot Z \left\{ L^{-1} \left( \frac{K_{TorqueSensor} K_{Fphr \rightarrow Torque} K_y (1 - e^{-T_{HR}s}) b_{LPF}}{s^2 (s + a_y)(s + b_{LPF})} \right) \right\} \quad (5.4.5)$$

With Eq. (5.4.5), the following approximate transfer function (as a function of  $z$ ) is obtained;

$$\begin{aligned} & G_{VoltageInput \rightarrow DigitalTorque}(z) \\ &= \frac{K_{A/D} K_{TorqueSensor} K_{Fphr \rightarrow Torque} K_y b}{a^2 b^2 (b - a)} \cdot \frac{z^{N_{HR}-1} + \dots + z + (1 + e)}{z^{N_{HR}}} \cdot \frac{c_2 z^2 + c_1 z + c_0}{(z - e^{-aT})(z - e^{-bT})} \\ &= K_{TorqueCE} \cdot G_{TorqueTF}^o(z) \end{aligned} \quad (5.4.6)$$

where



$$K_{TorqueCE} = K_{A/D} K_{TorqueSensor} K_{Fphr \rightarrow Torque} K_y b \quad (5.4.7)$$

and

$$G_{TorqueTF}^o(z) = \frac{1}{a^2 b^2 (b-a)} \cdot \frac{z^{N_{HR}-1} + \dots + z + (1+e)}{z^{N_{HR}}} \cdot \frac{c_2 z^2 + c_1 z + c_0}{(z - e^{-aT})(z - e^{-bT})} \quad (5.4.8)$$

which is equal to  $G_{ForceTF}^o(z)$  of Eq. (5.3.17). Figure 5.8 shows the block diagram of the system from the (discrete) voltage input to the measured digital torque.

## 5.4.2 Design of Torque Controller

Since  $G_{TorqueTF}^o(z)$  is the same as  $G_{ForceTF}^o(z)$ , the transfer function  $G_{TorqueTF}^o(z)$  at  $e = 0$  when  $\omega_{spindle} = 209$  rad/sec,  $\omega_s = 1,257$  rad/sec and  $\omega_{LPF} = 251$  rad/sec (Condition A), is the same as Eq. (5.3.31);

$$G_{TorqueTF}^o(z) = \frac{1.476 \times 10^{-8} \cdot (z^2 + z + 1)(z + 0.1801)(z + 2.659)}{z^3 (z - 0.8001)(z - 0.2848)} \quad (5.4.9)$$

and the controller for this plant can be chosen to be the same as  $G_{ForcePI}^o(z)$  of Eq. (5.3.35);

$$G_{TorquePI}^o(z) = K_c \frac{z - (1 - T_s / T_i^o)}{z - 1} = 6.49 \times 10^5 \cdot \frac{z - 0.821}{z - 1} \quad (5.4.10)$$

The overall block diagram of the closed loop system (where  $G_{VoltageInput \rightarrow DigitalTorque}(z)$  is the plant and  $G_{TorquePI}(z)$  is the PI controller) is shown in Fig. 5.9.

The PI controller  $G_{TorquePI}(z)$  for the transfer function  $G_{VoltageInput \rightarrow DigitalTorque}(z)$  is determined as follows:

$$\begin{aligned} G_{TorquePI}(z) &= \frac{1}{K_{TorqueCE}} G_{TorquePI}^o(z) = \frac{K_c^o}{K_{TorqueCE}} \cdot \frac{z - (1 - T_s / T_i^o)}{z - 1} \\ &= \frac{6.49 \times 10^5}{K_{TorqueCE}} \cdot \frac{z - 0.821}{z - 1} \end{aligned} \quad (5.4.11)$$

which, by substituting

$$\begin{aligned} K_{TorqueCE} &= K_{A/D} K_{TorqueSensor} K_{Fphr \rightarrow Torque} K_y b \\ &= 204.8 \cdot 5 \cdot K_{Fphr \rightarrow Torque} \cdot 1.39 \times 10^6 \cdot 251 \\ &= 3.57 \times 10^{11} \cdot K_{Fphr \rightarrow Torque} \end{aligned} \quad (5.4.12)$$

for Condition A, results in

$$G_{TorquePI}(z) = \frac{1.82 \times 10^{-6}}{K_{Fphr \rightarrow Torque}} \cdot \frac{z - 0.821}{z - 1} \quad (5.4.13)$$

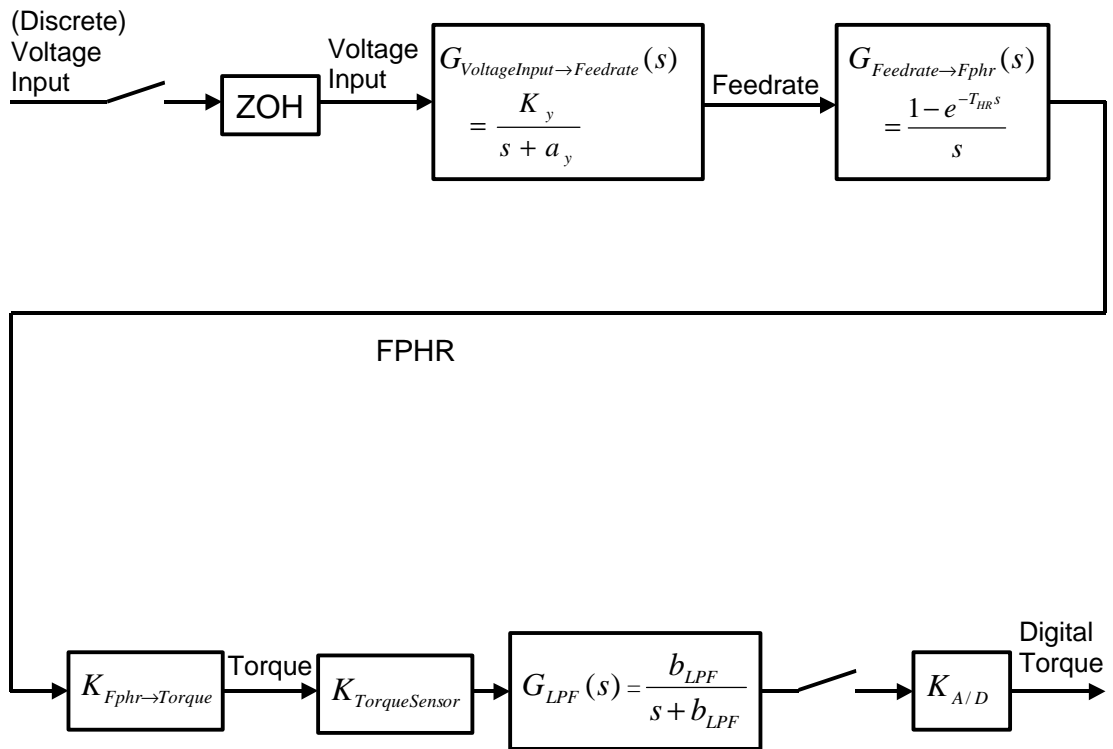


Fig. 5.8 Block Diagram of the Sampled System from the Discrete Voltage Input to the Measured Digital Torque. (The overall transfer function corresponds to  $G_{VoltageInput \rightarrow DigitalTorque}(z)$  in Fig. 5.9.)

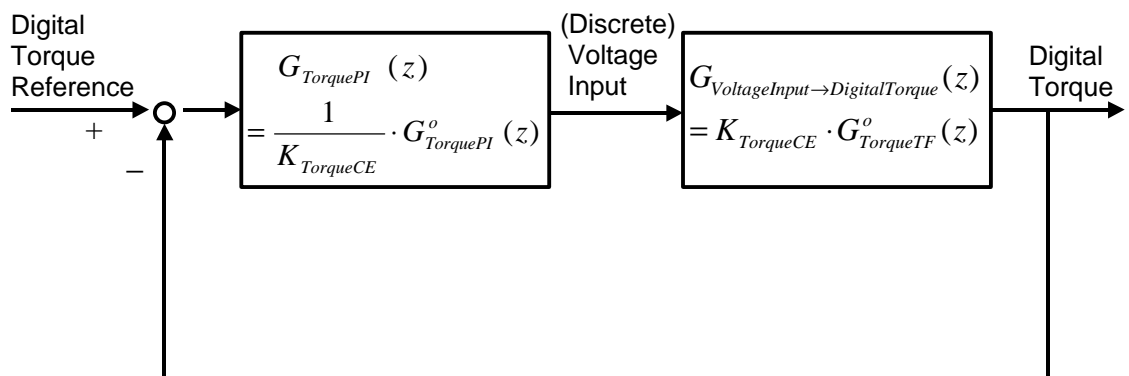


Fig. 5.9 Block Diagram of the Torque Control System.

## 5.5 Supervisory Control

### 5.5.1 Phases of Supervisory Control

In this subsection, the drilling phases that were adopted for our research are introduced. The phases are: *Pre Drilling*, *Entrance Drilling*, *Middle Drilling*, *PreExit Drilling*, *Exit Drilling*, and *Post Drilling*, and are shown in Fig. 5.10. They are defined geometrically except for *PreExit Drilling*, which is the last part of *Middle Drilling*. Figure 5.11 shows the overall architecture of the supervisory controller developed in our research, where those drilling phases are utilized. (The explanation in Fig. 5.11 subdivides *Middle Drilling* into *Middle Drilling 1* and *Middle Drilling 2*. They will be introduced in the next subsection.)

The descriptions of the phases utilize the following constants and variables. The constants are thickness of the workpiece  $H$ , drill point length  $P$ , and drill contact position  $y_0$ , where the first two quantities are measured before drilling commences and  $y_0$  is determined while drilling occurs. In our experiments,  $H > P + h_{PE}$  is always satisfied, where  $h_{PE}$  is the uncut thickness at the onset of failure under the chisel edge.  $h_{PE}$  is less than a few millimeters for the drills used in our experiments. The condition  $H > P + h_{PE}$  is not necessarily true for general manufacturing; a different model should be developed for thinner workpieces. Drill position  $y$  (positive for the approaching direction) is the variable that determines the uncut thickness under the chisel edge,  $h$ , and the depth of the hole,  $h_d$ , when  $y_0 < y \leq y_0 + H$ .

In the actual experiments, the drill position was fixed and the workpiece always approached the drill horizontally. This dissertation, however, describes the setup as if the drill approaches the workpiece in a downward direction.

### 1. *Pre Drilling*

The drill is lowered to the position where its chisel edge touches the top surface of the workpiece; this position is taken as the contact position  $y_0$ . In our experimental setup, the signal that indicates contact can be either the rise of the force signal, or electric contact if (the top surface of) the workpiece is electrically conductive.

### 2. *Entrance Drilling*

*Entrance Drilling* is the phase at the beginning of actual drilling, *i.e.* the conical part of the drill is not completely inside the workpiece, and some portion of the cutting edges are at the same height as the top surface of the workpiece.

In the *Entrance Drilling* phase and in the *Middle Drilling* phase that follows, the hole depth is defined as  $h_d = y - y_0$  and the uncut thickness is defined as  $h = H - y + y_0 = H - h_d$ . The drill position  $y$  in *Entrance Drilling* satisfies  $y_0 < y \leq y_0 + P$ , *i.e.* the hole depth  $h_d$  satisfies  $0 < h_d \leq P$ , and the uncut thickness  $h$  satisfies  $H - P \leq h < H$ .

In Fig. 4.1, Segments AB and BC of the thrust force, and Segment OP of the torque correspond to this phase.

### 3. *Middle Drilling*

The conical part of the drill is completely inside the workpiece. The drill position  $y$  satisfies  $y_0 + P < y \leq y_0 + H$ , *i.e.*  $P < h_d \leq H$  and  $0 \leq h < H - P$ .

Segments CD and DE of the thrust force and Segment PQ of the torque correspond to *Middle Drilling*.

### 3a. *PreExit Drilling*

*PreExit Drilling* is the phase when the thrust force decreases drastically because of the destruction of the thin layers under the chisel edge, which is not necessarily due to delamination. This phase is a part of the *Middle Drilling* phase. The *PreExit Drilling* phase is also defined as the *Middle Drilling* phase when the drilling mechanism is influenced by the existence of the bottom surface.

Using  $h_{PE}$  (the uncut thickness when the destruction under the chisel edge begins), the ranges of the drill position  $y$ , the depth of the hole  $h_d$ , and the uncut thickness  $h$  are found to be  $y_0 + H - h_{PE} < y \leq y_0 + H$ ,  $H - h_{PE} < h_d \leq H$ , and  $0 \leq h < h_{PE}$ , respectively. The real starting point of this phase, however, cannot be measured or predicted precisely, thus  $h_{PE}$  is an unknown value.

Segment DE of the thrust force in Fig. 4.1 corresponds to this transient phase. However, the point D can not be defined for the real thrust force graphs. Only the endpoint of the straight line can be found by visual inspection. This was the procedure used in Section 4.3.

### 4. *Exit Drilling*

Some points on the cutting edges are at the same height as the bottom surface in the *Exit Drilling* phase. The drill position  $y$  satisfies  $y_0 + H < y \leq y_0 + H + P$ .

Segment EF and Segment QR of Fig. 4.1 are in this phase.

### *5. Post Drilling*

After *Exit Drilling* phase, the drill moves downward a little more, then returns to the starting point for the next drilling process.

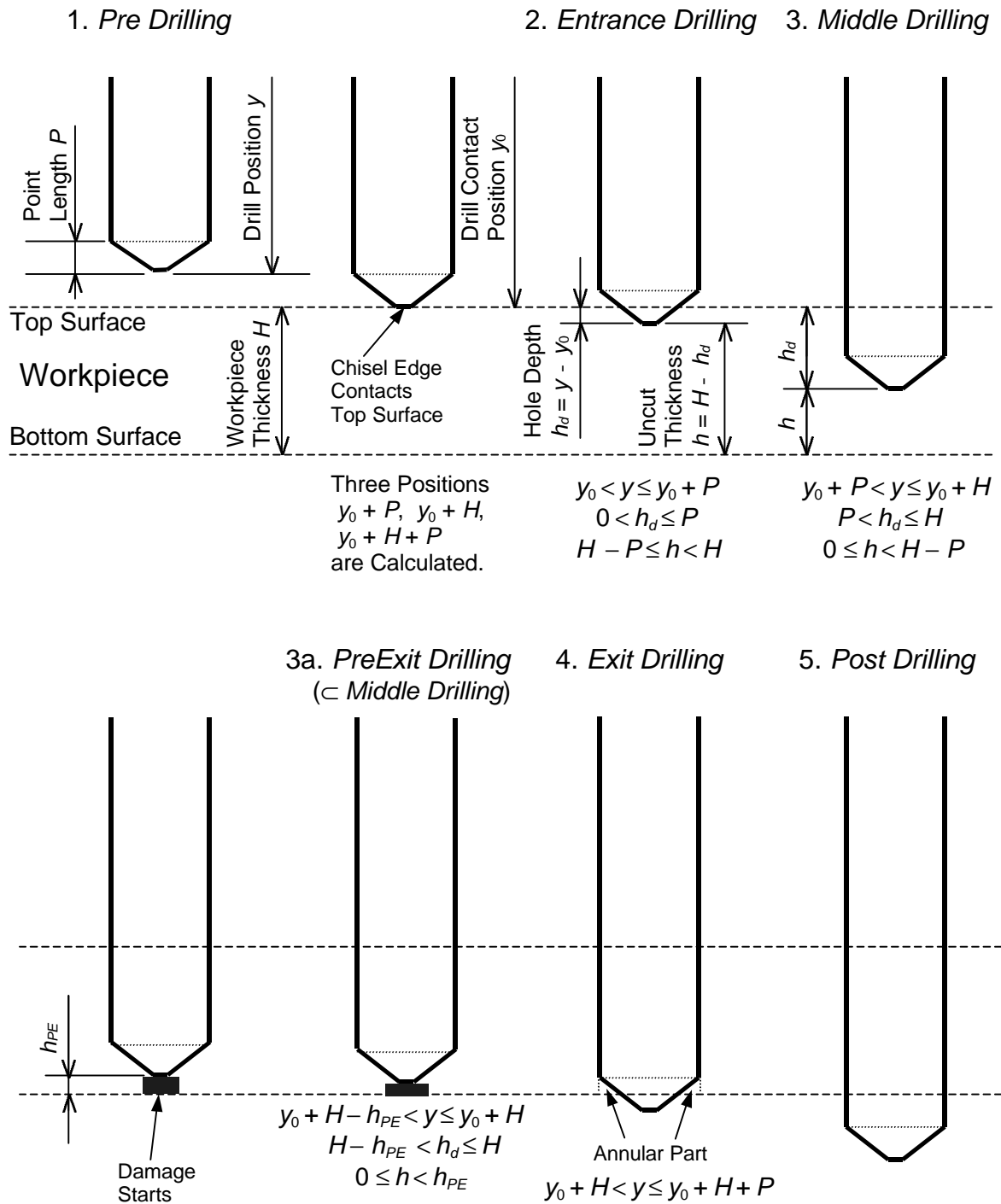


Fig. 5.10 Drill Position and Phase.



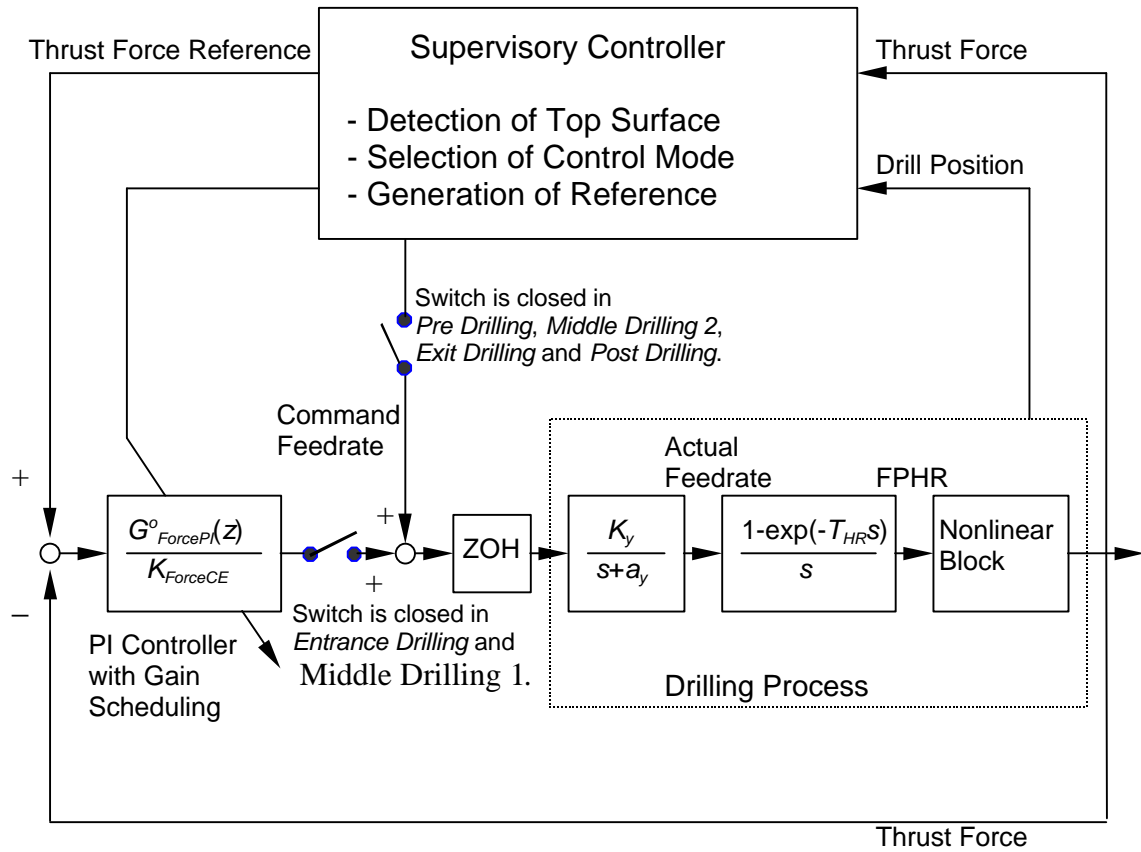


Fig. 5.11 Overall Architecture of the Supervisory Controller.

### 5.5.2 Control Strategy for Each Phase

This subsection describes the control strategy for each of the phases defined in the previous subsection. In this subsection and Sections 6.2 and 6.3, the upper bars signify constant values (see Section 4.2).

In the following description,  $F_{Chisel}$  and  $F_{Cutting}$  are used to explain the control strategy in some phases, where they are treated as if their values were independent, well analyzed, and predicted with small errors. However, their actual values can not be measured, nor can they be independent. Hence, it is not justified to substitute the values obtained in Chapter 4 into the equations in this subsection.  $P_{Chisel}$  (which will be introduced in 2. *Entrance Drilling*) is not the same as the height of the chisel edge, and it can not be constant for all conditions, although it is considered constant in this subsection. These ambiguous values of  $F_{Chisel}$ ,  $F_{Cutting}$  and  $P_{Chisel}$  are used in the manner below to make the complicated relations among many elements intuitively understandable.

#### 1. *Pre Drilling*

The drill approaches the top surface of the workpiece. The position controller for the approach was designed in Section 5.2. It is desirable to make the approach velocity fast in order to reduce air-cutting time, but only if this does not cause any problems during the transition to the next phase, *Entrance Drilling*. Possible problems that can arise are hole location error, drill breakage, or delamination; of these, delamination is considered in this research. In industrial situations, the approximate position of the top surface is known in general. Therefore, the drill should move slowly only within the last few millimeters before actual drilling begins.

The next phase, *Entrance Drilling*, is supposed to be carried out under force control (or velocity control as an open-loop force control). However, the detection of the top surface cannot occur exactly when the chisel edge touches the top surface, nor can the thrust force reference be traced from the beginning. Hence, the approaching speed should be limited so that peel-up delamination does not occur at the beginning of *Entrance Drilling*.

The thrust force does not increase sharply when the chisel edge touches the top surface. In the case of constant feedrate drilling, a hole depth of more than 0.127 mm was required before the influence of the chisel edge was manifested completely, for all the drills that were used in our research. Hence, a conservative value of constant feed  $\bar{f}_{Approach}$  for delamination-free drilling at the beginning of *Entrance Drilling* can be obtained from the following inequality:

$$F_{Chisel}(\bar{f}_{Approach}, d) < F_D(1) = 25.3 \text{ [N]} \quad (5.5.1)$$

Here,  $F_{Chisel}(\bar{f}_{Approach}, d)$  expresses the thrust force at the chisel edge, with a constant feed of  $\bar{f}_{Approach}$  and a drill diameter  $d$ . Table 4.1 and Fig. 4.4 (a) in Section 4.2 can be used to estimate the value of  $F_{Chisel}(\bar{f}_{Approach}, d)$  but with much uncertainty in the preciseness of the predicted value.  $F_D(1)$  is the value of the discrete Hocheng-Dharan equation for a single-layer thickness, which was calculated to be 25.3 N in Section 4.3. This value itself is conservative enough for the case of peel-up delamination. Furthermore, the chisel edge is less likely to cause delamination than the cutting edges. Hence, Eq. (5.5.1) gives a

much smaller value than what is needed to cause real peel-up delamination, assuming  $F_{Chisel}$  represents the correct value. However, the calculated value of  $F_{Chisel}$  is not reliable because it is not derived from direct measurements of the chisel edge thrust force. Therefore, it is not reasonable to loosen the condition of Eq. (5.5.1) when the feed is calculated using Table 4.1 or Fig. 4.4 (a).

If 25.3 N is compared with the chisel edge thrust forces of 9.53 mm drill in Table 4.1, 0.2 mm/rev is the maximum feed that satisfies Eq. (5.5.1), in the case that the feed is chosen from the values listed in Table 4.1, which occur in 0.1 mm/rev increments, or integer multiples of 0.1 mm/rev. (The chisel edge thrust force is 16.8 N at 0.2 mm/rev and 26.0 N at 0.3 mm/rev.) If the spindle speed is 2,000 rpm, 0.2 mm/rev corresponds to the feedrate of 400 mm/min or 6.7 mm/sec. The feedrate becomes 3.3 mm/sec for 1,000 rpm and 13.3 mm/sec for 4,000 rpm. This calculation suggests that the strategy of increasing the spindle speed only in *Pre Drilling* and the very beginning of *Entrance Drilling* is reasonable. In general, higher spindle speeds cause faster wear and shorter lifetime. However, if drilling with a high spindle speed only occurs at the very beginning of *Entrance Drilling*, the influence of drill wear can be made small.

In our experimental setup, the spindle speed cannot be measured directly. Therefore, if the spindle speed at the beginning of *Entrance Drilling* is changed to a normal speed from a higher speed, the force controller will not work well until the spindle speed stabilizes. Thrust force control achieved by varying the feed value during the transient stages of the spindle speed is a topic for future research (a modified experimental setup will need to be utilized).

## 2. Entrance Drilling

The major concern in *Entrance Drilling* is the risk of delamination. One strategy for this phase is thrust force control with a reference value given by the Hocheng-Dharan equation with the minimum value of  $F_D(1)$ . The thrust force value given by the Hocheng-Dharan equation is proportional to the hole depth to the power of 1.5. For example, the value reaches 559 N when the hole depth is only 1 mm, where the point lengths of 6.35, 7.94 and 9.53 mm drill used in our research are about 1.5, 2.3 and 2.5 mm, respectively. Hence, even in *Entrance Drilling*, other conditions such as drill breakage can become the constraints. In Fig. 5.12,  $F_{Middle}$  expresses the optimal thrust force in the *Middle Drilling* phase determined by other conditions.

The thrust force of constant feed  $\bar{f}$  in *Entrance Drilling* is intuitively approximated as follows:

$$F(h_d, \bar{f}, d) \approx \frac{h_d}{P_{Chisel}} F_{Chisel}(\bar{f}, d) \quad (0 < h_d \leq P_{Chisel}) \quad (5.5.2)$$

$$F(h_d, \bar{f}, d) \approx F_{Chisel}(\bar{f}, d) + \frac{h_d - P_{Chisel}}{P - P_{Chisel}} F_{Cutting}(\bar{f}, d) \quad (P_{Chisel} < h_d \leq P) \quad (5.5.3)$$

where  $P_{Chisel}$  represents the depth of the hole at the point when the total influence of the chisel edge appears in the thrust force graph. ( $P_{Chisel}$  is much longer than the chisel edge height measured in Subsection 3.3.1.) In the graph of Fig. 5.12, two thrust force lines  $F(h_d, \bar{f}_{EntA}, d)$  and  $F(h_d, \bar{f}_{EntB}, d)$  for constant feeds with the same spindle speed are shown. If  $\bar{f}_{EntA}$  (expressed as  $\bar{f}_{Approach}$  in the previous part) is used throughout the *Entrance Drilling* phase, the thrust force will only reach  $F_{EntA} = F(P, \bar{f}_{EntA}, d)$ , a value

that is too conservative. On the other hand, if the feed is chosen to satisfy  $F_{EntB} = F(P, \bar{f}_{EntB}, d) = F_{Middle}$ , there is a high possibility of peel-up delamination as the graph shows (around  $Q_{Ent3}$  of Fig. 5.12). Hence,  $F_{EntRef}(h)$  (or  $F_{EntRefa}(h)$  considering the increasing amounts of the cutting edges engaged in cutting) of Fig. 5.12 can provide a good thrust force reference value for the *Entrance Drilling* phase. Since the Hocheng-Dharan equation results in zero when the chisel edge is at the top surface, the value of the discrete Hocheng-Dharan equation for a single-layer thickness is used for the first layer.

When closed-loop force control is applied to trace the thrust force reference, the PI controller designed in Section 5.3 can be utilized. The control gains must be properly selected. The possible choices are (1) constant gain tuned for full engagement drilling, (2) gain scheduling as a function of the position (without gain estimation), and (3) gain scheduling with on-line gain estimation.

On the other hand, Eqs. (5.5.2) and (5.5.3) can be used for open-loop thrust force control, where the thrust force dynamics are neglected. In this case, the thrust force reference must be set well below the curve shown in the figure.

The measurement error of the contact position must be also considered. Especially when the top surface is measured indirectly from the thrust force, there will usually be a difference between the position where the thrust force exceeds the threshold and the actual contact position. Therefore, the control in *PreExit Drilling* should not be dependent on the precise position. It must be robust against the error of the contact position.

### 3. *Middle Drilling* (excluding part 3a, where the thrust force decreases)

Thrust force control with a constant reference value is appropriate for this phase. The thrust force reference can be determined by considering both the drill wear and drilling time. Our objective is to reduce both drill wear and drilling time, but since they are inversely related, this presents a conflict. If the workpiece thickness is much larger than that of the workpiece used in our research, constant torque control should be carried out because torque tends to become larger as the hole is drilled deeper, even if the thrust force is kept constant. Constant torque control can prevent drill breakage and rapid wear of the drill. However, if the approximate slope of torque increase (as a function of drill position, for example) is known, force control with a decreasing thrust force reference can be used instead because there is no need to follow the torque reference exactly.

The determination of the controller gain is another problem. The possible strategies are (1) adjusting based on Table 4.1 or Fig. 4.2 (constant for all drillings of the same condition), (2) adjusting based on the data of the previous drilling (constant for one hole), (3) gain scheduling with off-line estimation (the gain is changed with respect to the drill position), and (4) gain scheduling with on-line gain estimation.

#### 3a. *PreExit Drilling* (including *Middle Drilling* just before *PreExit Drilling*)

In the phase of *PreExit Drilling*, as the chisel edge approaches the bottom surface, the resistance (against the drill's downward motion) decreases drastically. The thrust force at constant feed  $\bar{f}$  in the *PreExit Drilling* phase is intuitively approximated as follows:

$$F(h, \bar{f}, d) \approx F_{Cutting}(\bar{f}, d) + \frac{h}{h_{PE}} F_{Chisel}(\bar{f}, d) \quad (0 \leq h < h_{PE}) \quad (5.5.4)$$

where  $h_{PE}$  was introduced in the previous subsection.

Hence, the condition of a constant feed  $\bar{f}_{Exit}$  for delamination-free drilling in *PreExit Drilling* can be obtained from the following inequality:

$$F_{Cutting}(\bar{f}_{Exit}, d) + \frac{h_t}{h_{PE}} F_{Chisel}(\bar{f}_{Exit}, d) < F_D(1) = 25.3[\text{N}] \quad (5.5.5)$$

In Table 4.1,  $F_{Cutting} = 22.0$  N and  $F_{Chisel} = 7.3$  N when the feed is 0.1 mm/rev, and  $F_{Cutting} = 24.0$  N and  $F_{Chisel} = 16.8$  N at 0.2 mm/rev. By substituting these two sets of forces and  $h_t = 0.127$  mm into Eq. (5.5.5), we obtain  $h_{PE} > 0.28$  mm for 0.1 mm/rev and  $h_{PE} > 1.64$  mm for 0.2 mm/rev. In our drilling experiments, the former is always satisfied but the latter is not. The conclusion is that 0.1 mm/rev is the maximum feed (going by 0.1 mm/rev step increments) that satisfies Eq. (5.5.5) for 9.53 mm drill.

However, in Subsection 4.3.2, it was shown that the intuitive approximation (used in Eq. (5.5.4)):

$$F(0, \bar{f}_{Exit}, d) \approx F_{Cutting}(\bar{f}_{Exit}, d) \quad (5.5.6)$$

includes a large error. One of the reasons is that the annular part at  $h = 0$  is not the same as the corresponding part at  $h \geq h_{PE}$ . It was also discussed in Subsection 4.3.2 that further study on bulging is necessary for the Hocheng-Dharan model to be applied. Furthermore, the values of  $F_{Chisel}$  and  $F_{Cutting}$  are ambiguous as discussed at the beginning of this



subsection. Therefore, the above conclusion gives only an approximate value to be referred, although it is still valuable in the design of a supervisory controller.

In the *PreExit Drilling* phase, either thrust force or position (velocity) can be the controlled variable. The position (velocity) control can be regarded as an open-loop thrust force control. For thrust force control (both closed-loop control and open-loop control), there are two strategies for determining the thrust force reference. The first utilizes the Hocheng-Dharan equation, as was done in the *Entrance Drilling* phase. The single-layer thickness value from the Hocheng-Dharan equation ( $F_D(1)$ ) is adopted for the last layer. In Fig. 5.13,  $F_{PreExitRef1}(h)$  is the thrust force reference given by  $F_D(1)$ ,  $F_{PushOut}$  and  $F_{Middle}$ . The reference is significantly greater than  $F(h_d, \bar{f}_{PreExit2}, d)$ , the thrust force curve for the constant feed  $\bar{f}_{PreExit2}$ , which is the maximum constant feed without delamination. (The decreasing thrust force line also depends on the spindle speed; therefore the above discussion assumes a constant spindle speed.)

However, there is a problem with this strategy when thrust force decrease is considered. In Fig. 5.13,  $F(h_d, \bar{f}_{PreExit5}, d)$  is the thrust force curve when constant feed  $\bar{f}_{PreExit5}$  (which gives  $F_{Middle}$  before the *PreExit Drilling* phase) is maintained throughout the *PreExit Drilling* phase. The thrust force starts decreasing at  $P_5$ , before  $F_{PushOut}$  becomes the effective constraint of  $F_{PreExitRef1}(h)$ . Hence, if  $F_{PreExitRef1}(h)$  is used as the reference for thrust force closed-loop control, the feedrate will be increased. This may cause a different type of delamination even if the thrust force is always kept below  $F_{PushOut}$ .

Figure 5.14 shows the second strategy of setting the thrust force reference. Let the five points  $P_1 \sim P_5$  be the points where thrust force starts decreasing for constant feeds  $F_{PreExit1} \sim F_{PreExit5}$ , respectively.  $F_{PreExitRef2}(h)$  is the new thrust force reference curve,

constructed by connecting points  $P_1 \sim P_5$  and the horizontal line of  $F_D(1)$ . This strategy avoids the sudden decrease of thrust force (due to destruction under the chisel edge) as long as possible by trying not to enter the *PreExit Drilling* phase.  $F_{PreExitRef2a}(h)$  is determined by considering the natural decrease of the thrust force (cf.  $F_{EntRefa}(h)$  of Fig. 5.12).

In the real thrust force curves, the point P cannot clearly be found; also it is affected by many factors such as drill wear. Furthermore, the delay of the transient response to the decrease of the thrust force reference value can easily cause delamination if the thrust force reference curve has a little margin. Figure 5.15 shows a practical strategy for determining the thrust force reference curve. The set of the thrust force curves of Fig. 4.8 are utilized as an example for the explanation. The relation between  $F_{PreExitRef3}(h)$  and  $F_{PreExitRef3a}(h)$  is the same as that of  $F_{PreExitRef2}(h)$  and  $F_{PreExitRef2a}(h)$  mentioned above. It is not meaningful to trace the thrust force reference precisely in the *PreExit Drilling* phase. The most important objective is to decrease the feed below  $\bar{f}_{PreExit2}$  (given in Fig. 5.14) or to decrease the thrust force below  $F(h_d, \bar{f}_{PreExit2}, d)$  before entering the *PreExit Drilling* phase.

Since a constant feedrate is maintained in *Exit Drilling* (see 4. *Exit Drilling*), the same feedrate can be utilized in the last part of *Middle Drilling*. In the case of this strategy, the value of the feedrate given for *Exit Drilling* is used as the threshold to change the controller from force control to position control. In this dissertation, the *Middle Drilling* phase in force control is called the *Middle Drilling 1* phase, and the *Middle Drilling* phase in position or velocity control is called the *Middle Drilling 2* phase.

Open-loop thrust force control is also a possible strategy (cf. 2. *Entrance Drilling*). In this case, the thrust force reference must be set substantially below the curve shown in Fig. 5.15.

#### 4. *Exit Drilling*

In the case of metal drilling, the annular part under the cutting edge in the *Exit Drilling* phase (see Fig. 5.11) can be analyzed and thrust force control can be achieved (Lee, 1989). However, the inhomogeneous structure of composite materials makes it difficult to analyze their structure under the cutting edge during *Exit Drilling*.

Delamination can still occur in the *Exit Drilling* phase. However, we have not studied the delamination model for this phase. In our experiments, the drilling for this phase is conducted with a constant feedrate that is given by the lowest feedrate utilized in the *PreExit Drilling* phase (generally, the feedrate at the end of *PreExit Drilling*, i.e. the feedrate at the beginning of *Exit Drilling*). This decision is not supported by any analysis. For optimal control in this phase, further study on the annulus is necessary.

For the same reason mentioned in *Pre Drilling*, higher spindle speed during *Exit Drilling* may be a good strategy. However, the drill wears faster at higher spindle speeds, which must be considered from the viewpoint of minimizing the total cost.

#### 5. *Post Drilling*

The drilling in the *Post Drilling* phase has the effects of eliminating small burrs and polishing the drilled hole. If these effects are not considered important, it is better to make the time interval of the *Post Drilling* phase as short as possible. In preparation for

drilling of the next hole, the optimal strategy is to use maximum upward acceleration during the move from  $y = y_0 + H + P$  (where velocity is downward) to  $y = y_0$  (where velocity is upward).

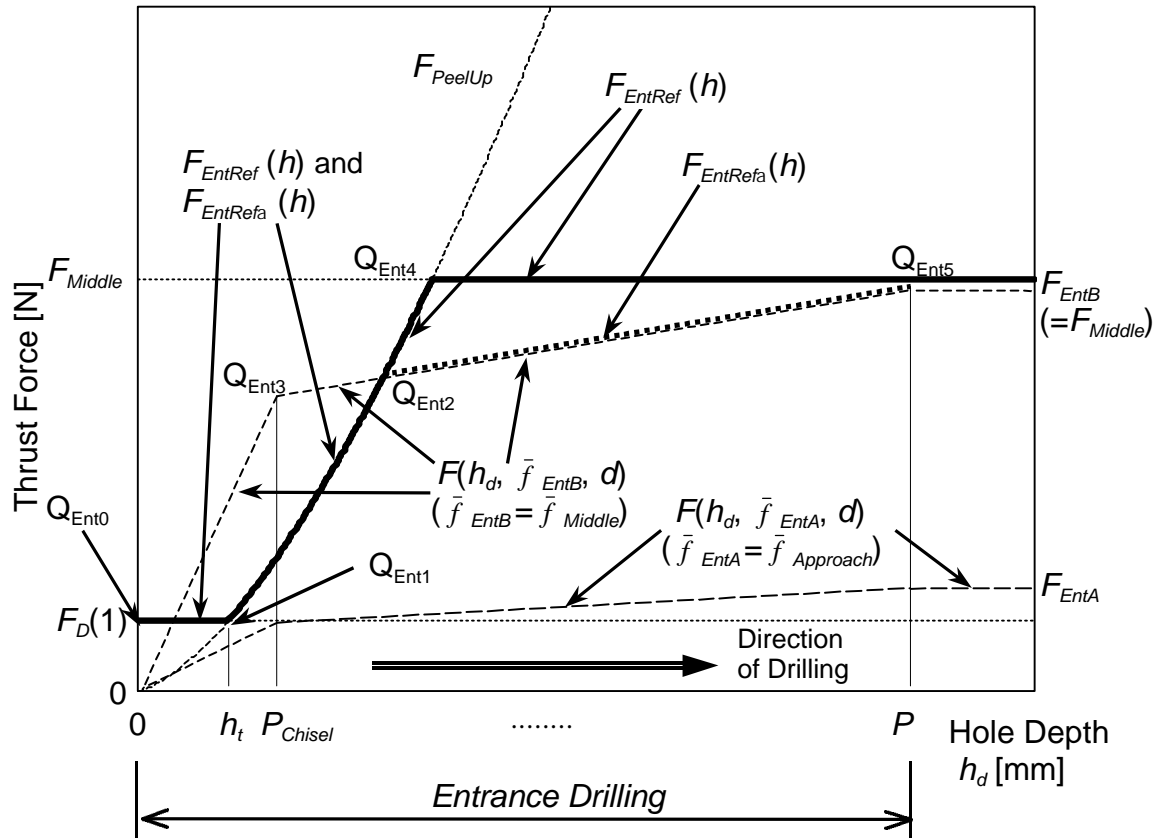


Fig. 5.12 Thrust Force Reference Determined by the Hocheng-Dharan Equation in the *Entrance Drilling* Phase.

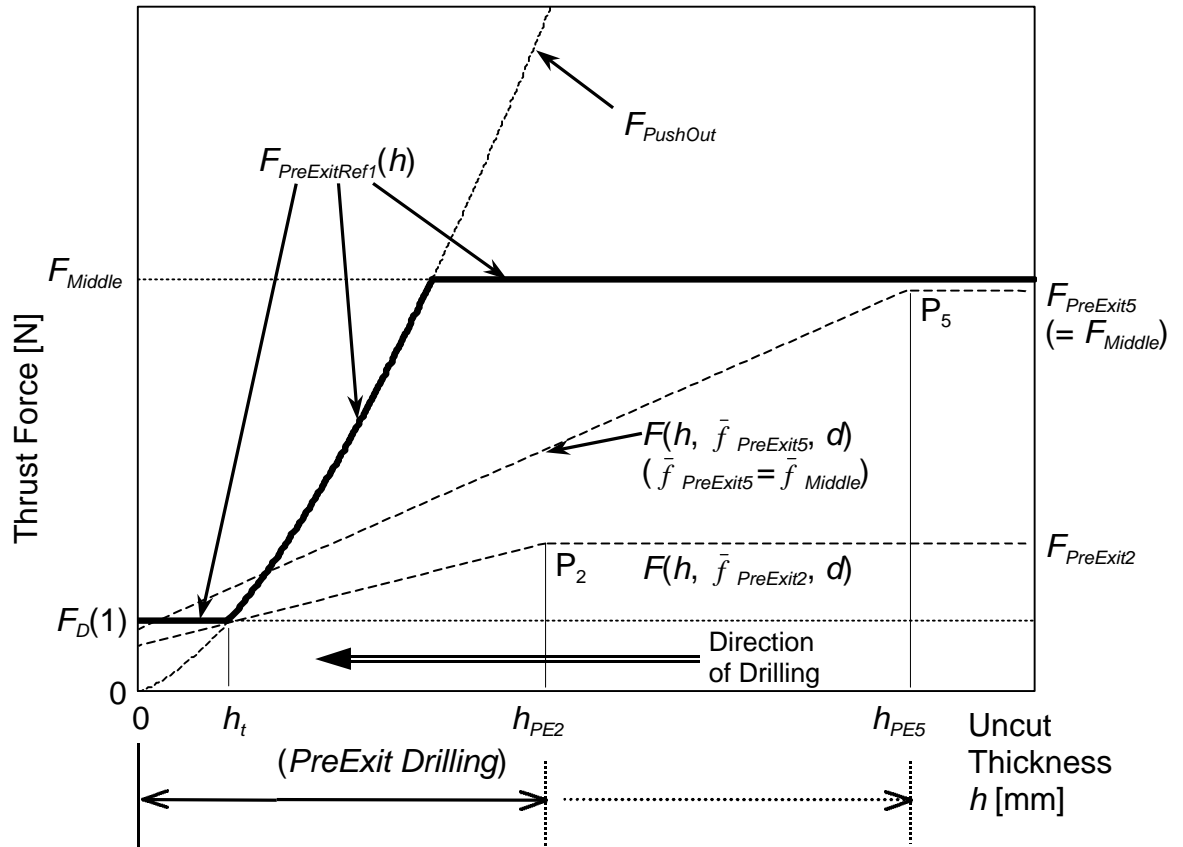


Fig. 5.13 Thrust Force Reference Determined by the Hocheng-Dharan Equation in the *PreExit Drilling* Phase.

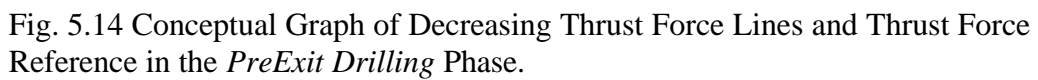


Fig. 5.14 Conceptual Graph of Decreasing Thrust Force Lines and Thrust Force Reference in the *PreExit Drilling* Phase.

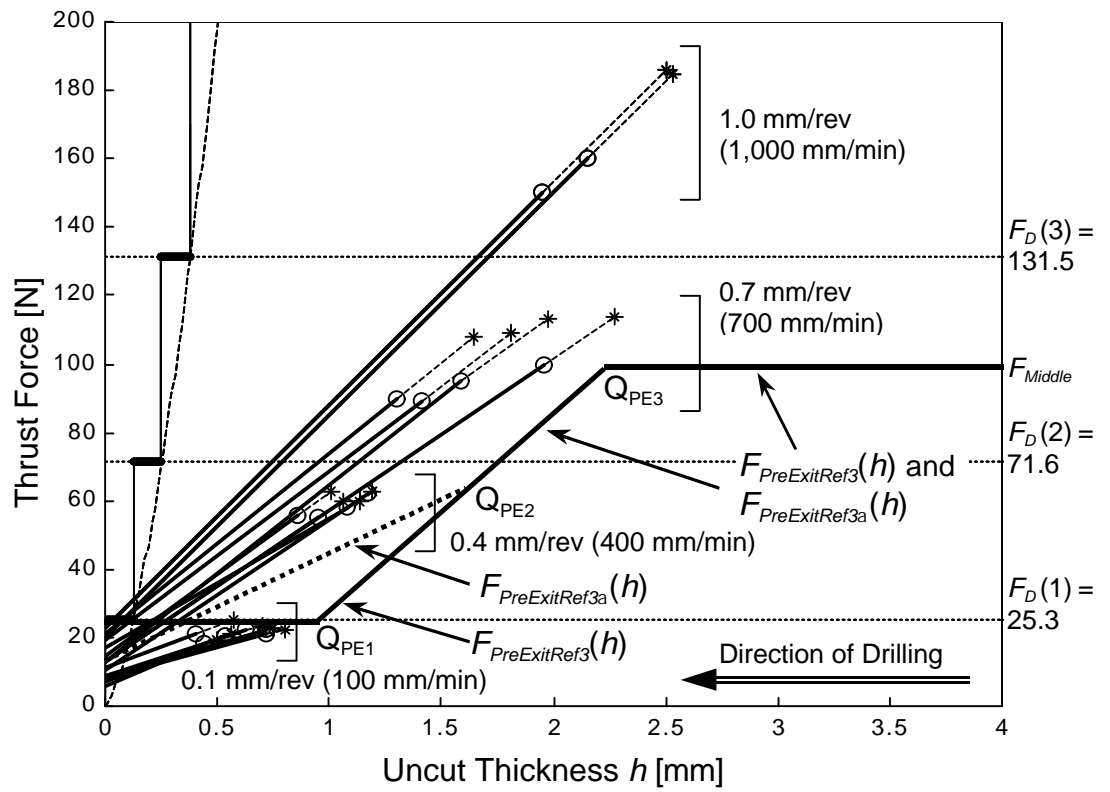


Fig. 5.15 Example of Thrust Force Reference Determined by Experimental Data of Decreasing Thrust Force in the *PreExit Drilling* Phase. (The decreasing thrust force lines are the same as those of Fig. 4.8.)



## 5.6 Summary

We presented the design of position, thrust force and torque controllers for the drilling process, and proposed a supervisory controller for drilling of composite materials by combining the separate controllers. Dynamic models for thrust force and torque were developed based on the assumption that thrust force and torque were proportional to FPHR, which corresponds to the thickness of the uncut chip. A discrete thrust force (or torque) model was obtained by applying a ZOH to the continuous thrust force (torque) model. The discrete model was first developed for the case when there were six samplings during one spindle revolution. Next, the model was generalized for an arbitrary spindle speed with four to eight samplings in one revolution. A discrete PI controller for the discrete model was developed for the six-sample dynamic model, and then tuned for different spindle speeds by varying the total proportional gain. Root loci were used for determining the stability limits and for tuning. The drilling process was divided into five phases (*Pre Drilling*, *Entrance Drilling*, *Middle Drilling* including *PreExit Drilling*, *Exit Drilling*, and *Post Drilling*) for the development of the supervisory controller. Each phase requires a unique control strategy for a satisfactory drilling process. Delamination-free drilling was emphasized in the development of the controller.

## CHAPTER 6

### Supervisory Control for Drilling Composite Materials

#### $\frac{3}{4}$ Experiment $\frac{3}{4}$

In this chapter, composite-material drilling experiments are described and the results are shown. Section 6.1 gives the construction method for the composite material that was used in our experiments. Section 6.2 describes the experiments in which the composite materials were drilled. Section 6.3 shows a typical experimental result when our supervisory controller conducted a delamination-free drilling process.

#### 6.1 Carbon Fiber Reinforced Laminates

*The composite materials used in the experiments were produced as follows:*

##### 1. Cutting Sheet

High-strength woven carbon fiber (T300/934, Carbon/Epoxy) was cut into sheets of 254 mm  $\times$  254 mm. Half of the sheets were cut parallel to the fabric grain and the rest were cut at an angle of 45° to the fabric grain.

##### 2. Making Prepreg Stack

A quasi-isotropic symmetric lay-up was used throughout, with a lay-up of  $[0/45]_{31S}$ . In this notation, '0' refers to a single layer of fabric, which consists of an

equal number of  $0^\circ$  and  $90^\circ$  fibers, and '45' refers to a layer of fabric oriented at  $45^\circ$ . One layer corresponds to 5mil (0.127mm) when the plate is cured. In the case of the above lay-up, 61 plies were stacked to make the specimen of 7.72 mm thickness and 0.63 fiber volume fraction after curing. In the case of different number of plies and different thickness, similar lay-up and the same single-layer thickness were kept.

### 3. Curing

Pressure of 0.69 MPa was applied and the specimen was heated at  $177^\circ\text{C}$  for 2 hours. After that, the heater was turned off and the plate was kept at the same pressure until the temperature fell below  $60^\circ\text{C}$ .

### 4. Cutting Plates

Each plate of  $254\text{ mm} \times 254\text{ mm} \times 7.72\text{ mm}$  was cut into five plates of  $51\text{ mm} \times 254\text{ mm} \times 7.72\text{ mm}$ . With these dimensions, each plate could be attached to Fixture 1 and could be drilled while measuring thrust force and torque.

The material properties of the carbon fiber reinforced material used in our research were  $G_{IC} = 260\text{ J/m}^2$ ,  $E = 41.6\text{ GPa}$ ,  $\nu = 0.3$  and  $h_t = 0.127\text{ mm}$ .

## 6.2 Design Parameters of Supervisory Controller

In this subsection, the key parameters of the supervisory control chosen in our experiments are introduced using Figs. 5.12 and 5.15. In the following case, the drill diameter  $d$  is 9.53 mm and the spindle speed is 2,000 rpm.

(a) Approaching Feed in *Pre Drilling*:  $\bar{f}_{Approach}$ , and Feedrate:  $\bar{V}_{Approach}$

In Section 5.5, the maximum constant approaching feed  $\bar{f}_{Approach} = 0.2$  mm/rev (for delamination-free drilling at the beginning of *Entrance Drilling*, with 9.53 mm drill) was obtained from the following inequality:

$$F_{Chisel}(\bar{f}_{Approach}, d) < F_D(1) = 25.3 \text{ [N]} \quad (6.2.1)$$

In the experiment of the next section,  $\bar{f}_{Approach} = 0.06$  mm/rev ( $\bar{V}_{Approach} = 2.0$  mm/sec for 2,000 rpm) is adopted, which implies a safety factor of 3.3 with respect to the feed (feedrate).

(b) Thrust Force Threshold (for determining the Contact Position):  $F_{Th}$

We chose  $F_{Th} = 4.88$  N, which corresponds to the digital value of 20.

(c) Contact Position Measurement Error:  $h_{dTh}$

The value of  $h_{dTh}$  depends strongly on the value of  $F_{Th}$ . It was estimated as less than 0.1 mm for the case of the above choices of  $\bar{V}_{Approach}$  and  $F_{Th}$ . In our experiments, the

contact position was approximated as the position when the thrust force exceeded  $F_{Th}$ . This makes the thrust force reference in the *Entrance Drilling* phase more conservative. The thrust force references in the *Middle Drilling* phase and in the *PreExit Drilling* phase were determined so that the controller was robust enough to allow  $h_{dTh}$  to be neglected.

(d) Constant Thrust Force Reference in *Middle Drilling*:  $F_{Middle}$

We utilized  $F_{Middle} = 60$  N for our experiments only because it is much lower than the drill buckling limit, and the torque accompanied with the thrust force  $F_{Middle} = 60$  N is much lower than the drill breakage torque limit. Deciding the optimal value requires statistical calculation of total cost.

(e) Thrust Force Reference in *Entrance Drilling*:  $F_{EntRefA}(h)$

The thrust force reference we utilized is shown as  $F_{EntRefA}(h)$  in Fig. 5.12. In this figure,  $Q_{Ent0} = (0\text{mm}, 25.3\text{N})$ ,  $Q_{Ent1} = (0.127\text{mm}, 25.3\text{N})$ , and  $Q_{Ent5} = (P, F_{Middle}) = (2.5\text{mm}, 60\text{N})$ .  $Q_{Ent2}$  is given by connecting  $Q_{Ent3} = (P_{Chisel}, F_{Chisel}(\bar{f}_{Middle}, d)) = (0.2\text{mm}, 33.3\text{N})$  and  $Q_{Ent5}$ , where 0.2 mm is used as a typical value of  $P_{Chisel}$  and  $\bar{f}_{Middle} = 0.37$  mm/rev satisfies  $F(P, \bar{f}_{Middle}, d) = F_{Middle}$ . (In Table 4.1, the thrust force is  $F = 52.0$  N at 0.3 mm/rev and  $F = 64.0$  N at 0.4 mm/rev; the chisel edge thrust force is  $F_{Chisel} = 26.0$  N at 0.3 mm/rev and  $F_{Chisel} = 37.0$  N at 0.4 mm/rev. By linearization,  $\bar{f}_{Middle} = 0.37$  mm/rev is obtained from the two thrust forces, and  $F_{Chisel}(\bar{f}_{Middle}, d) = 33.3\text{N}$  is obtained from the two chisel edge thrust forces.)

The line  $Q_{Ent3}Q_{Ent5}$  corresponds to the increase of the working area of the cutting edges.

In the experiment of the next section, the equation of the line  $Q_{Ent3}Q_{Ent5}$  is

$$F(h_d) = 11.6 \cdot h_d + 31.0 \quad (6.2.2)$$

The line is expressed as oblique dashed lines in *Entrance Drilling* of Fig. 6.1 (a) and (b).

(f) Thrust Force PI Controller:  $G_{ForcePI}(z)$

A constant gain controller tuned in *Middle Drilling* was considered; no gain scheduling or adaptive control was attempted. In that case, the thrust force controller can be designed as follows. The value of  $K_{Fphr \rightarrow Force}(\bar{f}_{Middle}, d)$  in Eq. (4.2.4) is obtained as

$$K_{Fphr \rightarrow Force}(\bar{f}_{Middle}, d) = 2 \cdot \frac{F(\bar{f}_{Middle}, d)}{1000 \cdot \bar{f}_{Middle}} = 0.002 \frac{F_{Middle}}{\bar{f}_{Middle}} \quad (6.2.3)$$

Figure 4.3 (a) can be also used to obtain  $K_{Fphr \rightarrow Force}$  for the feed  $\bar{f}_{Middle}$ . By substituting

$K_{Fphr \rightarrow Force}$  of Eq. (6.2.3) into Eq. (5.3.38), the controller:

$$\begin{aligned} G_{ForcePI}(z) &= \frac{4.54 \times 10^{-4}}{K_{Fphr \rightarrow Force}} \cdot \frac{z - 0.821}{z - 1} = \frac{0.227 \bar{f}_{Middle}}{F_{Middle}} \cdot \frac{z - 0.821}{z - 1} \\ &= \frac{0.227 \times 0.37}{60} \cdot \frac{z - 0.821}{z - 1} = 1.40 \times 10^{-3} \cdot \frac{z - 0.821}{z - 1} \end{aligned} \quad (6.2.4)$$

is obtained.

(g) Decreasing Thrust Force Reference in *Middle Drilling*:  $F_{PreExitRef3a}(h)$

As a conservative value, we used the line connecting the two points, (3mm, 60N) and (1mm, 0N), for decreasing the thrust force reference value. This line is expressed as  $Q_{PE2}Q_{PE3}$  and also down to  $Q_{PE1}$  in Fig. 5.15. However, the dotted line starting from  $Q_{PE2}$  was not specified in the experiments, and the controller was changed to position control when the feedrate became as low as  $\bar{V}_{Exit}$ , whose value is determined below.

(h) Exiting Feed:  $\bar{f}_{Exit}$ , and Feedrate:  $\bar{V}_{Exit}$

The maximum constant exiting feed was determined to be  $\bar{f}_{Exit} = 0.1$  mm/rev (for delamination-free drilling in *PreExit Drilling*, with 9.53 mm drill) from

$$F_{Cutting}(\bar{f}_{Exit}, d) + \frac{h_t}{h_{PE}} F_{Chisel}(\bar{f}_{Exit}, d) < F_D(1) = 25.3[\text{N}] \quad (6.2.5)$$

in Section 5.5. In the experiment of the next section,  $\bar{f}_{Exit} = 0.03$  mm/rev ( $\bar{V}_{Exit} = 1.0$  mm/sec) was chosen. This also implies a safety factor of 3.3 with respect to the feed (feedrate). (Cf. (a) Approaching Feed in *Pre Drilling*:  $\bar{f}_{Approach}$ , and Feedrate:  $\bar{V}_{Approach}$ )

## 6.3 Experimental Results of Supervisory Controlled Drilling of Composite Materials

Figure 6.1 shows a typical experimental result of supervisory controlled drilling of carbon fiber reinforced laminates. (The material was introduced in Section 6.1 and the controller design parameters were determined in Section 6.2.) Delamination did not occur anywhere in the drilled workpiece.

In each set of Fig. 6.1 (a) ~ (c), the first graph's horizontal axis is time, and the second graph's horizontal axis is position; both show the same data. Time and position values are set to be 0 when the thrust force exceeds  $F_{Th} = 4.88$  N, and the origin is also shown by a dash-dot line in each graph. The thrust force reference is determined using the origin. However, the phases in the graphs are determined using the actual position of the drill with respect to the workpiece, and the boundaries between the phases are shown by dotted lines. (The real contact position was determined from the data after the experiment, not during the drilling process.) Figure 6.1 (d) expresses the relation between time and position.

In each graph of (a) and (b), the actual thrust force is expressed by bold lines, and the thrust force reference is expressed by dashed lines. The large difference between the thrust force reference and the actual thrust force was caused by the fact that the workpiece was relatively easy to drill. If a harder workpiece or a blunt drill is used, the same thrust force reference requires much smaller feed, and as a result the actual thrust force can track the thrust force reference easily.

In the *Entrance Drilling* phase, the error of the thrust force (the difference between the thrust force reference and the actual thrust force), in general, is positive, which



suggests that delamination is less likely to occur. In the latter half of the *Middle Drilling 1* phase, the actual thrust force does not decrease as quickly as the thrust force reference decreases. This error suggests an increased risk of delamination.

In Fig. 6.1 (a), the exit thrust force (the thrust force on the boundary between *Middle Drilling 2* and *Exit Drilling*) is about 15 N, and the thrust force at 0.6 ~ 0.7 sec (a few spindle rotations after initiation of constant-feed drilling at 0.03 mm/rev) is about 30 N, which is about 200 % of the exit thrust force. In Table 4.1, there is no data corresponding to a constant feed of 0.03 mm/rev. However, it is reasonable to suppose that the thrust force at 0.03 mm/rev is less than 133 % ( $\approx \frac{29.3}{22.0} \times 100\%$  at 0.1 mm/rev) of the cutting edge thrust force (which almost corresponds to the exit thrust force) at 0.03 mm/rev, because the ratio (thrust force)/(cutting edge thrust force) decreases as the feed decreases. Therefore, it is almost certain that the large thrust force in *Middle Drilling 1* influenced the thrust force in *Middle Drilling 2* mechanically or physically, and that the influence caused the monotonous decrease of actual thrust force at *Middle Drilling 2*. But, it has not been proved yet that the damage under the chisel edge did not reach the bottom surface at 0.6 ~ 0.7 sec, which was the original objective of the experiment.

The actual thrust force of Fig.6.1 (a) shows a small sudden decrease at the point where the chisel edge is at the same height as the bottom surface (*i.e.* on the boundary between *Middle Drilling 2* and *Exit Drilling*), but no noticeable change in slope can be found there (*cf.* Fig. 4.1 (c)). This is caused by the low feedrate 1.0 mm/sec, which was chosen for delamination-free drilling at exit with a large safety factor.

Figure 6.1 (c) shows the torque curve. The torque is not controlled at any point. In the graph, the torque increases in the *Middle Drilling* phase, although the thrust force is

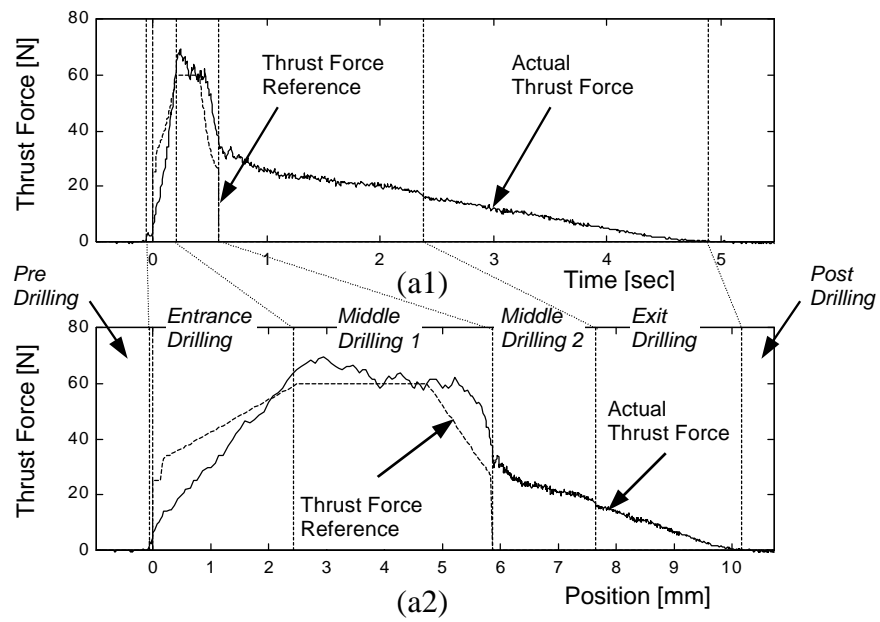
controlled to be constant (*cf.* Figure 4.1 for thrust force and torque during constant feedrate drilling). Therefore, if the workpiece thickness is much larger than 7.72 mm, and the same supervisory control strategy is used, the thrust force reference must be decreased as discussed in Subsection 5.5.2. (Torque control here is another option. However, the supervisory controller must use three controllers and the switching of the controllers requires further study.)

In Fig. 6.1, *Entrance Drilling*, *Middle Drilling 1*, *Middle Drilling 2* and *Exit Drilling* take a total of 4.95 sec, while the drill advances 10.22 mm (= 7.72 mm + 2.5 mm) downward. If 2.0 mm of *Pre Drilling* (at the feedrate of  $\bar{V}_{Approach}=2.0$  mm/sec) and 2.0 mm of *Post Drilling* (at the feedrate of  $\bar{V}_{Exit}=1.0$  mm/sec) are added to this, the total downward action (from *Pre Drilling* to *Post Drilling*) takes 7.95 sec ( $=\frac{2.0}{2.0}$  sec + 4.95 sec +  $\frac{2.0}{1.0}$  sec). The downward action does not include the drill's acceleration at the beginning of *Pre Drilling*, or the drill's deceleration and upward return for the next drilling, at the end of *Post Drilling*. In this discussion, 2 mm of *Pre Drilling* and 2 mm of *Post Drilling* are chosen as the typical lengths where the drill must advance at slow velocities because of uncertainty of the position and thickness of the workpiece.

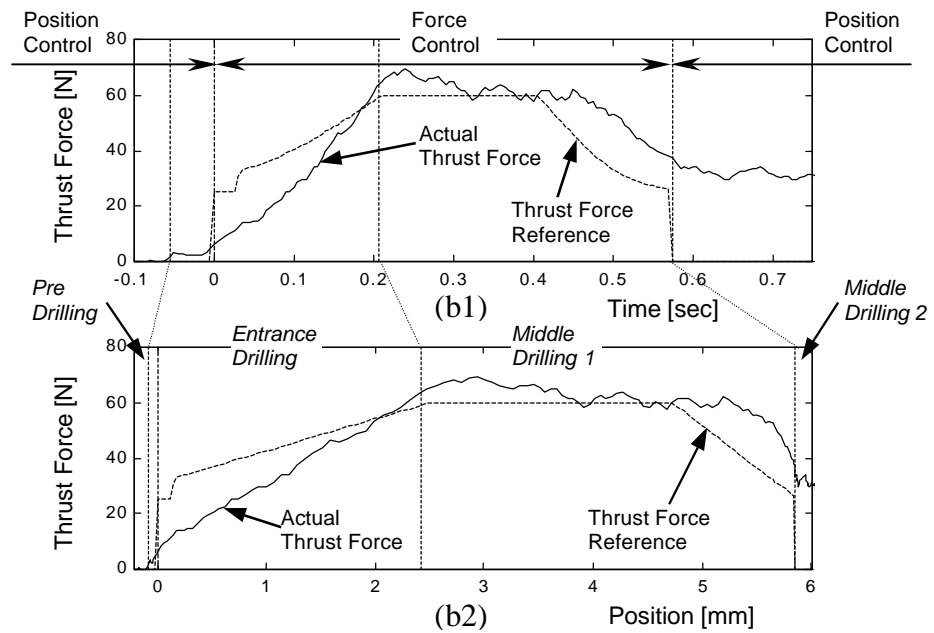
One of the simplest strategies that doesn't use supervisory control is changing the feedrate from  $\bar{V}_{Approach}=2.0$  mm/sec to  $\bar{V}_{Exit}=1.0$  mm/sec only once in the middle of the 10.22 mm (= 7.72 mm + 2.5 mm) advance. This strategy is called Strategy A hereafter. It takes approximately 10.7 sec ( $=\frac{2.0}{2.0}$  sec +  $\frac{10.22/2}{2.0}$  sec +  $\frac{10.22/2}{1.0}$  sec +  $\frac{2.0}{1.0}$  sec), which is about 2.7 sec longer than 7.95 sec of supervisory control. If the workpiece thickness is

19.0 mm instead of 7.72 mm, the estimated difference is about 10 sec (9.1 sec for the supervisory control and 19.1 sec for Strategy A). If the thickness is 34.3 mm, the difference becomes approximately 20 sec (10.6 sec for the supervisory control and 30.6 sec for Strategy A). (In these calculations, the feedrate of the supervisory control corresponding to the part of the extended thickness was assumed to be 10 mm/sec. This feedrate was obtained from the slope in *Middle Drilling 1* of Fig. 6.1 (d).) The time differences estimated above prove the efficiency of the supervisory controller developed in our research.

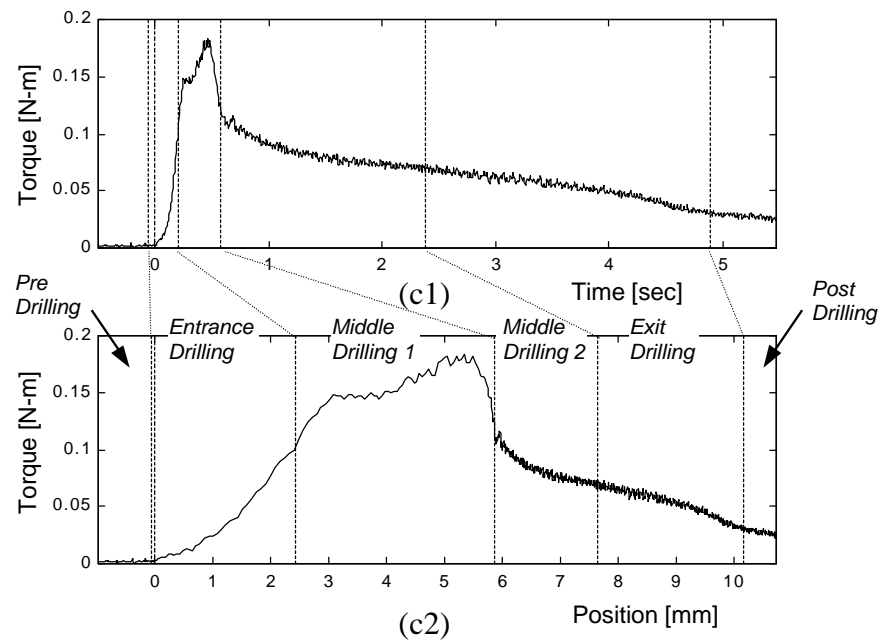
As mentioned at the beginning of this section, no delamination occurred in the workpiece during the experiment. To achieve this, the approaching feedrate and the exiting feedrate were chosen to be  $\bar{V}_{Approach}=2.0$  mm/sec and  $\bar{V}_{Exit}=1.0$  mm/sec, respectively. When these values were determined using Table 4.1, uncertain parts were included in the safety factors introduced in Section 6.2, and only the fact that no delamination occurred exists for each drilling experiment. (If the result of many drilling experiments is analyzed, the best choices of the feedrates can be obtained considering the total cost from the industrial point of view. However, that research topic is not included in our research.) What is also important about our supervisory controller is that it can make the feedrate fast only in *Entrance Drilling* and *Middle Drilling 1* according to the condition of the drill, to make each drilling process efficient without any risk of delamination or drill breakage. This strong point is effective especially when the workpiece thickness is large (as calculated in this section) or when one drill is used continuously to make many holes.



(a) Thrust Force Reference and Actual Thrust Force



(b) Thrust Force Reference and Actual Thrust Force (Partial Enlargement)



(c) Torque

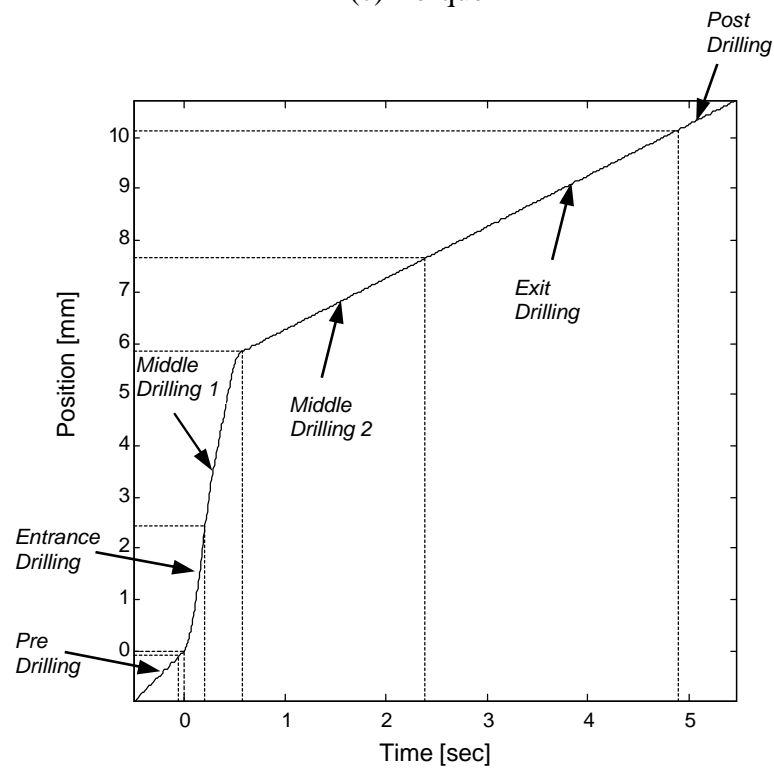


Fig. 6.1 Experimental Data of Supervisory Control of Drilling of Composite Materials.

## **6.4 Summary**

In this chapter, the experiments for the supervisory control of drilling of composite materials were described. First, the process for making specimens of carbon fiber reinforced laminates was shown. All workpieces in the experiments of our research were produced using this procedure. Next, the design of the supervisory controller utilized in our research was explained. The design also expresses how the data and analysis of previous chapters can be applied to determine the parameters. Finally, the experimental results of the supervisory controlled drilling were shown. Both non-delamination and efficiency were satisfied.

## **CHAPTER 7**

### **Conclusions and Future Research**

#### **7.1 Conclusions**

This dissertation has focused on the drilling of composite materials. The study made use of a Matsuura MC510VSS vertical machining center as a drilling machine, and carbon fiber reinforced laminates as workpieces. The work presented in this dissertation can be summarized as follows.

- The drilling process was analyzed and the following phases were proposed: *Pre Drilling*, *Entrance Drilling*, *Middle Drilling*, *PreExit Drilling*, *Exit Drilling*, and *Post Drilling*. All phases were determined by the drill position relative to the top surface and the bottom surface, except for *PreExit Drilling*, which was linked to the damage that occurs below the chisel edge (reaching the bottom surface) during the *Middle Drilling* phase.
- Experiments were conducted to characterize the thrust force and torque for drilling of carbon fiber reinforced composite laminates. The thrust force and torque profiles with respect to the drill position were obtained. The thrust force with a pilot hole was regarded as the thrust force at the cutting edge, and was used to estimate the thrust force at the chisel edge. The parameters in Shaw's equations were obtained by using the average values of thrust force and torque during the full engagement of the drill.

- The Hocheng-Dharan equations, which give conservative values of thrust force for delamination in the *Entrance Drilling* phase and in the *PreExit Drilling* phase, were modified to express the thickness of one lamina explicitly, and the new equations (the discrete Hocheng-Dharan equations) were obtained. Thrust force at the *PreExit drilling* phase was analyzed using the new discrete equations, and it was shown that the last lamina was the most vulnerable for delamination.
- Thrust force and torque dynamics were modeled. It was assumed that both thrust force and torque were proportional to FPHR (Feed Per Half Revolution), which is an imaginary uncut chip thickness in drilling process. The dynamic models in discrete time from the voltage input of the stage to the thrust force and torque signals were constructed.
- A discrete PI controller for the thrust force and torque model in discrete time was developed for a six-sample per spindle revolution dynamic model. Next, the controller was tuned for different spindle speeds by varying the total proportional gain. It was shown that root loci were effective for both determining the stability limits and tuning the controller.
- A supervisory controller for drilling of composite materials was designed. It chooses not only the best control strategy for each phase, but also the reference value and the controller gain that are suitable at each drill position. In the design, the requirements



and the conditions at each phase were analyzed using the information obtained through the characterizations performed in this research.

- Experiments were conducted to show the effectiveness of supervisory control, as well as to introduce one example of installing a supervisory controller using the data and analysis of this research. The experimental results show that the control objective of high productivity without delamination was achieved.

## **7.2 Future Research**

The following is a brief description of the topics that can be extended from this research. They do not require any new experimental setup beyond what was introduced in this dissertation.

- It is worthwhile to apply the supervisory control approach to drilling of circuit boards, laminated metals, aramid and glass laminates. However, if the thickness of the specimen is smaller than the point length of the drill, a new dynamic model and new delamination model must be developed.
- The supervisory controller developed in this research can be applied to metal drilling. In metal machining, the burr formation is related to thrust force in the *Exit Drilling* phase, where the thrust force control is more difficult than in other phases. The development of a burr-formation model, partially studied by Lee (Lee, 1989), still

remains as an unsolved problem. It must be accompanied with FEM simulation and a substantial amount of experiments.

- The development of a delamination model in the *Exit Drilling* phase will be important to obtain an optimal feedrate in this phase. For the *PreExit Drilling* phase, it will also be helpful to construct a delamination model with the analysis of the damage under the chisel edge. The continuity of these two models when the chisel edge just reaches the bottom surface may give hints for the new models.
- A practical method for tuning of the PI force/torque controller is desired. Gain scheduling with a gain estimator and other adaptive control schemes can be considered. However, when the tuning method is studied, the peculiarities of the drilling process and the possibility of installing the controller on an actual industrial setup must be always considered. The stability and overshoot in the transient phase must be given special attention.
- Neural network control and fuzzy control are other good strategies for the control of thrust force and torque. The ambiguity of the dynamics and the process mechanism gives some advantage to these relatively new control methods.
- Disturbance-observer (DOB) based estimation of thrust force provides a great advantage; it removes a dynamometer from the setup and makes it much easier to install the controller on the machines used on the factory floor. The relatively larger

measurement error peculiar to this observer must be considered also from the viewpoint of tolerance to delamination. The research of a drilling robot will be good in the area of industry.

- In this research, spindle speed was regarded as constant, only because the setup did not provide the on-line spindle speed measurement to the controller. However, it is without doubt that the spindle speed decreases when a larger torque is suddenly applied to the drill. If the spindle speed is directly measured, or the spindle motor current is utilized to measure it indirectly, the actual feed instead of the feedrate can be used for the thrust force and torque control.

## Bibliography

Al-Majed, M. I., 1997, "High Performance Machine Tool Controllers – A Control Theoretic Study and a PC-Based Realization", Ph.D. Dissertation, Department of Mechanical Engineering, University of California, Berkeley.

Anderson, B. D. O. and Moore, J. B., 1990, *Optimal Control*, Prentice-Hall, Inc., pp. 323-335.

Chandrasekharan, V., Kapoor, S. G. and Devor, R. E., 1993, "A Mechanistic Approach to Predicting the Cutting Forces in Drilling: with Application to Fiber-Reinforced Composite Materials," in *Machining of Advanced Composites*, ed. by M. Ramulu and R. Komanduri, MD-Vol.45/PED-Vol.66, ASME, pp. 33-51.

Danai, K. and Ulsoy, A. G., 1988, "Dynamic Modeling of Cutting Forces in Turning, Milling, and Drilling, from Experimental Data," in *Control Methods for Manufacturing Processes*, ed. by D. E. Hardt, DSC-Vol.9, ASME, pp. 27-34.

Dharan, C. K. H., Tomizuka, M., Won, M-S, Ozaki, M. and Sheng, Y., 1998, "Integration of Machine Control Schemes in the Machining of Composite Materials," *3rd Intl. Conf. on Integrated Design & Process Tech., ASME Engg. Syst. Design & Analysis Conference*, Berlin, Germany, July 6-9, pp. 294-301.

Dipaolo, G., Kapoor, S. G. and DeVor, R. E., 1993, "An Experimental Investigation of the Crack Growth Phenomenon for Drilling of Fiber-Reinforced Composite Materials," in *Machining Composites*, ed. by M. Ramulu and R. Komanduri, MD-Vol.45/PED-Vol.66, ASME, pp. 15-31.

Doran, J. H. and Maikish, C. R., 1972, "Machining Boron Composites," in *Composite Materials in Engineering Design*, ed. by B. R. Norton, American Society for Metals, pp. 242-250.

Dowling, N. E., 1993, *Mechanical Behavior of Materials*, Prentice-Hall, Inc., pp. 85.

Friend, C. A., Clyne, R. U. and Valentine, G. G., 1972, "Machining Graphite Composite Materials," in *Composite Materials in Engineering Design*, ed. by B. R. Norton, American Society for Metals, pp. 217-224.

Furness, R. J., 1992, "Supervisory Control of the Drilling Process," Ph.D. Dissertation, Department of Mechanical Engineering and Applied Mechanics, The University of Michigan.

Furness, R. J., 1996, "Intelligent Sensor-based Manufacturing: Applications, Needs, and Future Directions," *Japan-USA Symposium on Flexible Automation*, Vol. 2, pp. 1055-61.

Furness, R. J. and Ulsoy, A. G., 1990, "Identification of the Normal Response to Feed Input in a Turning Operation," *Proceedings of the American Control Conference*, pp. 1113-14.

Furness, R. J., Wu, C. L. and Ulsoy, A. G., 1992, "Dynamic Modeling of the Thrust Force and Torque for Drilling," *Proceedings of the American Control Conference*, pp. 384-390.

Furness, R. J., Ulsoy, A. G. and Wu, C. L., 1993, "Feed, Speed, and Torque Controllers for Drilling," *Proceedings of the American Control Conference*, pp. 384-390.

Furness, R. J. and Tsao, T. C., 1995, "Modeling and Torque Control of a Form Tool Drilling Process," *Proceedings of the American Control Conference*, pp. 718-722.

Furness, R. J., Ulsoy, A. G. and Wu, C. L. 1996, "Supervisory Control of Drilling," *ASME Journal of Dynamic Systems, Measurement and Control*, Vol. 118, pp. 10-19.

Guo, L., 1996, "Improved Parameterization for System Identification and Digital Control: Theory and Application to Motion Control Systems," Ph.D. Dissertation, Department of Mechanical Engineering, University of California, Berkeley.

Hatch, J. E., 1984, *Aluminum: Properties and Physical Metallurgy*, American Society for Metals.

Hocheng, H., 1988, "An Analysis of Drilling of Composite," Ph.D. Dissertation, Department of Mechanical Engineering, University of California, Berkeley.

Hocheng, H. and Dharan, C. K. H., 1988, "Delamination During Drilling in Composite Laminates," in *Machining Composite*, ed. by M. Taya and M. Ramulu, MD-Vol.12/PED-Vol.35, ASME, pp. 39-47.

Jain, S. and Yang, D. C. H., 1992, "Delamination-Free Drilling of Composite Laminates," in *Processing, Fabrication, and Manufacturing of Composite Materials*, ed. by T. S. Srivatsan and E. J. Lavernia, MD-Vol.35, ASME, pp. 45-59.

Kakino, Y., Matsubara, A., Nakagawa, H., Takeshita, T., Sato, T., Fujishima, M. and Nishiura, I., 1998, "High Speed and High Productive Drilling by Intelligent Machine Tools," *Japan-USA Symposium on Flexible Automation*, Vol. 1, pp. 285-289.

Kim, J., Dornfeld, D. A. and Furness, R. J., 1999, "Experimental Study of Burr Formation in Drilling of Intersecting Holes with Gun and Twist Drills," *Proceedings of the 27<sup>th</sup> NAMRC*, Berkeley, California, May 25-28, pp. 39-44.

Koenig, W., Wulf, C., Grass, P. and Willersheid, H., 1985, "Machining of Fibre Reinforced Plastics," *Annals of the CIRP*, Vol. 34, No. 2, pp. 537-548.

Koren, Y., 1983, *Computer Control of Manufacturing Systems*, McGraw-Hill.

Koren, Y. and Masory, O., 1981, "Adaptive Control System with Process Estimation," *Annals of the CIRP*, Vol. 30, No.1, pp. 373-376.

Lauderbaugh, L. K. and Ulsoy, A. G., 1989, "Model Reference Adaptive Force Control in Milling," *ASME Journal of Engineering for Industry*, Vol. 111, No.1, pp. 13-21.

Lee, G-B., 1989, "Digital Control for Burr Minimization in Drilling", Ph.D. Dissertation, Department of Mechanical Engineering, University of California, Berkeley.

Ljung, L., 1987, *System Identification: Theory for the User*, Prentice-Hall.

Oh, J-H., 1985, "Model Reference Adaptive Control of the Milling Process," Ph.D. Dissertation, Department of Mechanical Engineering, University of California, Berkeley.

Oxford, C. J., 1955, "On the Drilling of Metals, 1 — Basic Mechanics of the Process," *Trans. ASME*, Vol. 77, pp. 103-114.

Ozaki, M., Tomizuka, M., Dharan, C. K. H., Won, M-S. and Sheng, Y., 1999, "Intelligent Control for Drilling of Carbon Fiber-Reinforced Laminates," *Proceedings of the 27<sup>th</sup> NAMRC*, Berkeley, California, May 25-28.



Ozaki, M., Sheng, Y., Tomizuka, M., Won, M-S. and Dharan, C. K. H., 2000, "Characterization, Modeling and Control of Drilling of Composite Materials," *Japan-USA Symposium on Flexible Automation*, Ann Arbor, MI, July 23-26.

Puw, H. Y. and Hocheng, H., 1993, "Milling Force Prediction for Fiber Reinforced Thermoplastics," in *Machining of Advanced Composites*, ed. by M. Ramulu and R Komanduri, MD-Vol.45/PED-Vol.66, ASME, pp. 73-88.

Saghizadeh, H., 1987, "Delamination Fracture Toughness and Acoustic Emission in Fiber-Reinforced Epoxy Laminates," Ph.D. Dissertation, Department of Mechanical Engineering, University of California, Berkeley.

Shaw, M. C. and Oxford, C. J., 1957, "On the Drilling of Metals, 2 — The Torque and Thrust in Drilling," *Trans. of ASME*, Vol. 79, pp. 139-148.

Sheng, Y., Tomizuka, M. and Ozaki, M., 2000, "Dynamic Modeling and Supervisory Adaptive Predictive Control (SAPC) of Drilling of Composite Materials," *2000 American Control Conference*, Chicago, IL.

Stone, R. and Krishnamurthy, K., 1996, "A Neural Network Thrust Force Controller to Minimize Delamination During Drilling of Graphite-Epoxy Laminates," *International Journal of Machine Tools and Manufacturing*, Vol. 36, No. 9, pp. 985-1003.

Swanson, S. R., 1997, *Introduction to Design and Analysis with Advanced Composite Materials*, Prentice Hall.

Tarn, J. H. and Tomizuka, M., 1989, "On-Line Monitoring of Tool and Cutting Conditions in Milling," *ASME Journal of Engineering for Industry*, Vol. 111, No.3, August, pp. 206-212.

Timoshenko, S. and Woinowsky-Krieger, S., 1959, *Theory of Plates and Shells*, Second Edition, McGraw-Hill, pp. 290-293.

Tomizuka, M., Oh, J. H. and Dornfeld, D. A., 1983, "Model Reference Adaptive Control of the Milling Process," in *Control of Manufacturing Processes and Robotic Systems*, ed. by D. E. Hardt, ASME, pp. 55-63.

Tomizuka, M. and Zhang, S-J., 1985, "Modeling and Conventional/Adaptive PI control of a Lathe Cutting Process," *Proceedings of the American Control Conference*, Boston, MA.

Tomizuka, M. and Zhang, S-J., Oh, J-H. and Chen, M-S, 1985, "Modeling of Metal Cutting Processes for Digital Control," *Proceedings of the 13<sup>th</sup> NAMRC*, Berkeley, CA, May, pp. 575-580.

Tomizuka, M., Dharan, C. K. H., Ozaki, M., Won, M-S. and Sheng, Y., 1999, "Intelligent Machining of Composite Materials," *1999 NSF Design & Manufacturing Grantees Conference*, Long Beach, CA.

Tomizuka, M., Dharan, C. K. H., Ozaki, M., Won, M-S. and Sheng, Y., 2000, "Supervisory Control of Drilling of Composite Materials Intelligent," *2000 NSF Design & Manufacturing Research Conference*, Vancouver, Canada.

Tomizuka, M. and Lee, H-S., 1996, "Robust High-Speed/High-Accuracy Motion Controller," *Manufacturing Systems*, Vol. 25, No.1, pp. 97-104.

Tsao, T-C. and Tomizuka, M., 1994, "Robust Adaptive and Repetitive Digital Tracking Control and its Application to a Hydraulic Servo for Noncircular Machining," *ASME Journal of Dynamic Systems, Measurement and Control*, Vol. 116, pp. 24-32.

Tung, E. D., 1993, "Identification and Control of High-Speed Machine Tools", Ph.D. Dissertation, Department of Mechanical Engineering, University of California, Berkeley.

Ulsoy, A. G. and Koren, Y., 1993, "Control of Machining Processes," *ASME Journal of Dynamic Systems, Measurement, and Control*, Vol. 115, pp. 301-308.

Wong, T. L., Wu, S. M. and Croy, G. M., 1982, "An Analysis of Delamination in Drilling Composite Materials," *Proc. of 14<sup>th</sup> SAMPE Tech Conf.*, pp. 471-483.

Yao, B, Al-Majed, M. and Tomizuka, M., 1997, "High-Performance Robust Motion Control of Machine Tools: An Adaptive Robust Control Approach and Comparative Experiments," *IEEE/ASME Trans. on Mechatronics*, Vol.2, No.2, June, pp. 63-76.